Creep Deformation of 316H Weldments

By

SATYAJIT DEY

Department of Mechanical Engineering
UNIVERSITY OF BRISTOL

A dissertation submitted to the University of Bristol in accordance with the requirements of the degree of DOCTOR OF PHILOSOPHY in the Faculty of Engineering.

JULY 2020

Word count: forty five thousand eight hundred and twenty

Abstract

Many power plant components, such as steam generators, are exposed to creep regime temperatures during operation. Creep deformation is a major life limiting factor for such components. Therefore, estimation of creep life is important for ensuring safe operation of power plants. Austenitic steel is commonly used for steam generator components which also include thick sections of multi-pass welds. Creep deformation and damage is a bigger problem in multi-pass welds due to the material heterogeneity of such welds along with presence of defects and weld residual stresses. Investigation of creep damage is particularly complex in such welds. A robust understanding of creep deformation is the first step to any creep damage assessment. A realistic model of creep deformation of multi-pass weldments is complicated by the presence of different material zones, namely, base metal, weld and the heat affected zone (HAZ). This thesis investigates the existence and extent of elastic-plastic and creep properties variation across a 316H steel multi-pass weld and also explores effects of such mismatch on the overall creep response of the weldment. The scope of the work is limited to the creep deformation behaviour of 316H multi-pass welds and therefore tertiary creep was not explored in this treatise.

Estimates for stress and strain concentration effects were obtained using simplified finite element (FE) models and the results were compared against weld stress concentration factors from earlier work and engineering assessment codes. Localised creep tests were conducted on small test specimens extracted from different locations of an ex-service 316H weld HAZ section and thereby minimum creep rate in the HAZ was characterised as a function of the distance from the weld fusion line. DIC creep tests were then conducted on crossweld specimens of the aforementioned weld at different stress levels and using benchmarked finite element models, the full field strain and stress distributions in the specimens were studied. Also, DIC creep testing and finite element modelling were used to investigate any augmented effects of weld cap

geometry on stress concentrations due to existing material mismatch across the weld fusion line of a 316H multi-pass weld.

Results from the analytical models showed that upper bound estimates of stress concentration factors for the worst level of creep rate mismatch across a weld interface will always be lower than the stress concentration factors used for dissimilar welds. A method of creep rupture design of weldments was proposed which considers both the rupture stress in the creep strong material as well as creep strain rates in the creep weak material near the weld interface. DIC creep tests of crossweld samples of 316H weld depicted the extent and deformation behaviour of a creep strong material zone in the HAZ section. Finite element model results showed good correspondence with the tests and it was demonstrated that a combination of FE modelling and DIC tests can reveal true stress as well as strain field information in a test specimen. DIC creep tests and analytical modelling of a crossweld specimen with a simulated weld cap showed that effect of creep mismatch remains insignificant and the stress concentration due to only the weld cap geometry remains unchanged from that of a homogeneous metal specimen.

The work showed that although there can be significant difference in creep deformation behaviour between the base metal and the weld metal in a 316H multi-pass weld, its effects on stress and strain rate distributions near the weld fusion line and in the overall weld are insignificant. Also, the work demonstrated the use of a combination of DIC creep tests and FE modelling in studying weld creep and determination of the extent of a creep strong region in the weld where creep rates gradually vary. Stress concentration factors due to weld caps will be dominated by the geometry effects with insignificant contribution from the creep rate mismatch between the weld and the HAZ.

Dedication and acknowledgements

In loving memory of my father late Subodh Kumar Dey. There is an endless list of people who have directly or indirectly supported me during my PhD and only a selected number of them are mentioned here.

At first I want to thank late David Smith who had trusted me and offered me the research position. Next, I would like to thank my supervisors Professor David Knowles and Professor Christopher Truman for guiding me through my PhD and motivating me throughout. Both were extremely supportive and flexible in terms of direction of work. Dave and Chris would always ask the relevant questions at every stage to make sure that the work was on track and took care of any resources I needed to conduct my research.

I acknowledge the financial support from EDF Energy, Atkins SNC Lavalin and the University of Bristol in terms of stipends and scholarships. I would like to thank Dr. David Dean and Dr. Marc Chevaliar for their valuable inputs during our quarterly interactions. I thank Mr. Mike Spindler for sharing material data which was of extreme importance in my project.

I acknowledge the support of Open University and the University of Nottingham for allowing me to conduct some of the most important experiments there using their facilities. My special gratitude to Professor John Bouchard, Dr Alex Forsey, Mr Stan Hiller, Ho Kyeom Kim, Johannes and Ellies for supporting me with various activities related to my experiments at the Open University. I thank Professor Wei Sun and Mr Shane Maskill of University of Nottingham for allowing to do my experiments there.

I would like to thank the current and past research students and research associates of my department, Ed, Andrew, Nader, Sam, Paulo, Tomi, Aditya, Abdullah, Mehdi, Chris and Kostas for their help and friendship.

Finally, I cannot thank enough my family; without the sacrifices of my mother, I wouldn't be

able to accomplish this work. I acknowledge the contribution of my sister, brother in law, my in laws and all the members of Dey family for never failing to motivate me. Last but not the least, I would like to thank my wife, Sarmistha, for her sacrifices and relentless support during my PhD and unconditional love for me.

AUTHOR'S DECLARATION

I declare that the work in this dissertation was carried out in accordance with the requirements of the University's Regulations and Code of Practice for Research Degree Programmes and that it has not been submitted for any other academic award. Except where indicated by specific reference in the text, the work is the candidate's own work. Work done in collaboration with, or with the assistance of, others, is indicated as such. Any views expressed in the dissertation are those of the author.

SIGNED: .. [redacted] .. DATE: 31/072020

TABLE OF CONTENTS

Page

List of Tables **xi**

List of Figures **xiii**

1 Introduction **1**

1.1 Thesis Outline 2

2 Literature Survey **5**

2.1 Stainless Steels 5

2.1.1 Austenitic Stainless Steels 6

2.2 Creep deformation in austenitic stainless steels 8

2.2.1 Representation of Creep Data 9

2.2.2 Creep Mechanisms 10

2.2.3 Dependence of Creep on Stress and Temperature 13

2.2.4 Creep Models for 316H Steel 14

2.2.5 Effects of multi-material creep rates on stress and strain distributions in a weldment 15

2.3 Creep Testing 18

2.3.1 Impression Creep Test 18

2.3.2 Digital Image Correlation based Strain Measurement 21

2.4 Numerical modelling of Plasticity and Creep Using ABAQUS 34

3 Finite Element Modelling of Stress and Strain Distributions due to Mismatch in Creep Rates in a Thick Weld **37**

3.1 Specification Finite Element Weld Models 39

3.2 Review of Stress Singularity at a Bi-material Creep Interface 41
3.2.1 Stress Singularity in a Bi-material Elastic-Creep Finite Element Model . . 42
3.2.2 Stress Singularity in a Bi-material Elastic-Plastic-Creep Finite Element Model 45
3.2.3 Use of Singular Elements Instead of a Fine Mesh at the Singularity 47
3.3 Stress Concentrations due to Creep Mismatch 48
3.3.1 Interpretation of Results 49
3.3.2 Results and Discussion 53
3.3.3 Conclusions 64

4 Investigation of variation of creep rates in a 316H multi-pass weld 67
4.1 Impression Creep Tests 69
4.1.1 Test Material 69
4.1.2 Specimen Design 73
4.1.3 Test Data Analysis 73
4.1.4 Test Set Up 77
4.2 Impression Creep Test Results 80
4.3 Analytical Benchmarking of Test Results 86
4.4 Conclusions 90

5 Measurement of creep mismatch and analysis of its effects in a 316H cross-weld specimen 93
5.1 DIC Creep Tests 94
5.1.1 Test Material and Specimen Design 95
5.1.2 Test Apparatus 96
5.1.3 Specimen Speckle Pattern 97
5.1.4 Test Procedure 100
5.1.5 Data Analysis 100
5.2 Test Results 102
5.2.1 Test 2B (σ_{engg} = 250MPa) 104
5.2.2 Test 2C (σ_{engg} = 300MPa) 106
5.2.3 Test 2A (σ_{engg} = 330MPa) 109

5.3 Finite Element Modelling 112
5.3.1 FE Model Results 118
5.4 Conclusions 121

6 Effect of a simulated weld cap on creep of an ex-service 316H weld 125
6.1 DIC Creep Test 126
6.2 Test Results 129
6.3 FE Modelling 133
6.4 FE Model Results 135
6.5 Conclusions 136

7 Conclusions 139

Bibliography 143

List of Tables

Table **Page**

2.1 RCCM-R model constants for 316H steels 15
2.2 95% confidence limits on creep constants for 316H RCCM-R model 15

3.1 Elastic constants used for the weld models 40
3.2 Table of material and geometry constants for the FE models 50

4.1 Service Conditions of Cast 69431 HYA 2C2/3 Header material 70
4.2 Composition of Cast 69431 316H steel 70
4.3 Welding details of the Heysham 2C2/3 weld 70
4.4 Composition of Cast 69431 316H steel 71
4.5 Test parameters for the impression creep test 79
4.6 Stress-strain data used in the FE models for the weld and the parent material sections 89
4.7 RCCM-R model constants for 316H steels 89

5.1 DIC creep test matrix 95
5.2 Thermocouple calibration for DIC creep tests 100
5.3 DIC analysis parameters 101
5.4 Stress-strain data used in the FE models for the weld and the parent material sections116
5.5 Creep constants from data fits for the parent and the weld 117

6.1 Creep constants from data fits for the HAZ/parent and the weld 135

List of Figures

Figure **Page**

2.1 Schaeffler-Delong diagram identifying the phase boundaries of 316L steel alloys 316L SS alloys with different Cr equivalent and Ni equivalent values (Hedstrom [13]) . . . 8

2.2 A typical creep curve of a metal showing the three different stages of creep: primary, secondary and tertiary . . . 9

2.3 A map of creep deformation mechanisms of 316H steel with $50\mu m$ grain size (Frost and Ashby [24]) . . . 11

2.4 Schematic showing A) Nabarro-Herring and B) Coble Creep (Babu [28]) . . . 12

2.5 Schematic showing dislocation creep mechanisms . . . 12

2.6 Schematic showing the principle of impression creep and important geometrical parameters of a typical impression creep test . . . 19

2.7 Typical impression depth versus time curve for an impression creep test . . . 19

2.8 Principle of Digital Image Correlation (Zhang and He [112]) . . . 23

2.9 Schematic showing derivation of deformed coordinates of a Point in a reference subset using first order element shape function . . . 26

2.10 Sample of un-interpolated intensity data for an 8x8 subset (Bruck et al [117]) . . . 28

2.11 Schematic showing the location of pixels and the area over which interpolation is done 28

2.12 Sample of interpolated intensity data for an 8x8 subset (Bruck et al [117]) . . . 29

2.13 Example 3x3 Gaussian fit to image profile . . . 31

2.14 Example of reference images with three different decreasing speckle sizes: (1) > (2) > (3) (Pan et al [131]) . . . 33

2.15 Standard Deviation of Error for the three reference speckle patterns in figure 2.14 (Pan et al [131]) . . . 33

2.16 Example of effect of camera zoom for the same speckle pattern (Lecompte et al [129]) 34

2.17 Schematic showing the growth of yield surface for isotropic hardening plasticity . . . 35

3.1 Weld model geometry, 't' is the weld thickness and 'w' is the plate width 41
3.2 Schematic showing the location of stress singularity in a bi-material creep model . . . 42
3.3 Variation of equivalent stress ratio with normalised distance from the singularity along the weld interface 44
3.4 N_{eq} versus $1/n$ plots for a creep strong weld for a range of values of $\frac{A_w}{A_p}$ 45
3.5 N_{eq} versus $1/n$ plots for a creep soft weld for a range of values of $\frac{A_w}{A_p}$ 46
3.6 Contour plot of plastic strain near the singularity point 47
3.7 Variation of normalised equivalent stress with normalised distance from the singularity along the weld interface 48
3.8 Evolution of equivalent plastic strains along the interface in the weld metal 49
3.9 Plot of differential equivalent plastic strains in the weld metal to that of equivalent creep strains in the parent material for different creep times 49
3.10 Schematic showing the structure and location of the singular elements 50
3.11 Comparison of mesh with normal quadratic elements and mesh with singular quadratic elements in the vicinity of the singularity 51
3.12 Plot of normalised equivalent stresses versus normalised distance along the weld interface for conventional and singular elements 52
3.13 Schematic showing non-uniform and symmetrical axial stress distribution at the weld interface in the model 52
3.14 A schematic of the decomposed weld interface of the model explaining the origin of bending as a result of lateral strain mismatch 53
3.15 Plot of von Mises stresses along with linearised stresses along normalised distance from the singular point along the weld interface 54
3.16 Plot of von Mises stresses along with linearised stresses along normalised distance from the singular point along the weld interface 54
3.17 Plot of linearised and von Mises stresses along normalised distance from the singular point in order to show where on the von Mises stress plot the maximum magnitude of linearised stress occur 55
3.18 Contour plot of von Mises equivalent stresses in the weldment for $\frac{A_w}{A_p} = 0.1$ 55
3.19 Contour plot of equivalent creep strains in the weldment for $\frac{A_w}{A_p} = 0.1$ 56

3.20 Contour plot of SCFs for von Mises and maximum principal stresses in the weldment for $\frac{A_w}{A_p} = 0.1$ 58
3.21 Contour plot of Spindler fraction in the weldment for $\frac{A_w}{A_p} = 0.1$. A value close to 1 denotes a perfectly uniaxial stress state. 58
3.22 Plot of SCFs for von Mises and maximum principal stresses against nominal equivalent creep strains in the parent for $\frac{A_w}{A_p} = 10$ 59
3.23 Plot of equivalent SREFs in the creep soft parent against nominal equivalent creep strains in the parent for $\frac{A_w}{A_p} = 10$ 60
3.24 Variation of SCF in the creep hard weld and equivalent SREF in the creep soft parent against applied stress 61
3.25 Variation of SCF in teh creep hard weld and equivalent SREF in the creep soft parent against applied stress 61
3.26 Flowchart showing the steps to calculate creep rupture life of a weldment 64

4.1 Supplied material blanks of ex-service 316H steel weldment 71
4.2 Test weld geometry 72
4.3 Stress strain curves of Cast 69431 REP weld 72
4.4 Creep strain curves for Cast 69431 parent material for different stresses 74
4.5 Creep strain curves for Cast 69431 HAZ material for different stresses. Creep strain versus time for stresses in the range $[260MPa, 300MPa]$ at a temperature of $550°C$. 75
4.6 Schematic showing the test raw material and the different locations along the weldment from where the test specimens were extracted 75
4.7 Schematic showing the actual distances of the machined test specimens from the weld fusion line 76
4.8 A photograph of a typical impression test specimen showing the important dimensions 76
4.9 A schematic of a rectangular impression creep test specimen where length of the specimen is $'b'$, the width is $'w'$ and the thickness is $'h'$; the indenter width is $'d'$ . . . 77
4.10 Plot of the impression creep conversion factors against the ratio of the indenter width to specimen thickness for a rectangular indenter 78
4.11 A schematic of the test set up showing the locations and arrangement of the LVDTs . 79
4.12 A photograph of the impression creep test set up at Nottingham University 79

4.13 Raw impression creep results of the Parent specimen showing impression depth versus time for the two LVDTs and their average 81
4.14 Raw impression creep results of the HAZ1 specimen showing impression depth versus time for the two LVDTs and their average 81
4.15 Raw impression creep results of the HAZ3 specimen showing impression depth versus time for the two LVDTs and their average 82
4.16 Raw impression creep results of the HAZ5 specimen showing impression depth versus time for the two LVDTs and their average 82
4.17 Raw impression creep results of the Weld specimen showing impression depth versus time for the two LVDTs and their average 83
4.18 Impression velocity (rate of indentation) versus time for all the specimens and power law fits to all the specimens except the weld specimen 84
4.19 A bar chart of the minimum creep rates in the different impression test specimens along with error bars representing the error in the power law fits used to calculate the minimum creep rates 84
4.20 A schematic showing the effective loading orientation between the conventional and impression creep tests 85
4.21 A comparison of the impression creep test derived minimum creep rates in the parent and the weld specimens with the RCCM-R model and parent conventional creep test data 86
4.22 A comparison of the impression creep test derived minimum creep rates in the HAZ1, HAZ3 and HAZ5 specimens with the RCCM-R model and HAZ conventional creep test data 87
4.23 Schematic of the FE models showing the geometry and loading conditions 87
4.24 FE model mesh. Reduced integration linear elements were used for the analysis . . . 88
4.25 Equivalent creep strain distribution in the FE model after 400h 90
4.26 Plot of total impression depth with time for LVDT2 and FE analysis 90
4.27 Plot of increase in impression depth with time during creep for LVDT2 and FE analysis 91

5.1 DIC Creep Test Set Up 95
5.2 Specimen drawing for tests 2A and 2C 96
5.3 Specimen drawing for test 2B 96

5.4 Image Histogram of Test 2A Speckled Specimen 97
5.5 Image Histogram of Test 28 Speckled Specimen 97
5.6 Image Histogram of Test 2C Speckled Specimen 98
5.7 Image Histogram of Test 2A Speckled Specimen 98
5.8 Image Histogram of Test 2B Speckled Specimen 99
5.9 Image Histogram of Test 2C Speckled Specimen 99
5.10 Schematic showing a bayer pattern 101
5.11 Temperature history of Test 2A 102
5.12 Temperature history of Test 2B 103
5.13 Temperature history of Test 2C 103
5.14 Contour plot of longitudinal strains (ϵ_{yy}) as computed between two images of test 2A specimen taken before start of the test and at test temperature. The strain values shown correspond to noise level associated with the DIC data analysis. 104
5.15 Longitudinal strain (ϵ_{yy}) contour plots obtained at different times from test 2B 105
5.16 Longitudinal strain (ϵ_{yy}) plots along the specimen longitudinal centreline at different times for test 2B 106
5.17 Time history plots of longitudinal strains (ϵ_{yy}) at different locations in the test 2B specimen 107
5.18 Area reduction plots along the specimen longitudinal centreline at different times for test 2B 107
5.19 Longitudinal strain (ϵ_{yy}) contour plots obtained at different times from test 2C 108
5.20 Longitudinal strain (ϵ_{yy}) plots along the specimen longitudinal centreline at different times for test 2C 109
5.21 Longitudinal strain (ϵ_{yy}) contour plots obtained at different times from test 2A 110
5.22 Longitudinal strain (ϵ_{yy}) plots along the specimen longitudinal centreline at different times for test 2A 110
5.23 Plot of minimum creep rate versus applied stress for the parent and the weld sections derived from the DIC creep tests 111
5.24 Schematic of the FE models showing the geometry and loading conditions 113
5.25 Schematic of the FE models showing the geometry and loading conditions 114
5.26 Schematic of the FE models showing the geometry and loading conditions 114

5.27 Stress strain curves of Cast 69431 REP weld 116
5.28 Creep model comparison with actual creep data for 316H Parent 116
5.29 Test 2B FE model showing the variation of the state variable l_w and schematic variation of stress-strain and creep properties across the SAZ. The subscript 'i' indicates a point on the material stress-strain curve as presented in table 5.4 117
5.30 Comparison of longitudinal strain (ϵ_{yy}) evolution with time between DIC creep test and FE model of specimen 2A 118
5.31 Comparison of longitudinal strain (ϵ_{yy}) evolution with time between DIC creep test and FE model of specimen 2B 119
5.32 Plot of longitudinal strain (ϵ_{yy}) versus time for different material points for test 2A and the corresponding FE model 120
5.33 Plot of longitudinal strain (ϵ_{yy}) versus time for different material points for test 2B and the corresponding FE model 120
5.34 Contour plot of true von Mises equivalent stress (σ_e) at different times for FE model 2B121

6.1 Capped crossweld specimen for DIC creep test 127
6.2 Capped crossweld specimen image histogram 128
6.3 Capped crossweld specimen speckle pattern 128
6.4 Plot of temperatures recorded by the thermocouples and target temperatures of each versus time 129
6.5 Contour of elastic-plastic initial loading strains 130
6.6 Contour of elastic-plastic strains accumulated during creep at different creep times . 131
6.7 Plot of creep strains versus distance for a horizontal line in the specimen for x_w = 2.63mm for different creep times 131
6.8 Plot of creep strains versus distance for a horizontal line in the specimen for x_w = 5.96mm for different creep times 132
6.9 Plot of creep strains versus distance for a horizontal line in the specimen for x_w = 9.35mm for different creep times 132
6.10 Schematic of the FE model showing the geometry and loading conditions 134
6.11 FE mesh of the DIC creep test specimen with a simulated weld cap 134
6.12 Capped crossweld specimen speckle pattern 136
6.13 Capped crossweld specimen speckle pattern 137

6.14 Capped crossweld specimen speckle pattern 137

CHAPTER 1

INTRODUCTION

> *"When an idea exclusively occupies the mind, it is transformed into an actual physical or mental state."*
>
> Swami Vivekananda

Electricity generation from nuclear power plants constitutes about 19% of the total electricity generation in the UK (BRIEF, UK ENERGY IN [1]). Most of the nuclear power plants in the UK are Advanced Gas cooled Reactors (AGR). In the AGRs, steam generators are irreplaceable and hence the structural integrity of the steam generators govern plant life. They are generally made of austenitic stainless steels. In these power plants, the steam generators operate at creep regime temperatures of austenitic steels. This means that they are susceptible to creep deformation and damage during plant operation. Therefore, for ensuring safe plant operation, plant life assessment procedures are used for estimation of the extent of creep damage in steam generator components. The steam generators also include a number of thick multi-pass welded sections. Estimation of creep damage in weldments is complicated due to their inherent inhomogeneity, presence of residual stresses and presence of welding defects. The creep assessment procedures such as R5 ([2]) use simplistic and conservative approaches for creep assessments. For matching welds (similar metal), the creep deformation properties of the parent is used for assessments with an allowance for taking into account the creep strength mismatch

between the parent and the weld metal. Thus, an accurate prediction of creep deformation in such weldments is not used for determining creep damage. Since the prediction of creep deformation is usually the first step to any sound creep damage model, creep damage estimation procedures in assessment codes and methods can be highly inaccurate. For dissimilar metal welds, a stress concentration factor is used for creep rupture assessments but that can be too over-conservative for matching welds. Also, such stress concentration factors are obtained from comparing creep rupture test results of welded test specimens to that of the base metal and do not directly consider the effects of creep deformation due to mismatch.

The aim of this work is to investigate the effects of creep mismatch on the creep deformation behaviour of an ex-service multi-pass weld of 316H steel. The specific objectives of the work can be summarised as:

1. Use simple finite element (FE) modelling to determine the effects of creep mismatch across an abrupt weld interface on stress and strain distribution in a crossweld specimen

2. Determine the gradation of minimum creep rates in an ex-service 316H weldment and the effects of such mismatch on the stress and strain distributions in such a weldment using modelling and experiments

3. Investigate the augmenting effect of weld geometry, such as a weld cap, on stress and strain distributions in a weldment

1.1 Thesis Outline

The thesis is composed of 7 chapters in total. A summary of the next 6 chapters is provided in the paragraphs below.

Chapter 2 provides a comprehensive summary and critical analysis of available literature on the relevant context. Some of the topics covered in the chapter are: austenitic stainless steels, theory of creep, description of creep behaviour of 316H steels, description of the test material used in the present work, stress concentration in thick welds, creep testing methods used in this work and finite element analysis of creep using ABAQUS software. Critical analyses of relevant work are also presented.

Chapter 3 investigates the effect of creep mismatch on creep strain and stress distributions in a weld by means of a simple finite element model. Two distinct material regions (parent and weld) were considered separated by an abrupt interface. Sensitivity studies are performed with respect to various factors such as applied stress, weld geometry and creep model parameters. Results are compared to earlier studies. Finally, creep design methods used in ASME codes and R5 methods for determining reference rupture stress for a weldment are discussed in the light of the findings.

Chapter 4 investigates the gradation of minimum creep rates in the HAZ of an ex-service multi-pass 316H weldment. Impression creep tests are used to plot a graph of minimum creep rate versus distance from the weld fusion line through the HAZ section of the weld. Impression creep results from far away parent material validated using finite element modelling is used to serve as reference results.

Chapter 5 presents the effects of variation of mechanical and creep properties across a crossweld specimen taken from an ex-service multi-pass 316H weld. Digital Image Correlation (DIC) based creep tests are used to obtain a full field strain information in the specimens during creep at various applied stress levels. Test results are used to estimate the extent of HAZ for this type of welds. Finite element models are benchmarked against the tests and used to obtain full field stress information during creep.

Chapter 6 presents the effect of weld cap on creep deformation in a multi-pass weld. The chapter explains important conclusions from DIC creep tests done on a crossweld specimen with a 'simulated' weld cap and uses FE modelling to validate the results.

Chapter 7 presents important conclusions from the work.

CHAPTER 2

LITERATURE SURVEY

"The reading of all good books is like conversation with the finest (people) of the past centuries."

Descartes

This chapter provides a detailed discussion on the concepts and theories used in this work and reviews previous work done on two material analytical creep models and creep testing. The chapter starts with a description of the composition and behaviour of stainless steel welds followed by a description of the test weldment for the current work. It contains a comprehensive discussion on creep behaviour of austinitic stainless steels, assessment methods used for creep deformation, stress concentration in welds due to material mismatch, impression creep tests, digital image correlation (DIC) based creep tests and numerical schemes used for creep in finite element modelling.

2.1 Stainless Steels

Stainless steels are a type of iron-carbon alloys with chromium and nickel as the main alloying elements and small quantities of other alloying elements like molybdenum, tungsten and manganese (Peckner and Bernstein [3]). They are called stainless steels for their significantly

higher corrosion resistance. The chromium in the steel forms a stable layer of chromium oxide when exposed to air and thus prevents the exposure of the steel. A minimum of 12% chromium is needed to achieve corrosion resistance (Higgins et al [4]). The addition of chromium makes their high temperature oxidation resistance good. However, their higher temperature resistance is mainly due to dispersion hardening caused by the nitrides and carbides of other alloying elements (Higgins et al [4]).

There are five groups of stainless steels: ferritic, austenitic, martensitic, ferritic-austenitic and precipitation-hardening steels (Metal Handbook [5]). In AISI type of nomenclature, stainless steels are defined by using three subsequent numbers, for example, series 100 and 200 denote austenitic chromium nickel manganese alloys, series 300 represents austenitic chromium nickel alloy and series 400 is used for ferritic and martensitic chromium alloys (Totten and George [6]). Series 100 and series 200 have similar compositions; series 100 steels are used for steel furnitures whereas series 200 steels are general purpose steels.

2.1.1 Austenitic Stainless Steels

Austenitic steel is one of the four main types of stainless steels: austenitic, ferritic, martensitic and duplex. They are called austenitic steels as their primary crystalline structure is austenite. Since chromium is used in stainless steels to improve corrosion resistance which is a ferrite stabiliser, in order to retain the austenite crystal structure at room temperature, austenite retaining elements such as nickel, manganese and nitrogen are used in these types of steels (Krauss [7]). The austenite stabilising elements possess a face centred cubic (FCC) crystal structure and therefore inhibit the transformation of austenite to ferrite (Higgins et al [4]).

Two subgroups of austenitic steels, the 200 and the 300 series, exist. The 300 series austenitic steels contain nickel as their main austenite stabilising element and is the bigger group. The two most common 300 series austenitic stainless steels are the 304 and the 316 series steels. 316 series steel is more corrosion resistant than 304 steels. In the initial solution treated state, all 300 series steels are unstable. Therefore, when exposed to prolonged periods of time at a high temperature, carbide precipitation occurs (Marshall [8]).

Austenitic steels have a face centred cubic (FCC) structure and are non-magnetic. They have high formability, strength, ductility and toughness (Vaccari [9]). Austenitic stainless steels possess high oxidation resistance and retain their exceptional strength at high temperatures.

Austenitic steels exhibit good weldability and are extensively used in piping and pressure vessels, cooking utensils and cladding.

2.1.1.1 Type 316H austenitic stainless steel

Type 316H stainless steels are a member of the austenitic group with a typical composition C (0.04%-0.10%) Si (0.75%) Mn (2.0%) P (0.045%) S (0.030%) Cr (16.0%-18.0%) Mo (2.0%-3.0%) Ni (10.0%-14.0%) (Euro Inox 2012 [10]). Chromium in the steel forms protective oxide layer and impedes the diffusion of oxygen further into the steel (Euro Inox 2012 [10]). High temperature strength, ductility and resistance to carburisation is increased by the addition of nickel. Creep strength is improved by a higher carbon and nitrogen content and the presence of molybdenum.

2.1.1.2 Austenitic steel weld metal

The 316H weldment studied in this work used a 316L weld filler metal. During multi-pass welding, the weld passes and the nearby parent material are exposed to complex temperature histories. This results in a variation of microstructure both in the individual weld passes and the nearby parent material (Takahashi et al [11]). During each welded pass, heat is added to the molten weld metal and the surrounding parent metal which then cools off by conducting away the heat. This heating and cooling of the weldment during welding constitutes a thermal cycle. The weld beads which are deposited earlier, see a higher number of thermal cycles than the weld beads deposited later. Therefore, a variation of the degree of work hardening and microstructure exist in multi-pass weldments.

The resultant microstructure of the weld metal after welding depends on the mode of solidification, the organisation of the dislocations and the precipitates (Lippold and Kotecki [12]). Schaeffler-Delong diagram (figure 2.1, Hedstrom [13]) is used to identify the balance of different phases in austenitic steels as a function of it's composition. In this diagram, phases A, F and M denote austenite, ferrite and martensite phases respectively. Chromium and nickel equivalents are calculated and used as the two axes of the diagram. Austenite (γ) is the first phase to form in the A and AF regions whereas ferrite (δ) is the primary phase to form in the FA and the F regions. Austenitic welds are susceptible to hot cracking. Presence of δ-ferrite avoids short term failure of austenitic welds at low strains (Thomas [14]). Therefore, 316L weld metals are made to contain 3 to 8% δ-ferrite.

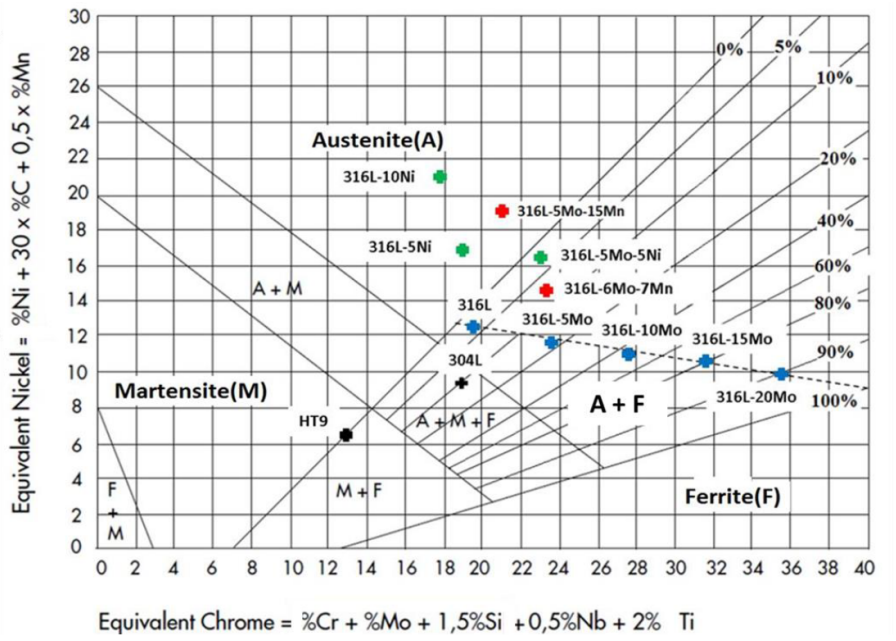

Figure 2.1: Schaeffler-Delong diagram identifying the phase boundaries of 316L steel alloys 316L SS alloys with different Cr equivalent and Ni equivalent values (Hedstrom [13])

2.2 Creep deformation in austenitic stainless steels

Engineering components when exposed to high temperature loading for a prolonged period of time produce time dependent inelastic strains. Under such circumstances, the material is said to undergo creep deformation. A sufficiently longer operation time for a combination of temperature and loading may lead to excessive plastic deformation or creep rupture. The combination of temperature, loading and time leading to a particular level of creep strain is dependent on the material and the environment.

The temperature at which creep occurs varies widely among different materials. However, it has been observed that the melting temperature of a material has a high bearing on its creep temperature. For austenitic stainless steels, the temperature above which substantial creep occurs, is of the order of 0.4Tm, where Tm is the melting temperature of 316H steel (Brnic et al [15]). Above this temperature, time dependent diffusion of atoms occurs along grain boundaries of metals and the mechanism is known as Coble creep (Hill [16], Coble [17]). Creep is an important source of material damage occurring at high temperatures (Lagneborg [18], Murty and Charit [19]).

2.2.1 Representation of Creep Data

Creep data is represented by a creep curve, which is a plot of strain versus time for a material obtained from a constant load creep test at a fixed temperature (Callister [20]). For generating a material creep curve, unixial creep tests can be carried out at constant load or constant stress. In a constant load creep test, the true stress increases with the decrease in cross-sectional area of the test specimen. Generally a constant stress creep curve is more useful (Garofalo [21]). Figure 2.2 shows a typical creep curve obtained from a constant load test conducted at a constant temperature. The constant load creep curve is characterised by three distinct regimes, namely, primary creep, secondary creep and tertiary creep. Primary creep occurs just after the initial strains in the test specimen caused by the load application where the creep rate decelerates. At the end of primary creep, the creep rate becomes constant which is known as the secondary creep. Finally, the creep rates starts accelerating in the tertiary creep regime which terminates in the fracture of the specimen.

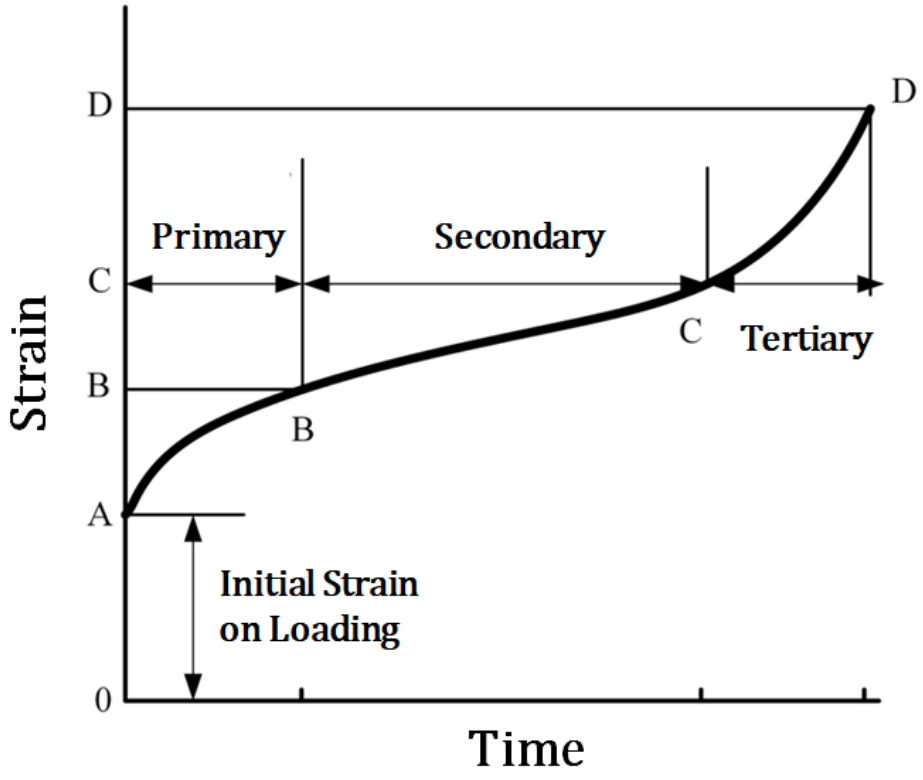

Figure 2.2: A typical creep curve of a metal showing the three different stages of creep: primary, secondary and tertiary

The primary creep deformation stage occurs first and it exhibits a decreasing creep strain rate with time. This is because the work hardening dominates over thermally activated recovery processes. Work hardening in type 316H steels occurs primarily due to the generation and movement of dislocations in the crystal structure of the material resulting from the applied stress. Dislocation movement is eventually inhibited due to the impediments arising out of increased dislocation density resulting in considerable reduction of available mobile dislocations. The secondary stage represents a linear variation of creep strain with time which is a result of a balance between work hardening and thermal recovery (softening). This is the longest portion of the curve (Monkman [22]). The creep strain rate in the secondary stage is the minimum creep strain rate and can be used to represent a combination of material and temperature. The last stage before fracture i.e. the tertiary creep stage exhibits a rapid increase in creep strain rate with time. This occurs due to the formation of cavities within the material which leads to stress concentration sites in the material together with a reduction in load bearing area (Sposito [23]).

2.2.2 Creep Mechanisms

Creep mechanisms vary across materials as well as test parameters (applied stress and temperature). Therefore, based on type of material, creep deformation processes for different loading conditions are represented by creep deformation mechanism map. Frost and Ashby [24] constructed creep deformation maps for different materials at various applied stress levels and temperature. Figure 2.3 (Frost and Ashby [24]) shows the creep deformation map for 316H steel. Diffusion creep is dominant at lower values of applied stress whereas at high stress level dislocation creep overshadows diffusion creep. A comprehensive overview of creep mechanisms is also presented in the work by Nabarro and deVilliers 1995 [25].

Diffusion creep is caused by the transport of atoms through the lattice structure of the crystal. In diffusion creep, crystalline defects generally migrate in the direction of higher compressive stress within a crystal under an externally applied load. This creates a net mass transfer which shortens the crystal in the direction of maximum compression. For 316H steels, diffusion creep is characterised by the migration of vacancies (Evans and Wilshire [26]). There are two types of diffusion creep: Nabarro-Herring creep (Herring [27]) and Coble creep (Coble [17]). In Nabarro-Herring creep, vacancies migrate within the grains whereas in Coble creep, vacancies migrate along the grain boundaries as shown in figure 2.4 (Babu [28]).

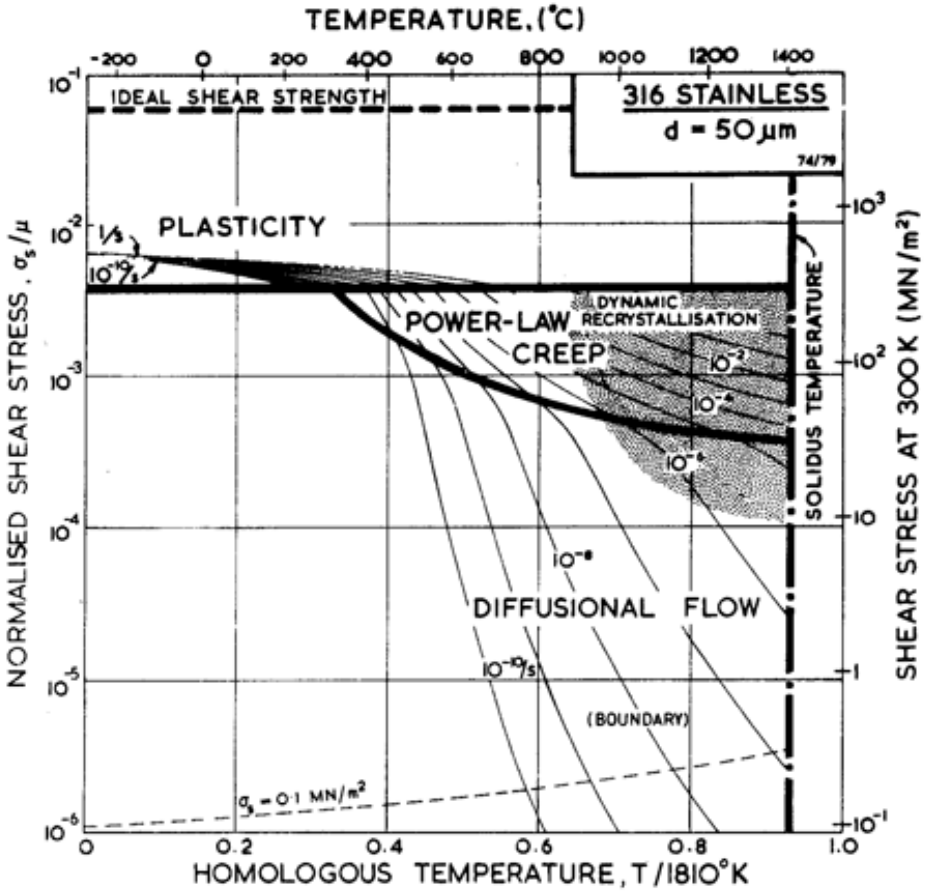

Figure 2.3: A map of creep deformation mechanisms of 316H steel with 50μm grain size (Frost and Ashby [24])

At higher stress levels, diffusion creep theories fail to explain the creep mechanism of metals. Experimental results suggest that creep at high stress levels occurs due to the movement of dislocations. Crystalline materials contain dislocations. During metal deformation under an applied stress, dislocation creep can occur by gliding along a plane. On encountering obstacles, the movements of the dislocations are arrested resulting in dislocation 'pile up'. Back stresses are generated due to dislocation pile up which balance the externally applied forces thus contributing to work hardening. When the work hardening fully compensates for the dislocation movement due to the external forces, the creep rate becomes constant i.e. primary creep ends and secondary creep starts. If the temperature is high enough, the dislocations, due to a higher amount of thermal energy, can climb over obstacles (Evans and Wilshire [29]). A schematic of the dislocation climb and glide processes is shown in figure 2.5.

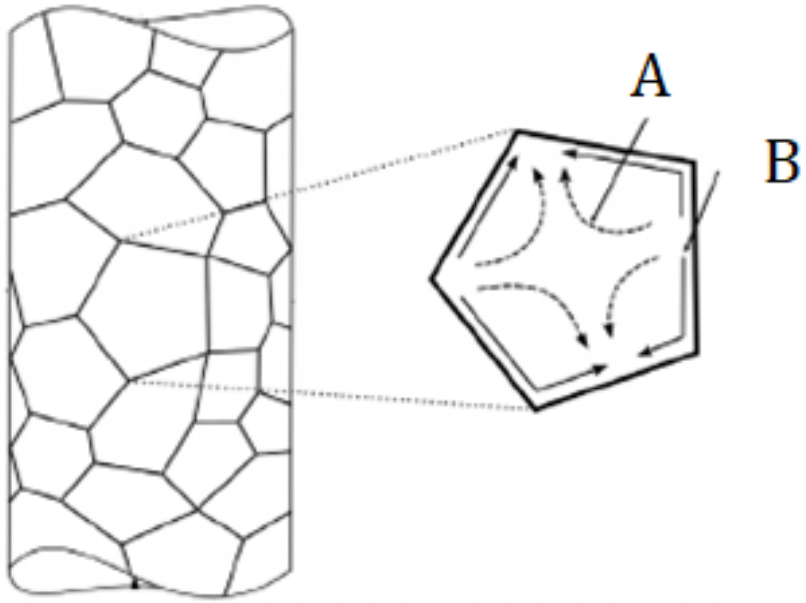

Figure 2.4: Schematic showing A) Nabarro-Herring and B) Coble Creep (Babu [28])

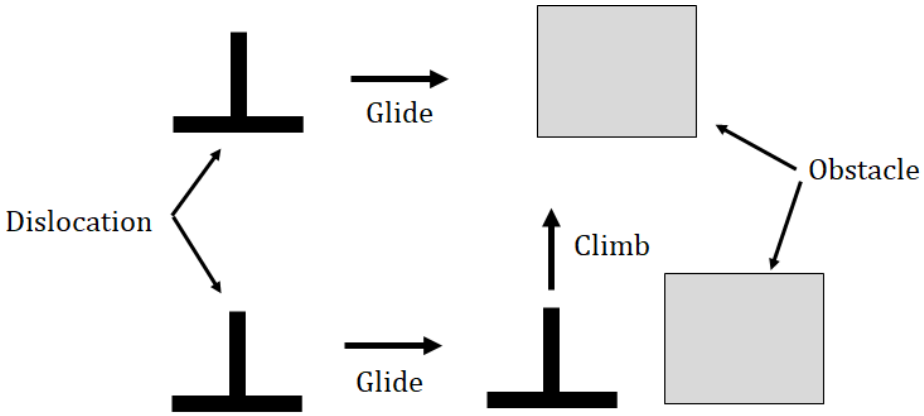

Figure 2.5: Schematic showing dislocation creep mechanisms

Creep damage accompanies creep deformation due to the formation of voids and micro-cracks. The formation and coalescence of voids and micro-cracks drive tertiary creep deformation when the creep rate exhibits an increasing trend leading to creep fracture. Applied stress and temperature along with material parameters such as grain size affect creep fracture (Ashby et al 1983 [30]). In 316 steels, creep fracture can be of two types: inter-granular fracture (either due to wedge type cracks or formation and coalescence of voids) and trans-granular fracture (Tabuchi et al 1990 [31]).

Operating stress levels in steam generator components are generally much below 100MPa. However, conducting creep experiments at such low stress levels is impractical due to the long time scales required for such tests. Therefore, creep tests on 316H material are generally conducted at high stress levels resulting in realistic test times and where dislocation creep is dominant for temperatures above 400°C (figure 2.3). Also, it can be seen from figure 2.3 that extrapolation of short term creep test data for lower stresses at 550°C would result in over estimation of creep rates and hence will remain conservative. For a creep temperature of 550°C and a stress range of 250-400MPa, power law creep remains dominant. The applied stresses used in this work were within 250-400MPa.

2.2.3 Dependence of Creep on Stress and Temperature

In general, the steady state creep rate is loosely called as the creep rate (Nabarro and deVilliers 1995 [25]) by ignoring the contributions of primary and tertiary creep stages. For isothermal conditions, the dependence of creep strain rate is a power law function of the applied stress represented as:

$$\dot{\epsilon}_c \propto \sigma^n \tag{2.1}$$

where, $\dot{\epsilon}_c$ is the creep strain rate, σ is the applied stress and n is the stress exponent. In the power law regime, for metals, the value of the stress exponent n is 3 while for pure metals it is between 4 and 5 and for stainless steels it is greater than 5 (Nabarro and deVilliers 1995 [25]). An exponential form represents the stress dependence of creep at higher stress when the power law breaks down.

$$\dot{\epsilon}_c = A' e^{\beta\sigma} \tag{2.2}$$

where $A^{'}$ and β are constants independent of stress but dependent on temperature.

Thermodynamics and solid-state rate processes govern the temperature dependence of creep. That is why an exponential form is often used to represent the temperature dependence of creep. Arrhenius equation is popularly used to represent the temperature dependence of creep:

$$\dot{\epsilon}_c = \gamma e^{\frac{-Q}{RT}} \tag{2.3}$$

where $\dot{\epsilon}_c$ represents the creep rate, Q is the creep activation energy, T is the creep temperature, R is the universal gas constant and γ is a material constant. As can be observed, the creep rate exponentially rises for an increase in temperature. Generally 3 or 4 ranges of creep behaviour is observed in metals based on their melting points (McLean 1966 [32]):

- $0 < T < 0.3T_{melt}$: transient logarithmic creep
- $0.3T_m < T < 0.9T_{melt}$: engineering creep range
- $0.9T_m < T < T_{melt}$: diffusional creep

where T is the creep temperature and T_{melt} is the melting point of the metal.

2.2.4 Creep Models for 316H Steel

Uniaxial creep deformation in 316H steels is best described by the Bailey-Norton equations for primary and secondary creep (Odquist and Hult [33]):

$${\epsilon_c}^p = C_1 t^{C_2} \sigma^{n_1} \tag{2.4a}$$

$${\epsilon_c}^s = C \sigma^n t \tag{2.4b}$$

where, ${\epsilon_c}^p$ is the creep strain accumulated during primary creep stage, ${\epsilon_c}^s$ is the strain accumulated during secondary creep, σ is the applied uniaxial stress and t is time. C_1, n_1, C_2, C

Temperature ($^{\circ}C$)	C_1	C_2	n_1	C	n
550	2.9618E-12	0.42131	4.18	5.2900E-26	8.2

Table 2.1: RCCM-R model constants for 316H steels

Confidence Limit	Secondary Creep	Primary Creep
Lower 95%	$0.1519C$	$0.1413C_1$
Upper 95%	$6.5830C$	$7.0754C_1$

Table 2.2: 95% confidence limits on creep constants for 316H RCCM-R model

and n are temperature dependent constants. The first equation defines primary creep strains as a function of time and the second equation defines the accumulation of secondary creep strains with time.

The above equations, when presented in terms of creep strain rates instead of creep strains, can be expressed either in the time or stress hardening form. Equations 2.5 represent the time hardening form and 2.6 represent the strain hardening form.

(2.5a) $$\dot{\epsilon_c}^p = C_1 C_2 t^{C_2-1} \sigma^{n_1}$$

(2.5b) $$\dot{\epsilon_c}^s = C\sigma^n$$

(2.6a) $$\dot{\epsilon_c}^p = {C_1}^{\frac{1}{C_2}} C_2 {\epsilon_c}^{p\,\frac{C_2-1}{C_2}} \sigma^{\frac{n_1}{C_2}}$$

(2.6b) $$\dot{\epsilon_c}^s = C\sigma^n$$

One of the creep models extensively used for 316H steels is the RCCM-R model (RCCM-R code [34]) which is based on the above equations. The creep constants for 316H as cited in RCCM-R are presented in table for a temperature of $550^{\circ}C$ (Chen et al [35], R66 Materials Handbook [36]). The values presented in table 2.1 are mean properties while table 2.2 presents the lower and upper bound creep coefficients for primary and secondary creep (R66 Materials Handbook [36]).

2.2.5 Effects of multi-material creep rates on stress and strain distributions in a weldment

Creep deformation and failure of weldments is a major life limiting factor for power plant components (Zeravcic et al [37]). Prediction of creep deformation and damage in weldments is

complicated by the presence of different metallurgical zones in a weldment. Creep damage in weldments is influenced by the ductilities and creep strengths of its constituent metallurgical zones (Manjoine [38], Storesund et al [39], Eggeler et al [40]). Creep strength of a material is generally measured by its rupture stress for a given creep time and creep temperature. Also, the multiaxial creep ductility of a material is a function of the uniaxial creep ductility of the material as well as the multaxiality of the state of stress. Both creep strain evolution as well as stress multiaxiality in a weldment are affected by the degree and extent of creep mismatch between the constituent materials. Effect of creep mismatch on stress multiaxiality was studied by Tu et al [41], Tu and Sandstrom [42], Craine and Newman [43] and Storesund et al [39]. Creep design codes and methods generally assume that the creep strength of a weldment is limited by the creep strength of the weld metal (the R5 method [2], ASME Code Case N47-29 [44]). This is to ensure that the creep strength of the weld metal should not reduce the overall strength of the weldment calculated using the parent properties. A fundamental assumption in such a treatment is that the interaction between the different creep properties of the weldment constituents is insignificant. Simplified estimates of weldment creep strength by using relative creep and rupture strengths of the base metal and the weld metal are used in these engineering assessment methods. An important concern was a lower creep strength of the weld (Mayer et al [45], Segle [46]). However, due to complex interactions between the creep strain rates in the different material zones and in particular between the parent and the weld metal (Storesund et al [39], Craine and Newman [43], Segle et al [47]), it has been found in earlier studies that the creep life of the weld can vary significantly from the rupture lives of it's constituents (Samuelson et al [48]). Major analytical (Manjoine [38], Hall and Hayhurst [49], Tu and Sandstrom [42], Tu et al [50]) and experimental work (Coleman et al [51]) have been undertaken in the past where weldment creep strength reduction factors were defined and evaluated by considering different material zones in a weldment.

Creep mismatch between the constitutive material zones in a weldment can manifest itself as strain and stress concentration effects which change the stress and strain distribution in a weldment subjected to creep. In the present context, a stress concentration factor (SCF) is defined as the ratio of the peak stress at a weld interface divided by the nominal stress in the weldment. The nominal stress is the stress which will exist in a homogeneous material under the same loading conditions. A considerable amount of work in the past has been directed towards

working out stress concentration factors (SCF) arising out of creep mismatch in a weldment. Ivarsson and Sandstrom [52] studied the creep rupture of butt-welded AISI316 steel tubes and correctly predicted the observed creep rates, rupture times, positions and orientations of cracks, and a rupture ductility of the right order of magnitude. Browne et al [53] studied the rupture behaviour of $\frac{1}{2}Cr\frac{1}{2}Mo\frac{1}{4}V$ steel tubes by representing the tubes as a three material model with weld, HAZ and parent as it's constituents. It can be seen that most of the earlier work concentrated on the behaviour of tube to tube butt welded joints under internal pressure. It was generally predicted that there will be considerable redistribution of the hoop stress and not necessarily the axial stress. Hyde and Sun [54] studied the distribution of stress across the centreline of a crossweld specimen subjected to creep. Samuelson et al [55] studied strain concentrations in a circumferential pipe weld using finite element modelling. Wada et al [56] studied creep-fatigue behaviour of a 304 weldment by using a strain concentration factor to take into account metallurgical discontinuity effects and thereby proposed a simplified creep-fatigue evaluation procedure for weldments by using only the parent properties. Samuelson et al [48] used a three material model (weld, HAZ and parent) to show that stress concentrations due to creep mismatch can also be influenced by the weld geometry and the relative extent of the HAZ. Chellapandi and Chetal [57] identified stress concentration factors in a dissimilar metal weld as a function of the applied stress level, weld angle and the level of mismatch using finite element modelling. Li et al [58] identified that both creep strain concentrations as well as stress multiaxiality arising out of creep mismatch impacted creep damage evolution in a Mod.9Cr,Äì1Mo steel weld. Also, a number of creep crack growth studies for heterogeneous weldments were conducted by various researchers such as Segle et al [59], Tu et al [60].

Although the work by Samuelson et al [48] and later by Chellapandi and Chetal [57] provided a better insight into the effects of creep mismatch on stress and strain concentrations, the work did not consider the problem of stress singularity associated with bi-material interfaces in numerical simulations. Incompatibility of lateral strains at bonded interfaces of two different materials results in a stress singularity at the free surface of the interface. Such incompatibility can arise due to elastic, elastic-plastic or creep mismatch across a bonded interface. Therefore, it is essential to consider singularity effect in multi-material creep models in order to derive any meaningful estimation of real stress and strain concentrations. Considerable work on the nature of singularity at the bonded interface of two elastic material (Hein and Erdogan [61],

Reedy [62], Bogy [63], Bogy et al [64], Dunders [65], Fr*ä*nkle et al [66], Niu et al [67], Qian et al [68], Ro et al [69], Desmorat et al [70], Dempsay and Sinclair [71], Dempsay and Sinclair [72], Wu [73] and Munz and Yang [74]), elastic-plastic material (Wang [75], Xu et al [76], Van Lich et al [77] and Rahman [78]) and elastic-creep material interfaces (Kitamura et al [79] and Ngampungpis et al [80]) have been done in the past, where the strength and extent of the stress singularity at the free edge of a bi-material interface was analysed and related to the level of mismatch and geometry of the interface. Wu [81] studied stress concentrations in a bi-material joint free of stress singularities. The most recent and relevant work with respect to the context of this thesis was done by Hyde and Sun [82]. Hyde and Sun [82] investigated the nature of singularity at the interface of an axisymmetric cross-welded specimen arising out of the weld geometry (weld aspect ratio, type and shape of the weld etc.) and the mismatch in power law creep coefficients between the parent and the weld. Hyde and Sun [82] also discussed on the area around the singularity point where the effect of the singularity will be significant. This was termed as the singularity zone and was defined in the paper as the maximum radius from the location of singularity where the equivalent stress is greater or equal to twice the nominal stress in the component. The choice of twice the equivalent stress was primarily influenced by the general range of stress concentration factors arising out of geometrical discontinuities. The intention was probably to show that for certain cases, it is possible that the singularity zone sizes will be in the order of microstructural features and hence will not exist in a real component. However, there still exists the lack of a comprehensive method for interpreting numerical results for a bi-material creep analysis in order to extract realistic information on stress and strain concentrations by masking the interface edge effects due to stress singularity.

2.3 Creep Testing

2.3.1 Impression Creep Test

Impression creep test is a localised creep test where an indenter is pressed against the test specimen with a specified pressure at the creep temperature. The depth of indentation of the indenter is then related to the creep strain accumulation in the test specimen. Thus, impression creep curves can be directly compared with creep curves obtained by conventional testing. It is a modification of indentation creep tests, where a flat face is used for the indenter contacting

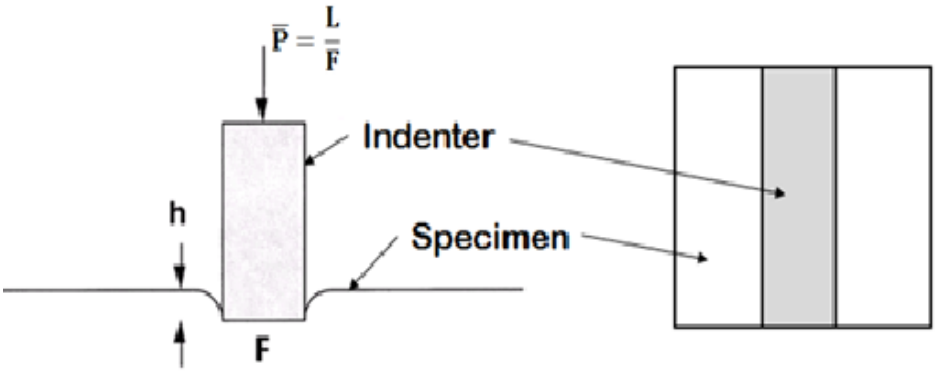

Figure 2.6: Schematic showing the principle of impression creep and important geometrical parameters of a typical impression creep test

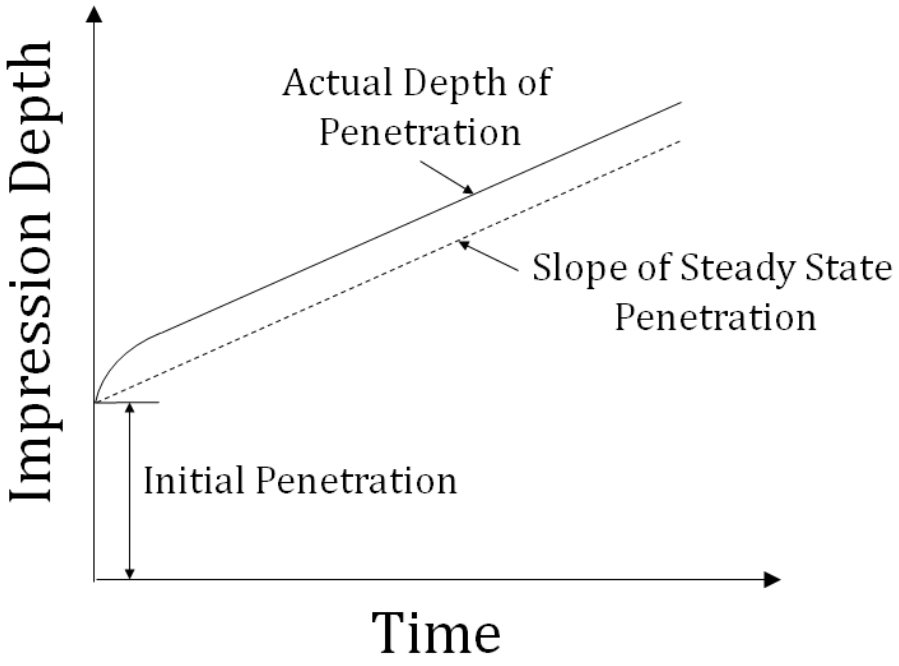

Figure 2.7: Typical impression depth versus time curve for an impression creep test

surface as shown in figure 2.6. This makes the applied stress constant through the test unlike an indentation test. Some of the earliest accounts of impression creep testing can be found in Chu et al [83], Yu and Li [84], Yu and Li [85], Chu et al [86] and Gibbs et al [87]. Figure 2.7 shows a typical impression depth versus time curve for an impression creep test.

Conventional creep testing is good for accurate creep measurements for standard sized creep samples but cannot be used in cases where only a limited number of samples can be made using

the available material or where localised creep properties are needed to be investigated. Other localised creep tests such as indentation creep suffered from the fact that due to the shape of the indenter, the applied load (stress) does not remain constant or steady, thereby making the interpretation of results extremely difficult to interpret against the available conventional creep data. For a flat cylindrical indenter, Yu and Li [85] showed that for a power law steady state creep constitutive relationship between the von Mises equivalent stress and creep strain rate, the impression velocity of the indenter is related to the punch stress by the same power law. Yung et al [88] later showed that the impression velocity maintained a hyperbolic sine relationship with the punch stress if the creep constitutive relationship was a hyperbolic sine law. This meant that irrespective of the creep constitutive relationship used, the impression velocity followed the same relationship with the punch stress and therefore it was possible to convert impression creep results to conventional creep tests.

All the earlier authors such as Chu et al [83], Yu and Li [85], Chu et al [89], Yu et al [90] and Tasnadi et al [91] have followed a trial and error approach to find empirical conversion factors relating the average punch stress '$\bar{P}$' and steady state impression velocity '$\dot{\delta}_{ss}$' of an impression creep test to the uniaxial stress 'σ' and steady state creep strain rate '$\dot{\epsilon}_c$' in a conventional creep test respectively. Hyde et al [92] developed a sound reference stress based approach for obtaining conventional creep data from an impression creep test. The conversion relationships can be written as:

$$\sigma = \eta \bar{P}, \tag{2.7a}$$

$$\dot{\epsilon}_c = \frac{\dot{\delta}_{ss}}{\beta d}, \tag{2.7b}$$

where η and β are the stress and strain rate conversion factors respectively and d is the indenter diameter. Hyde et al [92] confirmed that these conversion factors are independent of material properties and are only a function of geometry of the indenter and the test specimen.

Due to its ability to determine approximate minimum creep rates within small regions of material, impression creep test became a common tool for measurement of creep rate variation in weldments, where the minimum creep rate can drastically vary within small regions of the HAZ. Several authors applied impression creep testing to study weldments, the most notable ones are:

Gibbs et al [87], Gibbs et al [93], Hyde et al [94], Yu et al [95], Imam et al [96], Lisin et al [97], Sastry [98] and Hyde et al [99].

There are some important points which should be considered while interpreting impression creep data. Firstly, in most cases, the penetration rate or impression velocity of the indenter never becomes constant in an actual test. One way to extract the minimum or steady state velocity is to plot the impression velocity against inverse time and then fitting a straight line to the points. The extrapolation of this straight line to time = ∞ or inverse time = 0. This method was used by Hyde et al [92]. Another way of interpreting the data is to plot the impression depth versus time for higher time values and fitting a straight line through those points. The slope of the straight line will give the steady state impression creep velocity.

2.3.2 Digital Image Correlation based Strain Measurement

Digital image correlation (DIC) technique is a non-contact method of measuring 2D and 3D surface deformations in a test specimen by tracking changes in a series of images of the specimen. It enables full field measurement of displacement and strain fields spanning the gauge area of test specimens. It has been successfully used by researchers to study strain variation in crossweld tensile test specimens at room temperature (Boyce et al [100], Acar et al [101], Reynolds and Duvall [102], Acar et al [103], Acar [104]). The DIC technique is based on the principle of using computational algorithms to measure shifts in image data sets of test specimens. In mechanical testing, displacement fields and subsequently strain fields are measured by tracking changes in image intensity patterns of images taken before and after an event of loading producing surface deformation.

The first application of DIC technique to high temperature measurements was demonstrated by Lyons et al [105] where free thermal expansion and tensile strains were measured on Inconel 718 specimens at temperatures up to 650°C. They used a coating of Aluminium Oxide and Boron Nitride was used for creating the speckle patterns, in order to inhibit oxidation of the specimen surface at high temperature. Also, high quality glass was used for the furnace window in order to reduce image distortion and a small fan was used to mix the hot air between the furnace window and camera in order to reduce the effects of thermal currents and maintain a constant refractive index. A good accuracy of thermal as well as tensile strain measurements was achieved. Liu et al [106] later used to same test set up to conduct high temperature DIC based fracture tests on

notched Inconel 718 specimens at 650°C and 704°C. For the first time, theoretical elastic and visco-elastic results for strains around a crack tip were successfully compared to experimentally obtained strain field data.

A an optical system was developed by Maharaj, al [107], Morris et al [108], Morris et al [109] in order to measure creep strains in power generation plants in the UK. It used a combination of DIC and an optical strain measurement system called Auto-Reference Creep Measurement and Control (ARCMAC). A pair of optical gauges were used in the system for monitoring point-to-point changes in strain across pipe welds. The system used DIC to monitor the separation of two circular markers on two separate Inconel plates. Although the system used DIC technique to successfully determine strains by tracking point-to-point marker separations, it could not be used for full field strain measurements.

2.3.2.1 Principle of Digital Image Correlation

Digital Image Correlation (DIC) can best be described as a pattern matching technique that maps images of a test specimen at different stages of its deformation in order to extract information such as deformation vector field or strains in the specimen. The reference image is divided into smaller regions called subsets and each of these subsets are then tracked through the different stages of deformation. Software such as LaVision [110] and Dantec [111] employ various computation algorithms to perform tracking of the subsets. In order to ease identification of the subsets through the deformation stages of the test specimen, a distinct identifiable pattern is needed on the surface of the test specimens, which can either be some naturally occurring pattern like visible surface roughness or artificially created using a paint or coating called speckle patterns. The principle of tracking speckle patterns using DIC is illustrated in figure 2.8 (Zhang and He [112]). In figure 2.8, the random pattern of black dots on the white surface is the speckle pattern. Sometimes natural features present on specimen surfaces can be used as a speckle pattern. However, in most cases, in order to enhance image contrast, artificial speckle patterns are created using spray painting. Figure 2.8 shows the tracking of speckle pattern by a subset (red box in figure 2.8, Zhang and He [112]) during deformation. Cross correlation functions are used to determine the location of the centre of each subset after deformation. Vector fields of displacement are then computed from the change in distances between the centres of each of these subsets during deformation. Strain fields are then calculated from the displacement fields

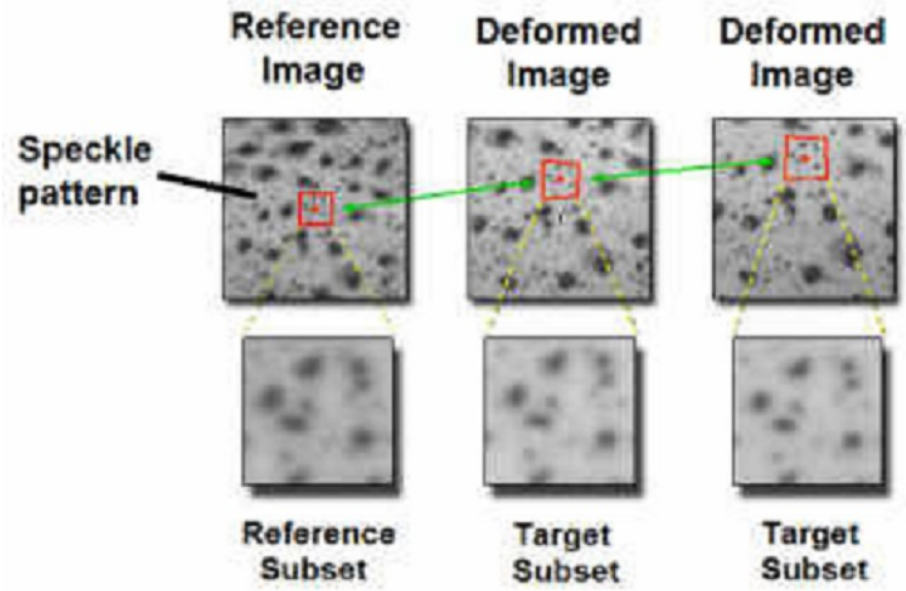

Figure 2.8: Principle of Digital Image Correlation (Zhang and He [112])

by fitting smooth surface patches over the displacement fields and differentiating.

Each image taken by a camera corresponds to a unique load or time step. In a camera, photographs are taken using a pixel array and then converted to an analogue signal. For analysis of image data using computational methods, the signal is re-converted to a digital signal. 24-bit RGB (Red, Green and Blue) images can be converted to 8-bit grey scale images where the intensity value at each pixel can range from 0 to 2^8 i.e. 256. On the grey scale, the lowest value of of image intensity represents black whereas the highest value is white. The speckle pattern on the specimen surface reflects light which is corresponds to a discrete value of image intensity at each pixel location. By comparing the image intensities for a subset in two different images, DIC technique can then determine the translation of the centre of that subset between the two images. This is done for all the subsets in a given image.

In order to track a subset in an image after deformation, a similar luminance distribution as of the reference image subset is searched in the new image. A correlation function is used by this method, the value of which depicts how close the light intensity distribution is, between two images and for each subset. In DIC, the different types of correlation functions are used. Equations present the magnitude of intensity difference function (C) and the normalised cross correlation function (NCC).

$$C(x,y,\hat{x},\hat{y}) = \sum |F(x,y) - G(\hat{x},\hat{y})| \tag{2.8a}$$

$$NCC(x,y,\hat{x},\hat{y}) = \frac{\sum F(x,y)G(\hat{x},\hat{y})}{[\sum F(x,y)^2 \sum G(\hat{x},\hat{y})^2]^{\frac{1}{2}}} \tag{2.8b}$$

The sum of absolute value of intensity differences between image intensities for two different images is calculated by the first function in equation 2.8, where, the grey scale value of light intensity at image location (x,y) of the initial image is $F(x,y)$ and the grey scale value of at $(\hat{x},\hat{y})$ of the deformed image is $G(\hat{x},\hat{y})$. The aim is the minimisation of the function $C(x,y,\hat{x},\hat{y})$.

Normalised cross correlation function (equation 2.8), which represents similarity of two images, is the more common of the two. In this case, the value of the function ranges between -1 and 1. The highest correlation, in this case, is indicated by the maximum value of the correlation function. In a standard DIC data analysis software such as the LaVision Davis software [110], there is an option of selecting any of these functions along with others.

Thus, using a correlation function, every subset $F(x,y)$ in the reference image is mapped to a deformed subset $G(\hat{x},\hat{y})$ in the new image. The next step is the calculation of a deformation field explained in the following sub-section.

2.3.2.2 Deformation Field

Once a subset in the reference image is mapped to a deformed subset in the new image, the displacement of the centre of the subset between the reference and the target image is given by:

$$\begin{bmatrix} c_u \\ c_v \end{bmatrix} = \begin{bmatrix} c_{\hat{x}} \\ c_{\hat{y}} \end{bmatrix} - \begin{bmatrix} c_x \\ c_y \end{bmatrix} \tag{2.9}$$

where, $(c_x,\ c_y)$ are the coordinates of the subset centre for the reference image, $(c_{\hat{x}},\ c_{\hat{y}})$ are the subset centre coordinates for the deformed image and $(c_u,\ c_v)$ is the displacement vector of the subset centre between the reference image and the test image.

In order to determine the displacement of a point P in the reference subset, it is required to make assumptions regarding the deformed shape of the subset in the target image. For requirements of continuity, neighbouring points in the reference subset will remain as neighbours in the target image. Therefore, a point $P(x,y)$ in the reference subset can be mapped to a point

$\hat{P}(\hat{x},\hat{y})$ in the target subset (fig) by using shape functions $\zeta(x,y)$ and $\eta(x,y)$ (ref) as shown in the following equations:

$$\begin{bmatrix}\hat{x}\\ \hat{y}\end{bmatrix} = \begin{bmatrix}x+\zeta(x,y)\\ y+\eta(x,y)\end{bmatrix} \tag{2.10}$$

For a rigid body displacement, the distance between the point $P(x,y)$ and the centre of the subset $C(c_x,c_y)$ in the reference image remains constant and can be determined by zero order order shape functions:

$$\zeta(x,y) = c_u \tag{2.11a}$$

$$\eta(x,y) = c_v \tag{2.11b}$$

Thus for rigid body motion, the displacement of any point in the reference subset is equal to the displacement of the centre of the subset. For constant strain assumption for each subset, a first order shape function is used, which is in essence, considering the first two terms in the Taylor expansion of the displacement of the subset centre $C(c_x,c_y)$.

The new coordinates of any point in the deformed subset is then given by:

$$\begin{bmatrix}\hat{x}\\ \hat{y}\end{bmatrix} = \begin{bmatrix}x+c_u+\frac{\partial c_u}{\partial x}(x-c_x)+\frac{\partial c_u}{\partial y}(y-c_y)\\ y+c_v+\frac{\partial c_v}{\partial x}(x-c_x)+\frac{\partial c_v}{\partial y}(y-c_y)\end{bmatrix} \tag{2.12}$$

The deformation mapping for the first order shape function (constant strain) is illustrated in figure 2.9, where the displacement vector of a point P in the reference subset to the point $\hat{P}$ in the deformed subset is derived from the displacement vector of the centre of the subset and the relationship between the location of the point P to that of the subset centre C. A first order Taylor series approximation is used in this case, which assumes a constant strain in the deformed subset. Higher order approximations can be made to derive the displacement vector field for better accuracy especially for cases with steep strain gradients or bigger subset sizes.

As mentioned above, a correlation criterion is used to evaluate the degree of similarity between the reference and the deformed subsets and is evaluated before a correlation analysis is performed. As can be seen from above, for a first order displacement or shape function, the

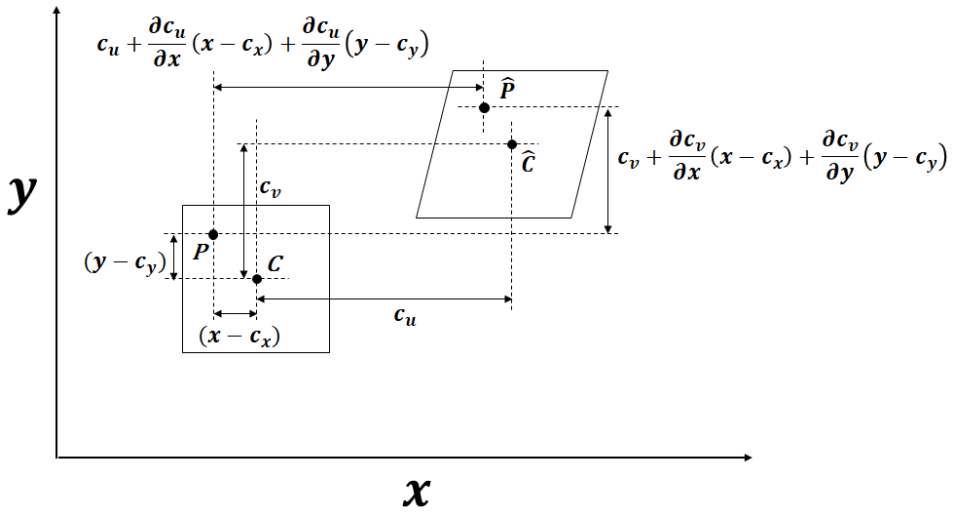

Figure 2.9: Schematic showing derivation of deformed coordinates of a Point in a reference subset using first order element shape function

correlation coefficient of the mapping is a function of the subset centre displacements (c_u, c_v) and displacement gradients, $\frac{\partial c_u}{\partial x}$, $\frac{\partial c_u}{\partial y}$, $\frac{\partial c_v}{\partial x}$ and $\frac{\partial c_v}{\partial y}$. The correlation coefficient is maximised by determining the values of this displacements and the gradients.

The Newton-Raphson method for solving a non-linear differential equations is frequently used to solve for the six unknown variables for minimisation of the correlation function C (equation 2.8) or maximisation of the function NCC (equation 2.8). The initial values for the six parameters is calculated using this iterative method. For the initial guess, a zero value of displacement gradient is used followed by the determination of the displacement gradients using the intensities determined by sub-pixel interpolation. Then the calculated displacement gradients are used to refine the values of the six variables (Bing et al [113], Bruck et al [117]).

As can be observed from equation, the deformed coordinates of a point $(\hat{x}, \hat{y})$ may not lie at a pixel location but in between pixels. Therefore, the image intensities of the points at these sub-pixel locations must be determined before evaluation of the correlation coefficient. This is done by interpolating the image intensities at these sub-pixel locations and is called sub-pixel interpolation.

2.3.2.3 Sub-pixel Interpolation

Various sub-pixel interpolation schemes can be found in literature such as bi-cubic interpolation, bi-linear interpolation, bi-quintic B-spline interpolation, bi-cubic B-spline interpolation and bi-cubic spline interpolation schemes. Books on computational methods such as (Grasselli and Pelinovsky [114], Lyche and Morken [115] and Gibb et al [116]) provide a detailed account of such schemes. However, Schreieret al[80]and Knausset al[49] highly recommend the use of higher order schemes such as bi-cubic spline interpolation as they provide better convergence and registration accuracy in comparison to the simple methods. For an 8x8 subset size, a typical intensity array with digitised values is depicted in figure 2.10 (Bruck et al [117]). The grey intensity values at a point $(\hat{x},\hat{y})$ are interpolated by using a bi-linear scheme (figure 2.11). The four neighbouring pixel locations have image intensities $\hat{P}(i,j)$, $\hat{P}(i+1,j)$, $\hat{P}(i,j+1)$ and $\hat{P}(i+1,j+1)$ where i and j are the pixel coordinates. The grey value of a location $\hat{P}(\hat{x},\hat{y})$ in between these neighbouring pixel is then calculated by the following equation:

$$\hat{P}(\hat{x},\hat{y}) = c_{00} + c_{10}(\hat{x}-i) + c_{01}(\hat{y}-j) + c_{11}(\hat{x}-i)(\hat{y}-j) \tag{2.13}$$

where c_{00} is the grey level of pixel location $(i+1,j)$, c_{10} is the difference of grey level of pixel location $(i+1,j)$ and c_{00}, c_{01} is the difference of grey level of pixel location $(i,j+1)$ and c_{00} and c_{11} is equal to the difference of grey level of pixel location $(i+1,j+1)$ and $(c_{00} + c_{10} + c_{01})$.

Thus, the neighbouring point pixel intensities are used to determine the bi-linear constants c_{00}, c_{10}, c_{01} and c_{11}. The intensity surface map after bi-linear interpolation is shown in figure 2.12 (Bruck et al [117]).

There are several interpolation methods for pixel intensity values to fit the image surface Bruck et al [117], Schreirer et al [118].

2.3.2.4 Measurement of Deformation Field

The discrete nature of DIC images renders displacement calculation with a minimum accuracy of one pixel readily possible. Sub-pixel interpolation algorithms should then be used to improve the measurement of displacements [81]. Therefore, 2D DIC implementation consists of two steps, an initial guess of deformation and measurement of sub-pixel displacements. An accurate initial guess is important as convergence most commonly used correlation optimisation algorithms such

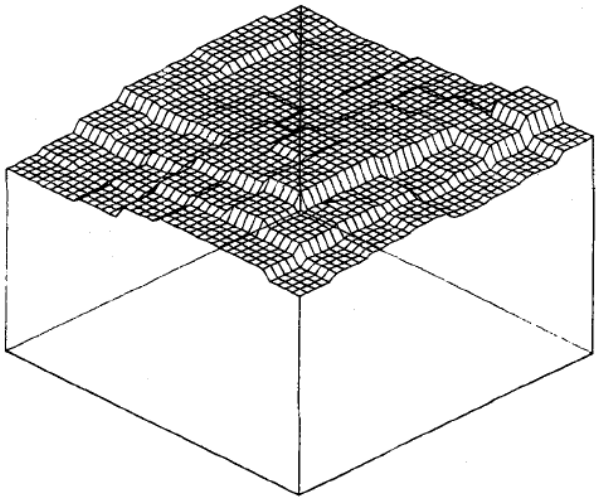

Figure 2.10: Sample of un-interpolated intensity data for an 8x8 subset (Bruck et al [117])

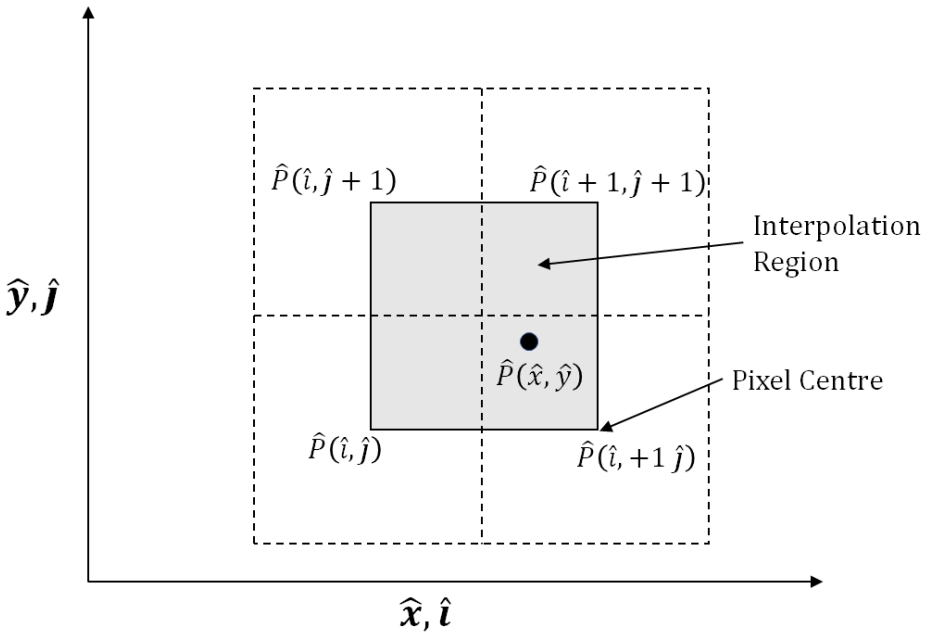

Figure 2.11: Schematic showing the location of pixels and the area over which interpolation is done

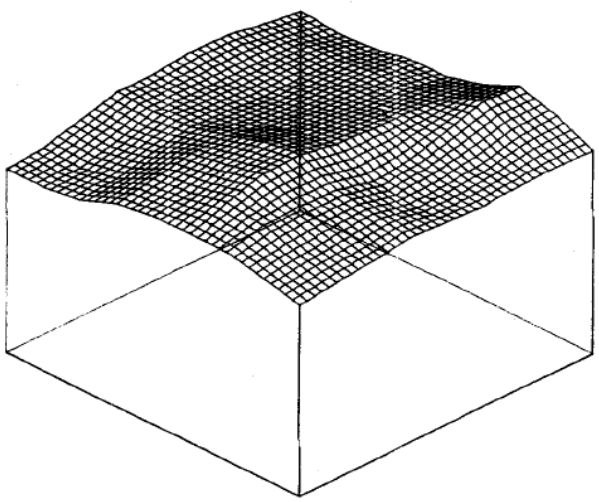

Figure 2.12: Sample of interpolated intensity data for an 8x8 subset (Bruck et al [117])

as the Newton-Raphson method, depends heavily on the initial guess. Vendroux and Knauss [60] showed that the Newton-Raphson method has a convergence radius of less then 7 pixels. In the following paragraphs, algorithms commonly used for initial estimation and sub-pixel registration are discussed.

An initial estimation for the displacement field with with a one pixel accuracy can be performed using a simple searching technique, either in the spatial or the frequency domain. Fine search routines such as the coarse to fine can be used in the spatial domain for determining the actual locations of the target subsets. Alternatively, in the frequency domain, Fourier transforms can be used for implementing the correlation between the reference and deformed subsets. In this work, Fourier transforms were used for initial estimation of pixel displacement fields as they are computationally fast and accurate for small rotations between the reference and the target images (Schalkoff [119]).

Any function of time can be decomposed into it's constituent frequencies using Fourier transforms (Marks and Robert [120] and Rayner [121]). The Fourier transform of a function $f(t)$ is mathematically defined as:

$$F(f) = \int_{-\infty}^{\infty} f(t) e^{-2\dot{\pi} i f t} dt \tag{2.14}$$

Thus, a Fourier transform of a time function $f(t)$ is a function $F(f)$ of frequency f. Also, the function $f(t)$ can be expressed as an inverse Fourier transform of $F(f)$ as follows:

$$f(t) = \int_{-\infty}^{\infty} F(f) e^{2\pi i f t} df \tag{2.15}$$

Using Euler's equation, the Fourier transform $F(f)$ can be decomposed into a real and an imaginary part (Wilson [122]):

$$F(f) = \int_{-\infty}^{\infty} f(t)[cos(2\pi f t) + isin(2\pi f t)]dt \tag{2.16}$$

In equation, the phase of the function is expressed by the real part and the amplitude of the function is expressed by the imaginary part. For a DIC image, the frequency of the magnitude of image intensity (brightness) is represented by the imaginary part whereas the contour or shape of the brightness distribution is represented by the real part [78]. In DIC pattern matching, an inverse Fourier transform is applied to only the imaginary part of the function to extract the image intensities. A method called Phase Only Correlation (POC), extensively used in medical applications, the image contour, as extracted from the real part is used [79].

After the initial estimation step, sub-pixel interpolation algorithms are used to refine the accuracy of DIC. Many different algorithms for sub-pixel registration such as course-fine search, peak finding, iterative spatial domain cross-correlation, spatial-gradient based algorithm, genetic algorithm and finite element and B-Spline algorithm are described in literature various literature. Correlation accuracy is affected by the sub-pixel interpolation scheme (Schreirer et al [118], Wang et al [123]). In the LaVision 8 DIC software program, a bilinear interpolation scheme is used by default. Although, this method eliminates noise with an acceptable sub-pixel accuracy, it results in the loss of some original image features. In other words, it results in over-smoothing of the image. In this work, image reconstruction for sub-pixel registration was performed using a non-linear interpolation scheme, namely, the Whittaker reconstruction algorithm [124]. In this algorithm, a low frequency wave is generated from the sampling pixels. This method has good sub-pixel accuracy in addition to removal of noise while avoiding any excessive smoothing. Thus, this method supports original image resoration without much loss of information (LaVision Davis 8 software [110]).

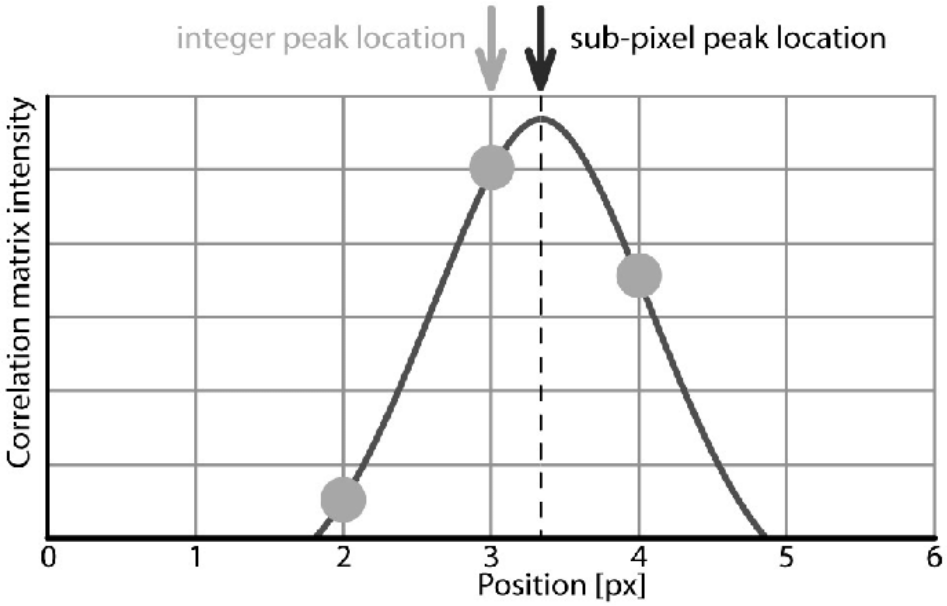

Figure 2.13: Example 3x3 Gaussian fit to image profile

A Gaussian weight function based method, along with sub pixel interpolation was used to increase deformation estimation accuracy. In this work, after initial deformation estimates were made with integer level pixel accuracy the correlation function was evaluated followed by the usage of either a bilinear or Whittaker interpolation scheme for sub-pixel registration (in DaVis [110]). A 3x3 Gaussian interpolation function was applied to the reconstructed images as shown in figure 2.13 (Thielicke [125]). A 3x3 grid was used for fitting the Gaussian bell curve to the data (3 points in DaVis [110]) for the correlation peaks. The Gaussian function is applied to both the reference and the target images before applying the correlation function. A convolution technique is then applied to determine the correlation peaks. The position of the correlation peak is determined by maximising the area overlap between the two functions.

2.3.2.5 Factors Affecting DIC Accuracy

The important factors affecting DIC test accuracy are environment, image acquisition technique and DIC image analysis using complex computational algorithms.

Environmental factors include but not limited to image speckle size and distribution, illumination, distortion from camera lens and convection currents resulting in change in refractive index of the air in between the test specimen and the camera lens. All these factors can affect

image contrast which is important as the image intensity function depends on it. A good image contrast is needed for accurate correlation. Different computational algorithms such as subset shape function, sub-pixel intensity interpolation Schreirer et al [118], Wang et al [123], Schreirer et al [126], Zhou et al [127] and optimisation techniques used for correlation peak. The speckle size of the image and the subset size selected for image analysis are the most dominant factors affecting the accuracy of DIC image analysis Ueda [128], Lecompte et al [129], Yaofeng et al [130]. A larger subset size generally aids in identifying two correlating subsets as it covers a larger area of speckle pattern and hence leads to a more reliable result. The dependence of accuracy of displacement vectors on subset size is shown in table (LaVision software [110]).

A large subset size generally leads to smaller errors but it compromises with the analysis resolution. So, if there are regions of steep gradients, accurate prediction of displacements is not possible with a large subset size. On the other hand, a suitable higher order displacement shape function can be used with a small subset to increase the accuracy of cross-correlation computation. The speckle pattern is also an important consideration for selection of subset size. The accuracy of measured deformation is significantly influenced by the number and size of the speckle pattern. Although a subset containing a relatively large number of speckles provides more information resulting in a high quality pattern matching, it can also lead to intensity noise on the determined displacements using correlation functions. Therefore, the optimal number and size of speckles in a subset is obtained based on the gradient of displacement. Both speckle pattern and subset size are therefore considered for achieving the best accuracy in DIC analysis. A reliable measurement requires a sufficient number of unique features or speckles in a subset. Subset size selection was proposed by Yaofeng et al [130] in order to calculate displacements in three test image pairs with different textures. This is illustrated in figure 2.14 (Pan et al [131]). For subset sizes ranging between 17x17 and 71x71 pixels, the standard deviation of errors for the displacement vector are shown in figure 2.15. The measured displacement standard deviation of error is mathematically defined as:

$$\sigma_d = \sqrt{\frac{1}{M-1}\sum_{i=1}^{M} {d_i}^2} \tag{2.17}$$

where displacement of a point i is d_i, M is the number of pixels and σ_d is the standard deviation of measurement error. σ_d represents the deviation of measurements from the mean

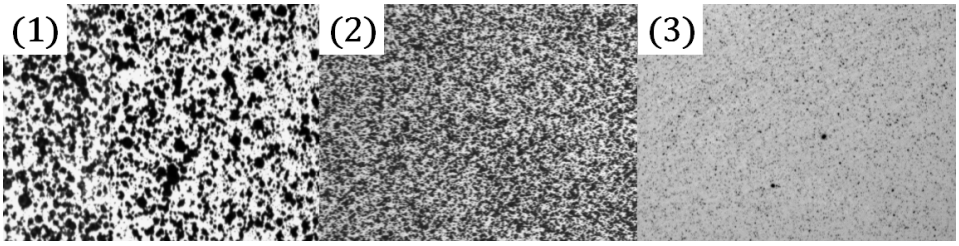

Figure 2.14: Example of reference images with three different decreasing speckle sizes: (1) > (2) > (3) (Pan et al [131])

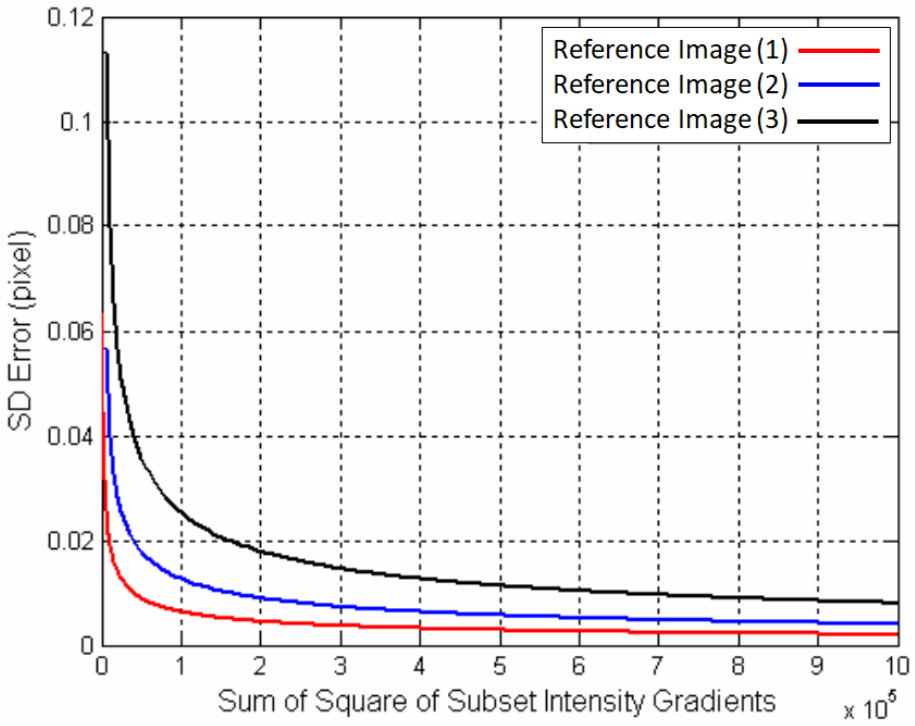

Figure 2.15: Standard Deviation of Error for the three reference speckle patterns in figure 2.14 (Pan et al [131])

value. From equation, it can be seen that as subset size decreases, σ_d increases. From figure 2.15, it can be observed that measurement error for image pair (3) are much larger than the other image pairs due to image contrast. A larger number of pixels are used in a larger subset increasing correlation accuracy. However, both subset size and the translation displacement obtained, affect measurement accuracy. For a 10-pixel displacement, the distance between the neighbouring points is shown in figure 2.15 (Pan et al [131]).

Affect of different camera zoom on accuracy was studied by Lecompte et al [129]. Figure 2.16

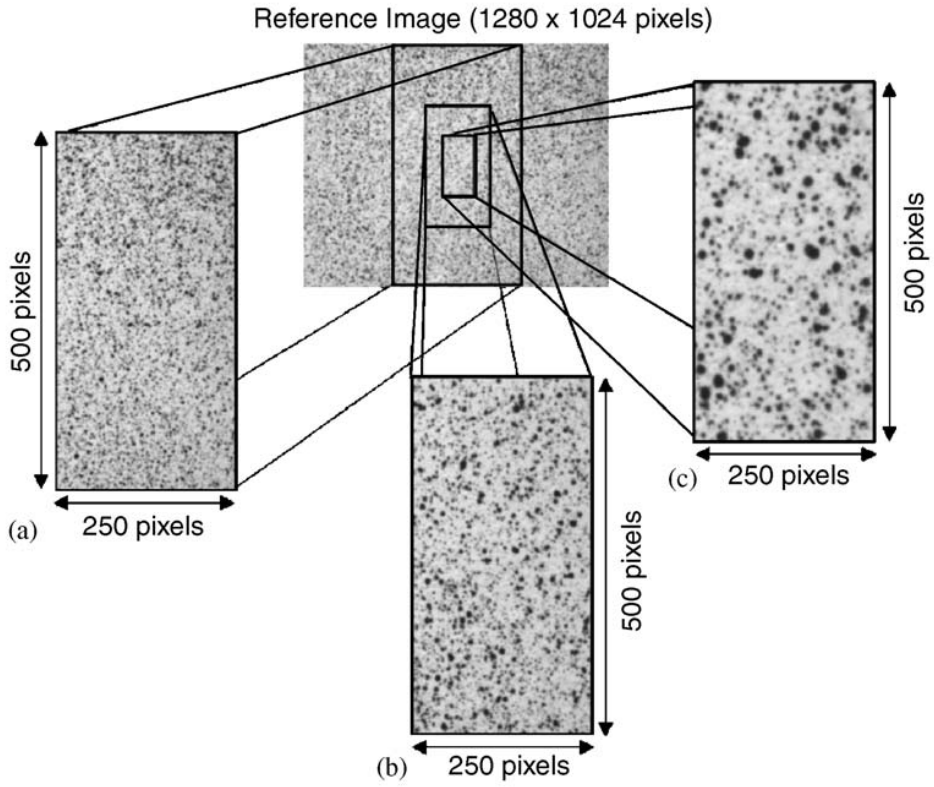

Figure 2.16: Example of effect of camera zoom for the same speckle pattern (Lecompte et al [129])

(Lecompte et al [129]) shows three speckle patterns with the same distribution and different camera zoom. In this case, it was found that accuracy of measurement increased with subset size.A good accuracy for a smaller subset is attributed to smaller speckle size. Therefore it can be said that the subset size selection for the same desired accuracy depends on the speckle size used, a larger speckle size for a larger subset and a smaller one for a smaller subset. In any DIC image analysis, a balance between the speckle size and subset size is struck to improve measurement accuracy.

2.4 Numerical modelling of Plasticity and Creep Using ABAQUS

In this work, commercial finite element software ABAQUS (ABAQUS 6.14 Documentation [132]) was used for numerical modelling of time independent creep and plasticity. Isotropic hardening option was used for time independent plasticity as the present work dealt with monotonic load

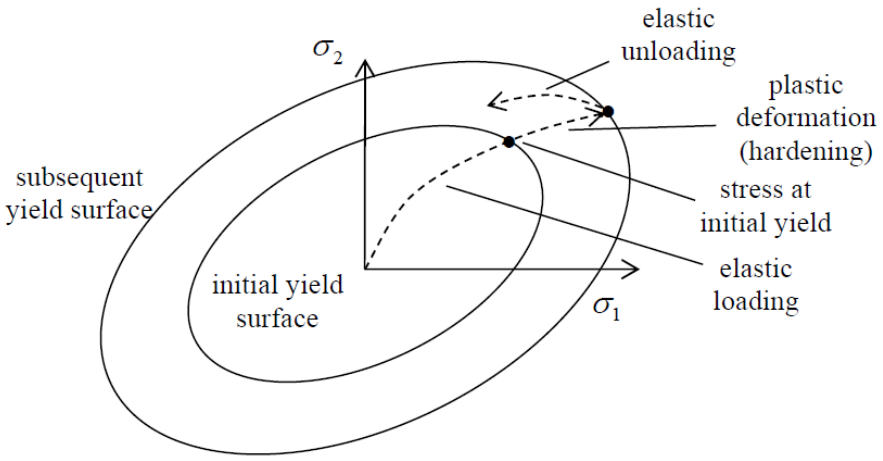

Figure 2.17: Schematic showing the growth of yield surface for isotropic hardening plasticity

cases. Isotropic hardening is generally used to describe the deformation hardening behaviour of material under monotonic loading Lee and Barkey [133]. For multiaxial plasticity, the yield surface for isotropic hardening is given by (Argon [134]):

$$f(\sigma_{ij}, K_i) = f_0(\sigma_{ij}) - K = 0 \tag{2.18}$$

where, $f_0(\sigma_{ij})$ is the initial yield function, K is a hardening parameter and σ_{ij} are the component stresses. Initial yielding for a von Mises stress function leads to the following expression for the initial yield function:

$$f_0(\sigma_{ij}) = \frac{1}{\sqrt{2}}\sqrt{(\sigma_1-\sigma_2)^2+(\sigma_2-\sigma_3)^2+(\sigma_3-\sigma_1)^2} \tag{2.19}$$

where, σ_1, σ_2 and σ_3 are the three principal stresses. Figure 2.17 shows a schematic of how the yield surface grows in case of isotropic hardening. The centre of the surface remains fixed while the surface increases in size.

In ABAQUS, a multi-linear fit to the stress strain curve can be provided as input along with a selection of isotropic hardening (Hibbit [135]).

For multi-axial creep, the uniaxial creep equations 2.6 for strain hardening will take the form of (Boyle and Spence [136]):

$$(\dot{\epsilon}^c_{ij})_{primary} = \frac{3}{2}\sigma'_{ij} C_1^{\frac{1}{C_2}} C_2 (\epsilon^c_e)^{\frac{C_2-1}{C_2}} {\sigma_e}^{(\frac{n_1}{C_2}-1)}, \tag{2.20a}$$

$$(\dot{\epsilon}^c_{ij})_{secondary} = \frac{3}{2}\sigma'_{ij} C {\sigma_e}^{n-1}, \tag{2.20b}$$

$$\dot{\epsilon}^c_{ij} = Max((\dot{\epsilon}^c_{ij})_{primary}, (\dot{\epsilon}^c_{ij})_{secondary}) \tag{2.20c}$$

$$\dot{\epsilon}^c_e = \sqrt{(\frac{1}{2}\dot{\epsilon}^c_{ij}\dot{\epsilon}^c_{ij})} \tag{2.20d}$$

where, i and j are the coordinate indices, $(\dot{\epsilon}^c_{ij})_{primary}$ are the primary creep rate components, $(\dot{\epsilon}^c_{ij})_{secondary}$ are the secondary creep rate components, $\dot{\epsilon}^c_{ij}$ are the effective creep strain rate components, σ'_{ij} are the stress deviator tensor components, ϵ^c_e is the equivalent creep strain and σ_e is the equivalent von Mises stress while C_1, C_2 and n_1 are primary creep constants and C and n are secondary creep constants.

The implementation of primary and secondary creep deformation in ABAQUS requires the use of a FORTRAN subroutine called 'CREEP' (Goyal et al [137] and Kim [138]). In this subroutine, the uniaxial model for primary and secondary creep equations have to be provided along with a criteria for determining the overall creep rate at each time step of analysis. Also, in many parts of the present work, ABAQUS user subroutine 'UVARM' was also used (Bray et al [139]). The subroutine 'UVARM' can be used to calculate different user defined quantities for a given time step. It is extensively used for creep damage calculations (Jiang et al [140]). In Chapter 3, a UVARM subroutine was used to define quantities related to stress and strain concentrations.

CHAPTER 3

FINITE ELEMENT MODELLING OF STRESS AND STRAIN DISTRIBUTIONS DUE TO MISMATCH IN CREEP RATES IN A THICK WELD

> *"Imagination is more important than knowledge."*
>
> Albert Einstein

Creep properties of metallic components are characterised by their minimum creep rates, creep strengths and creep ductilities. In a weldment, the base metal, weld and HAZ (Heat Affected Zone) may have different creep constitutive behaviours depending on the material and the type of weld. This can lead to constraint effects resulting in non-uniform distribution of stresses and strains which can further be enhanced by weld geometry and loading conditions. Non-uniform stresses and strains can lead to stress concentration and strain localisation effects as well as multiaxial states of stress. Therefore, in a weldment, mismatch in the creep deformation rates in the different sections of material may lead to reduction in creep life.

Design and assessment of residual life of in-service welded components operating at creep regime temperatures are addressed by design and assessment codes such as ASME BPVC Section III-NH [141], RCC-MR [34] and the R5 method [2]. An accurate estimate of creep damage should

ideally be based on a physically robust creep deformation model for the constituent materials of a component. However, such an assessment for weldments is complicated by their inherent metallurgical non-uniformity and the presence of residual stresses. ASME Code Case N-47-29 [44] and RCC-MR [34], therefore, follow a simplistic approach where creep strength of a weldment is expressed in terms of the creep strength of the parent material by the use of appropriate strength reduction factors in order to account for possible variations in the weld quality and uncertainties in stress computations (section 2.2.5). The reduction factors are defined as the ratio of creep rupture strengths of the weld and the parent material. However, as this approach is not based on a physically sound creep deformation model, it is generally over conservative and can be under conservative in certain circumstances (Tu and Sandstrom [42]). Also, the behaviour of the weldments under different loading conditions such as stress relaxation or under a combination of primary and secondary stresses cannot be fully understood using this approach. An analysis of the distribution of stresses and strains in weldments due to constituent creep mismatch can help in developing realistic weld strength reduction factors and hence lead to a better understanding of weld behaviour in creep under different loading conditions. Some of the earlier work (Samuelson et al [48], Chellapandi and Chetal [57]) have attempted to estimate stress concentration effects of material mismatch by calculating stress concentration factors for different scenarios of creep mismatch in simplified numerical models of weldments. In the present context, stress concentration factor is defined as the ratio of the peak stress arising due to creep mismatch to the nominal stress for a given state of stress. Nominal stress is the stress which would occur in a homogeneous material under the same loading conditions. Section 2.2.5 of chapter 2 details selected work on numerical analysis of stress concentration effects in a welded joint during creep deformation. Numerical analysis of stress concentration effects in a multi-material creep model is not straightforward as a stress singularity appears at the edge of any abrupt two material interface as shown in earlier work (Kitamura et al [79], Hyde and Sun [82]). Such a stress singularity is understood to be non-physical based on experience from crossweld creep tests. However, such a numerical singularity can overshadow the analysis of real physical constraint effects in the model arising out of material mismatch and geometry. A thorough discussion on earlier work done on stress singularity in abrupt material interfaces is provided in section 2.2.5 of chapter 2.

The aim of this chapter is to use finite element (FE) modelling for investigating the effects of

creep mismatch on stress and strain distributions in a weldment while discounting any artificial effects like stress singularity. It will also attempt to develop an approach of calculating design lives of weldments from the knowledge of relative creep deformation rates in the parent and weld metal and their respective creep rupture curves. The specific objectives of this chapter can be broken down as follows:

1. A review of stress singularity in a bi-material creep joint using a 2D plane strain FE model
2. Investigation of the effect of elastic perfectly plastic material properties of the parent and the weld metal on the stress singularity
3. Development of a computationally efficient weld model using singular elements around the stress singularity
4. Development of a method to calculate stress and strain redistribution effects in a bi-material creep model while ignoring any artificial peak stresses due to stress singularity
5. Define measures of stress and strain rate concentration effects in a weldment due to creep mismatch and conduct sensitivity analyses for different levels of mismatch, geometry of the weld and applied stress levels
6. Propose an approach of estimating stress concentration effects in a weldment for design against creep rupture

ABAQUS 6.14 [132] was used for the FE analyses.

3.1 Specification Finite Element Weld Models

For simplicity, only 2D finite element models of the weld were used in this work. Also, two distinct material zones were assumed to constitute a weld, namely, parent and weld metal and the existence of an abrupt weld interface separating the two.

The review work on stress singularity at a bi-material weld joint (section 3.2) used a 2D plane strain model which is an idealisation of a longitudinal weld in a large cylindrical vessel acted upon by hoop stress. For separating out the effects of material mismatch and geometry, an ideal straight weld-parent interface was used. Figure 3.1 shows a sketch of the idealised weld geometry

Elastic Constant	Value
Elastic Modulus, E (GPa)	150
Poisson's Ratio, ν	0.3

Table 3.1: Elastic constants used for the weld models

used. The aspect ratio (α) of the weld model is defined as the ratio of the weld thickness (t) to the plate width (W):

$$\alpha = \frac{t}{W}. \tag{3.1}$$

Only uniform monotonic tensile loading is considered as shown in Fig 3.1. Same elastic constants were assumed for both the parent and the weld metal as given in Table 3.1 which are similar to 316H elastic constants at at temperature of $550°C$. It was assumed that both the parent and the weld metal follows Norton's law of creep, where the creep strain rate is expressed as:

$$\dot{\epsilon} = A\sigma^n. \tag{3.2}$$

where $\dot{\epsilon}$ is the creep strain rate at a von Mises equivalent stress level of $\dot{\sigma}$ and A and n are Norton's constants, namely, stress coefficient and stress exponent respectively. Creep mismatch between the parent and the weld metal was introduced by taking different ratios of the weld stress coefficient (A_w) and the parent stress coefficient (A_p). The stress exponents for both the parent and the weld were assumed to be the same in all analyses for simplicity. It is believed that only the overall creep rate mismatch affects any stress singularity or stress concentration effects so a mismatch in creep coefficients should suffice.

Analysis of stress and strain concentrations due to creep mismatch in a weldment used the same model as in figure 3.1 but with plane stress assumptions. This was done in order to make the initial applied stress to be fully uniaxial. If a good understanding is developed for the uniaxial case, multiaxial loading states such as plane strain or a cylinder acted upon by internal pressure can be derived by using suitable stress triaxiality factors.

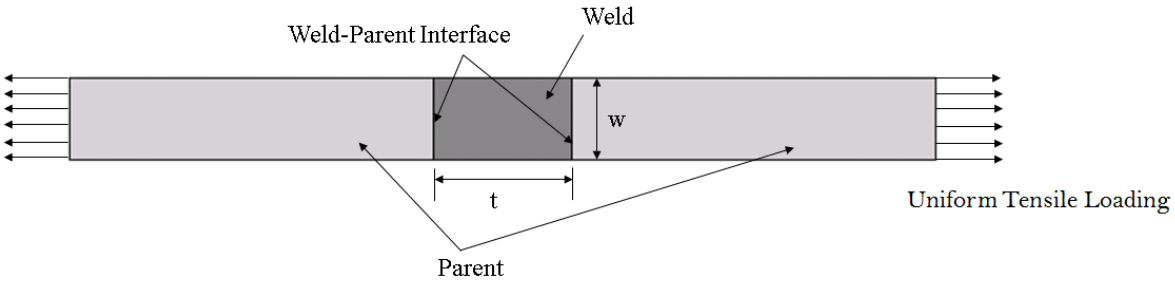

Figure 3.1: Weld model geometry, 't' is the weld thickness and 'w' is the plate width

3.2 Review of Stress Singularity at a Bi-material Creep Interface

An analytical weld model with two material regions and an abrupt interface, results in a stress singularity at the edge of the two material interface. Such stress singularities are a result of incompatibility of lateral strains and is commonly seen in any two elastic or elastic-plastic material interface. A considerable amount of work in the past has been done on stress singularities in two material bonded interfaces. Reedy [62], Bogy et al [64], Fr*ä*nkle et al [66], Niu et al [67], Qian et al [68], Ro et al [69], Desmorat et al [70], Dempsay and Sinclair [71] and Munz and Yang [74]), elastic-plastic material (Wang [75] and Rahman [78] have all studied the nature of stress singularity at the bonded interface of two elastic material. Kitamura et al [79] have studied stress singularity at an elastic-creep bi-material interface.

Hyde and Sun [82] investigated the nature of singularity at the interface of an axisymmetric cross-welded creep test specimen in order to throw light on the interpretation of crossweld creep test results. Effects of weld geometry (weld aspect ratio, type and shape of the weld etc.) and the mismatch in power law creep coefficients between the parent and the weld were studied. Hyde and Sun [82] also discussed on the area around the singularity point where the effect of the singularity will be significant. This was termed as the singularity zone and was defined in the paper as the maximum radius from the location of singularity where the equivalent stress is greater or equal to twice the nominal stress in the component. The choice of twice the equivalent stress was primarily influenced by the general range of stress concentration factors arising out of geometrical discontinuities. The intention was probably to show that for certain cases, it is possible that the singularity zone sizes will be in the order of microstructural features and hence

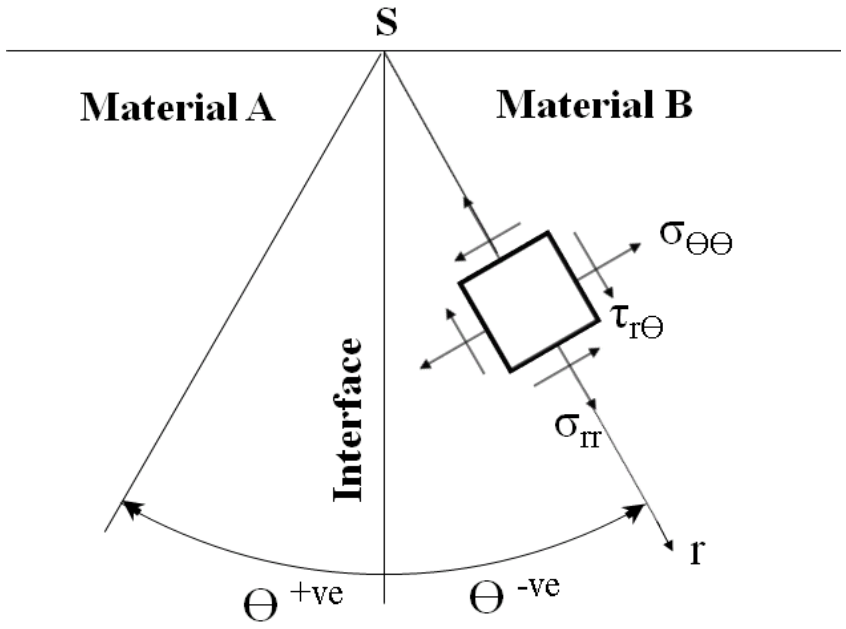

Figure 3.2: Schematic showing the location of stress singularity in a bi-material creep model

will not exist in a real component. However, this approach assumes that the order of stress concentration factors due to any material mismatch will always be '2' which can either be too over conservative or non-conservative. A multiplier of 2 on the applied stress is huge as the resulting creep life from a creep rupture calculation can reduce by orders of magnitude. The present work is directed towards finding meaningful stress concentration factors due to creep mismatch and hence such an assumption is not helpful in the context.

3.2.1 Stress Singularity in a Bi-material Elastic-Creep Finite Element Model

In the weld model described in the previous section, a stress singularity occurs at the free edge of the multi-material interface (point S) as shown in figure 3.2. At a singularity point, the stress components tend towards infinity with increasing creep. An '$r-\theta$' coordinate system centred about 'S' is defined in order to express the stress state at a point in the material in terms of the location of the point with respect to the singularity point 'S'. The in-plane stress components in the '$r-\theta$' coordinate system are the radial stress 'σ_{rr}', shear stress '$\sigma_{r\theta}$' and circumferential stress '$\sigma_{\theta\theta}$' stress as depicted in figure 3.2. The out of plane stress component is not considered here.

As shown in Hyde and Sun [82], if the stress components are plotted along radial lines emanating from the singularity point 'S', the stress components will follow a power law trend with reducing distance along the radial lines as represented by the following equation:

$$\sigma_{ij}{}^{m} = K(\theta)_{ij} r^{\lambda} \tag{3.3}$$

where $(i,j)/(r,\theta)$ are the planar coordinates centred at the interface edge, m(=Parent, Weld) is the material label, λ is the stress exponent (<0), $K(\theta)_{ij}$ is the stress intensity factor.

Also, it was shown in Hyde and Sun [82] that the variation of the stress components and the equivalent stress follow the same form. Hence, the above equation can be written in terms of the von Mises equivalent stress. It is useful to write the equation in terms of the von Mises equivalent stress because for creep stress exponents greater than one in the Norton's equation, equivalent stress is the driving factor for creep strain accumulation. Also, the equation is written below in non-dimensional form to augment parametric implementation:

$$\frac{\sigma_{eq}}{\sigma_{nom}} = K(\theta)\frac{r}{w}^{N_{eq}} \tag{3.4}$$

where, σ_{eq} is the von Mises equivalent stress at a given location near the singularity point, σ_{nom} is the nominal von Mises stress at a location far away from the weld interface, $K(\theta)$ is the stress intensity factor for the equivalent stress and N_{eq} is the stress exponent. The stress exponent in equation 3.4 determines the strength of the singularity and the problem is then to estimate the maximum possible value of N_{eq} for a range of material properties and geometry. For the same geometry of the weldment, the stress exponent of equation 3.4 will be a function of the ratio of the stress coefficients of the weld and the parent, and the stress exponent used in the Norton's law creep equation:

$$N_{eq} = f(\frac{A_w}{A_p}, n) \tag{3.5}$$

In this section, the singularity stress exponent N_{eq} was calculated for a range of values of $\frac{A_w}{A_p}$ and n for a plane strain 2D model. At first the equivalent stresses were plotted along different radial paths from 'S'. Figure 3.3 shows the variation of equivalent stress ratio with radial distance

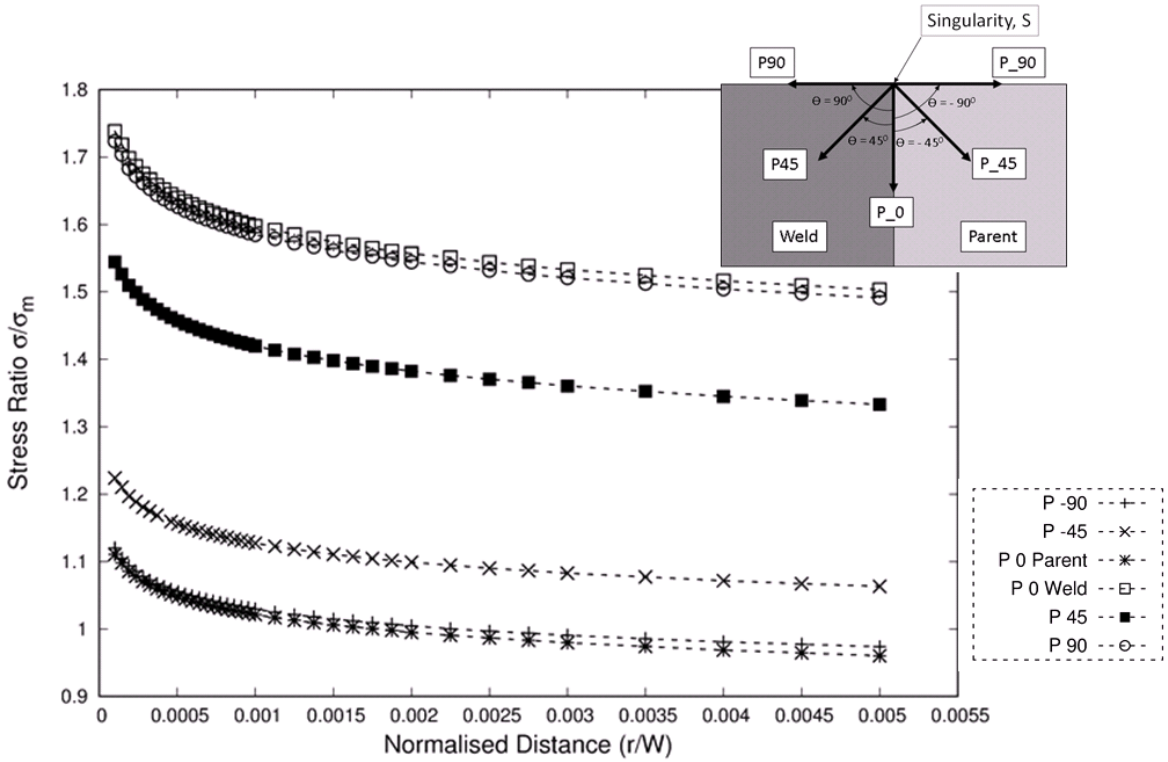

Figure 3.3: Variation of equivalent stress ratio with normalised distance from the singularity along the weld interface

r from S for the different orientation of the paths, for an $\frac{A_w}{A_p}$ ratio of 0.1 and an n value of 5. Power law fits were then made for the plots from where the stress exponent was determined. Since all the paths result in similar values of the stress exponent, only the P0 path (figure 3.3) was used in all subsequent calculations.

A creep strong weld is one where $\frac{A_w}{A_p}$ is less than one and a creep soft weld is one where it is greater than one. Following the same methodology, values of the singularity stress exponent N_{eq} were carried out for both creep strong as well as creep soft welds for a range of values of $\frac{A_w}{A_p}$ and n. For a creep strong weld, the range of values of $\frac{A_w}{A_p}$ was $[0.1, 0]$ while for a creep soft weld, the range was $[10.0, \infty]$. The values of n were 1, 2, 5, 8 and ∞. Figure 3.4 shows the plot of N_{eq} versus $1/n$ for a creep strong weld. Plots from Hyde and Sun [82] for an axisymmetric weldment is also presented alongside for reference. It can be seen that for a given $\frac{A_w}{A_p}$ ratio, the strength of the singularity N_{eq} reduces with increase in the creep stress exponent n. Also, the case with $\frac{A_w}{A_p} = 0$ can be taken as a bounding case for the creep rate mismatch in a creep strong weld. Figure 3.4 shows that the maximum possible value of the strength of the singularity is 0.4

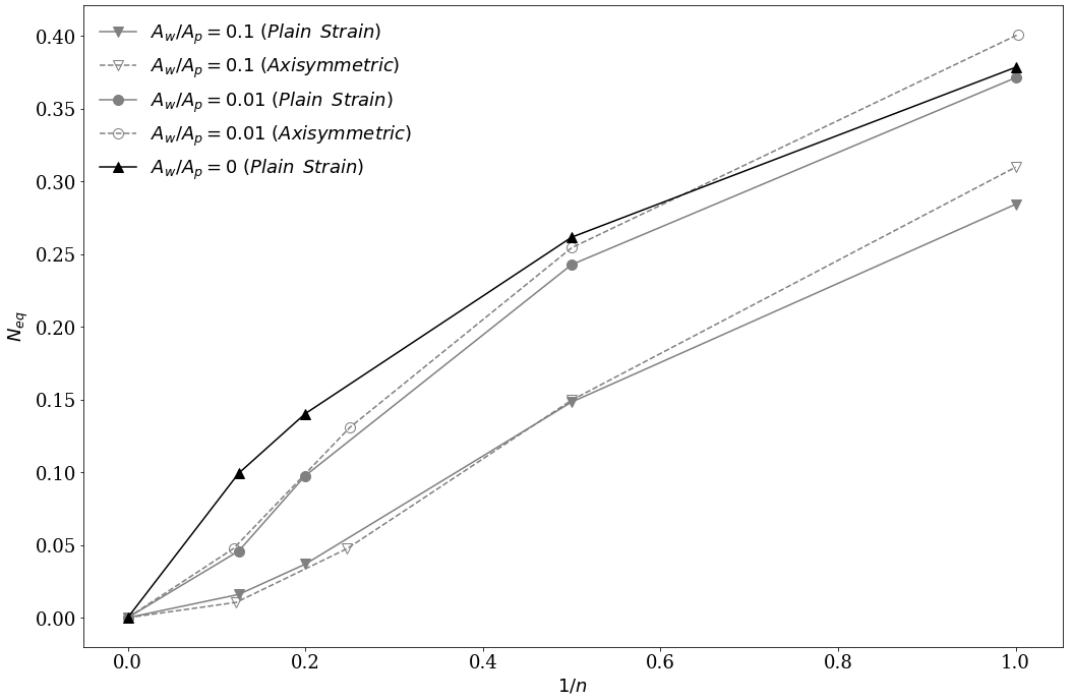

Figure 3.4: N_{eq} versus $1/n$ plots for a creep strong weld for a range of values of $\frac{A_w}{A_p}$

and that the strength of the singularity reduces to almost zero for $n = \infty$. The creep soft weld (figure 3.5) also shows similar trend with the exception that the strength of the singularity does not reduce to 0 as n approaches ∞.

It was discussed in Hyde and Sun [82] that the singularity is non-physical and therefore the local high stresses near the singularity will eliminate up to a distance of minimum grain size of the material. It is therefore important to get rid of the singularity in the modelling, so that the actual stress or strain raising effects of the constraints due to material mismatch across a weld interface can be studied.

3.2.2 Stress Singularity in a Bi-material Elastic-Plastic-Creep Finite Element Model

Elastic-plastic material properties were used for both the parent and the weld metal to investigate if using time independent plasticity helps in eliminating/ reducing the stress singularity at the edge of the weld-parent interface. A yield stress of 100MPa was used for both the weld and the parent. The aim was to use an elastic perfectly plastic material model but using a zero slope

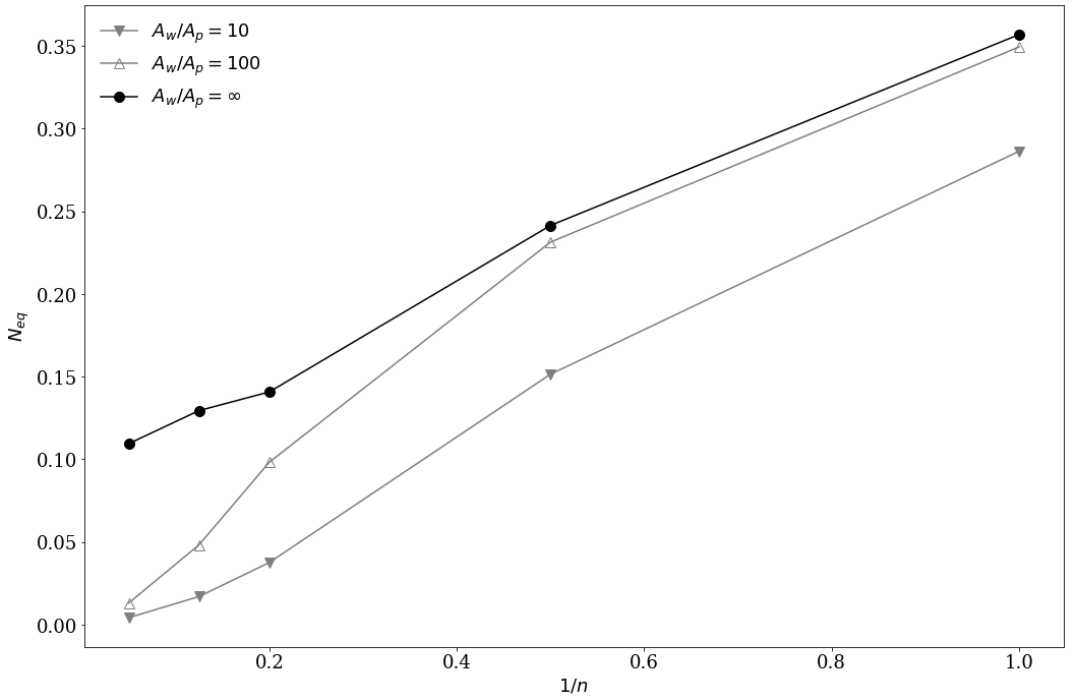

Figure 3.5: N_{eq} versus $1/n$ plots for a creep soft weld for a range of values of $\frac{A_w}{A_p}$

leads to convergence problems. Therefore a small plastic slope of 10MPa was used. Plasticity prevents stresses from becoming infinite and therefore eliminated singularity. It was expected that plastic straining at the creep strong material in this case would result in blunting of the stress singularity as it occurs in case of crack-tip plasticity. Only the creep strong weld cases were analysed.

Figure 3.6 shows the contour plot of equivalent plastic strains near the weld interface at 10000h. It can be seen that plastic strains occur only in the creep strong material, which is the weld in this case. Figure 3.7 shows the variation of normalised stresses along normalised distances from the singularity point for an elastic-plastic-creep weld model. It can be seen that the singularity is completely eliminated from the weld metal but the stress variation in the parent still remained singular. This is because the weld is stronger in creep with higher stresses resulting in significant plastic strain accumulation compared to the parent material.

Figure 3.8 shows the evolution of the variation of equivalent plastic strains in the weld along normalised radial distance from the singularity point with creep time. It can be seen that the plastic strains in the weld keep increasing with time with no sign of convergence. This can be explained in terms of the total inelastic strain incompatibility between the parent and the weld

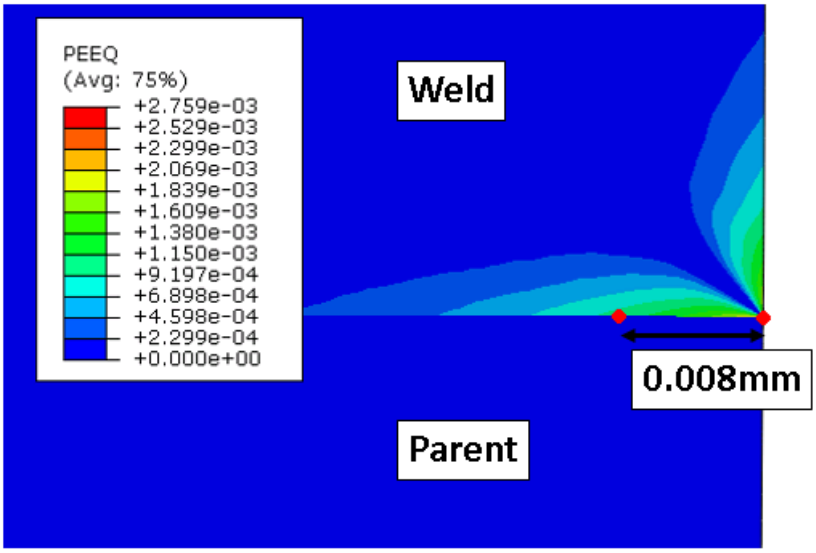

Figure 3.6: Contour plot of plastic strain near the singularity point

at the interface. Figure 3.9 shows the plot of differential equivalent plastic strain ($\delta\epsilon_p$) in the weld (creep strong) across the interface to the differential equivalent creep strain ($\delta\epsilon_c$) in the parent (creep strong) at different creep times. It seems from the plot that at any given time, the increase in creep strain in the parent with respect to the weld is manifested as an equivalent increase in plastic strain in the weld. In such a model, the plastic strains will keep on increasing with time in the creep strong material as the differential inelastic strains increase between the parent and the weld.

3.2.3 Use of Singular Elements Instead of a Fine Mesh at the Singularity

Isoparametric quadratic triangular elements with a displaced mid-side nodes were introduced at the free edge of the weld-parent interface in place of extremely fine meshes used in the earlier sections. Use of such element can greatly reduce the size of the model as extremely fine meshing is not required in the vicinity of the singularity. Figure 3.10 shows a schematic of the morphology and location of the singular elements at the weld interface.

Figure 3.11 provides a comparison of mesh sizes used in a conventional mesh and a model using singular elements. It can be seen that computational efforts can be greatly reduced if singular elements are used. Figure 3.12 shows comparison of stress variation in the creep strong material along the weld-parent interface for a conventional mesh and a mesh with singular

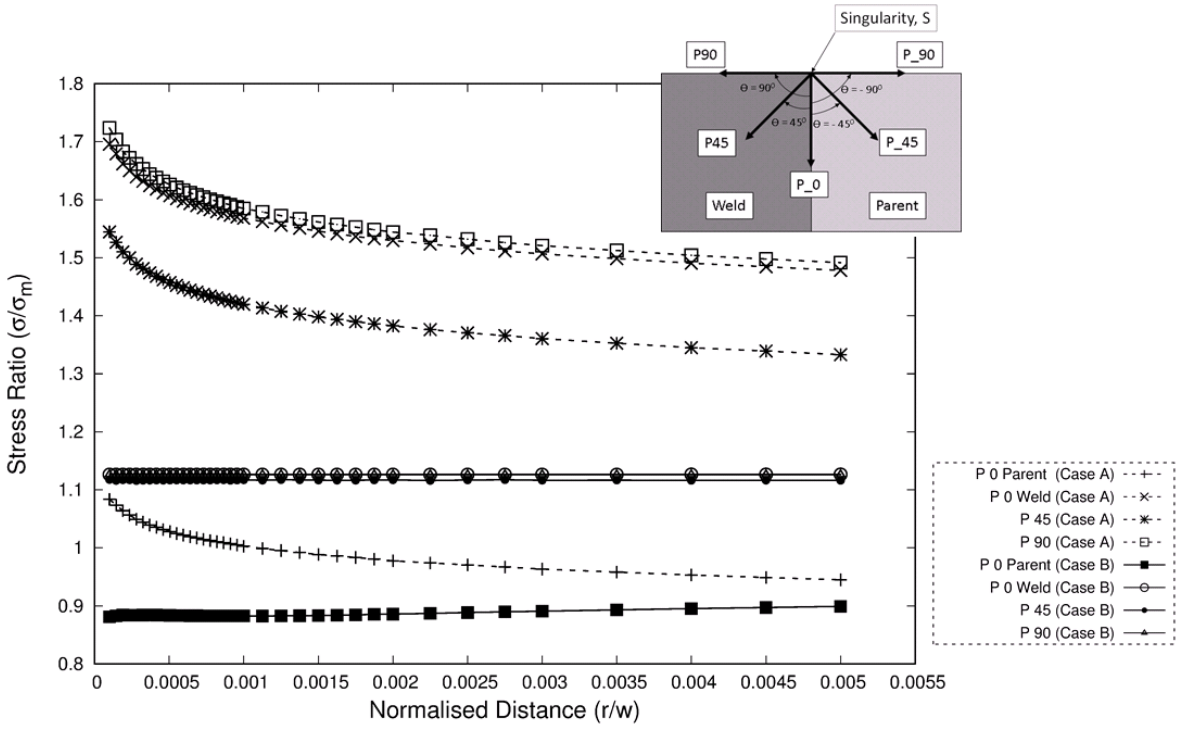

Figure 3.7: Variation of normalised equivalent stress with normalised distance from the singularity along the weld interface

elements.

It can be seen that use of singular elements in modelling weld-parent interfaces greatly reduces computational effort without the loss of accuracy.

3.3 Stress Concentrations due to Creep Mismatch

In this section a bi-material 2D plane stress model of a weld will be used to study the effects of creep mismatch on stress and strain redistributions. The effects of weld geometry, level of mismatch and stress levels will also be explored. In the end, a new approach will be proposed for calculating creep rupture lives of welded joints.

The different values of creep mismatch, weld aspect ratio and applied stress are summarised in table 3.2. The FE mesh shown in figure 3.11 was used for all the FE analyses described in this section. Also, the same loading type was used as described in the previous section.

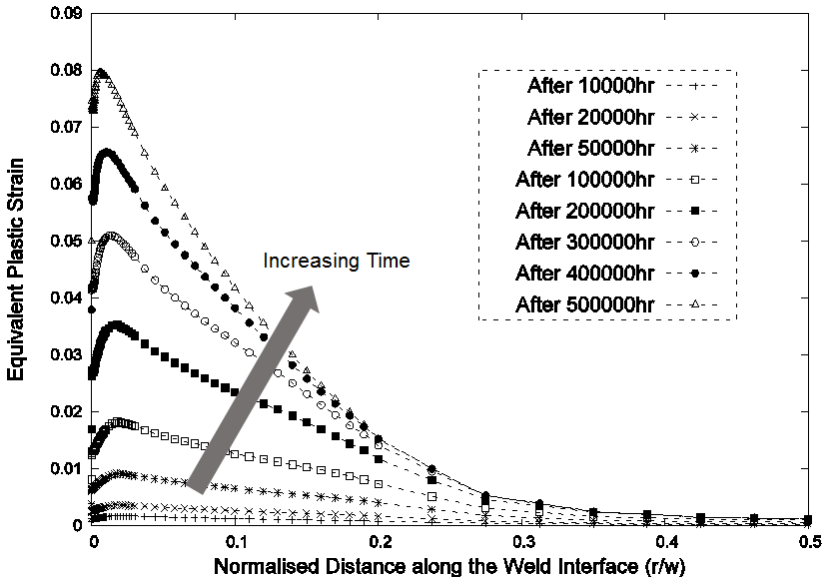

Figure 3.8: Evolution of equivalent plastic strains along the interface in the weld metal

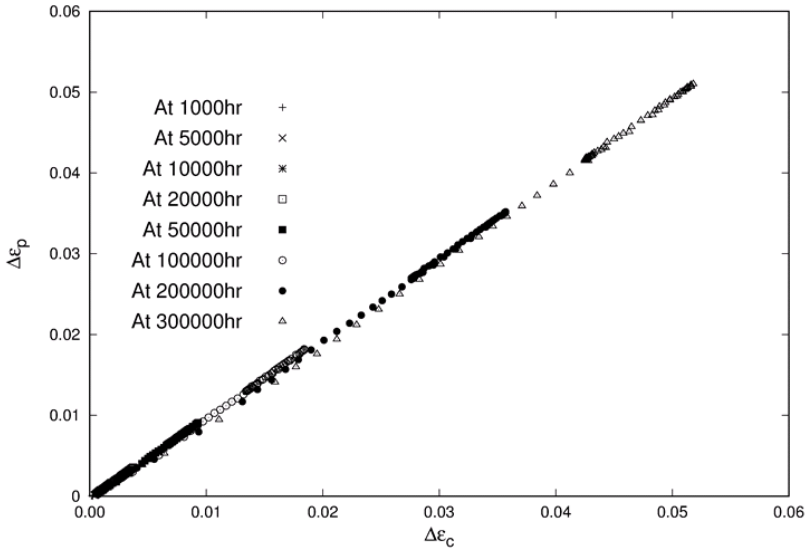

Figure 3.9: Plot of differential equivalent plastic strains in the weld metal to that of equivalent creep strains in the parent material for different creep times

3.3.1 Interpretation of Results

Lateral strain mismatch leads to a non-uniform stress distribution across the weld interface of the models described in the earlier sections and schematically depicted in figure 3.13. The stress distribution is symmetrical about the model centreline due to the geometry and the loading

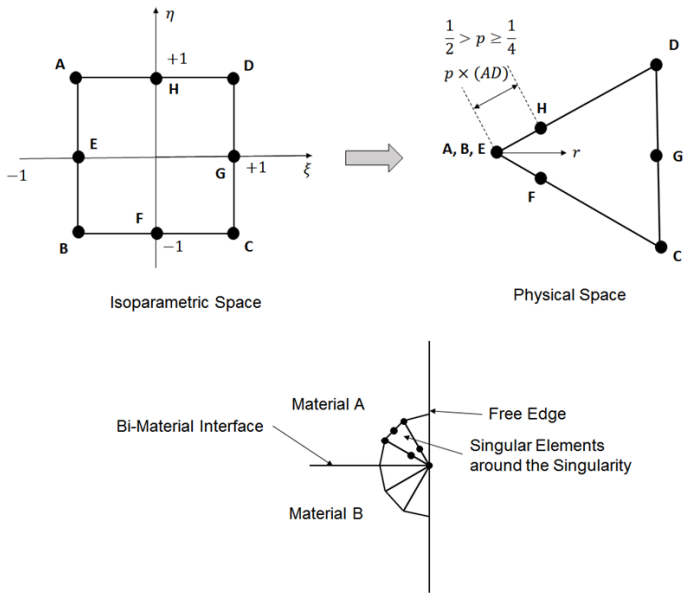

Figure 3.10: Schematic showing the structure and location of the singular elements

Parameter	Description	Values
$\frac{A_w}{A_p}$	Ratio of Norton's creep coefficients for weld and parent	0.1, 0.01
α	Weld aspect ratio	0.25, 0.3, 0.4, 0.5, 1.0
$\sigma_{applied}$ (MPa)	Uniaxial applied stress	100, 200, 300

Table 3.2: Table of material and geometry constants for the FE models

conditions used. This non-uniform stress distribution is a result of local bending at the interface resulting from a lateral strain mismatch between the creep strong and the creep weak material. This is explained schematically in figure 3.14. Since the lateral strains at the creep strong material is smaller than the creep weak material, the action of the creep weak material on the creep strong material creates shear forces and bending moments on the creep strong material at the interface shown by the blue arrows. Similarly, a set of shear forces and bending moments act on the creep weak material at the interface. As pointed out in Hyde and Sun [82], singularity is a modelling artefact and such high peak stresses at the edge of the interface should be consumed by inter granular displacements. Therefore, it can be argued that stress distributions in a weldment is only dependent on the global bending due to creep mismatch. It is essential to then discount the effect of stress singularity in order to meaningfully calculate stress and strain concentration effects in a weldment. This section describes a method of defining a singularity zone around the point of stress singularity which can be masked out for analysing stress distributions in an

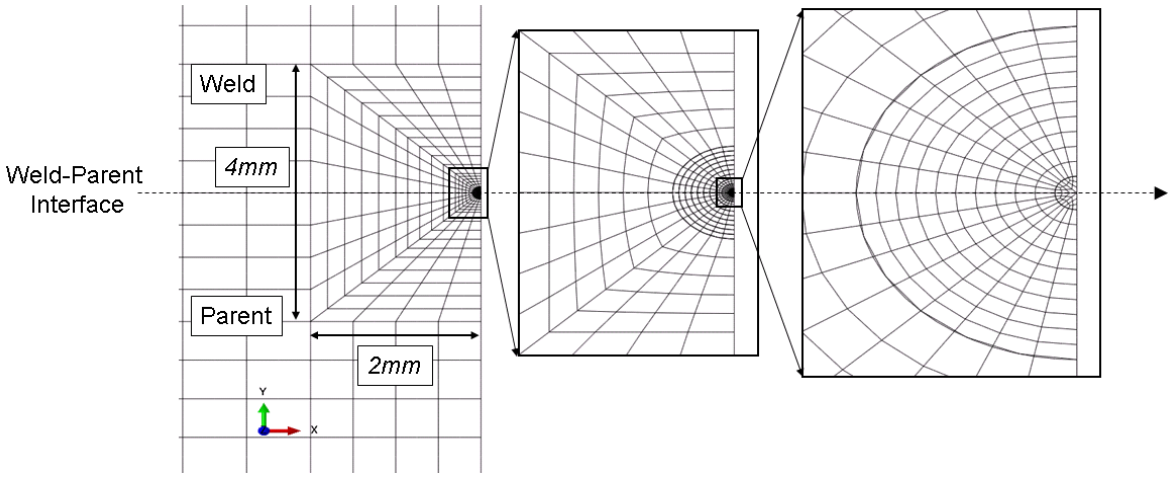

(a) Plot of mesh with normal quadratic elements

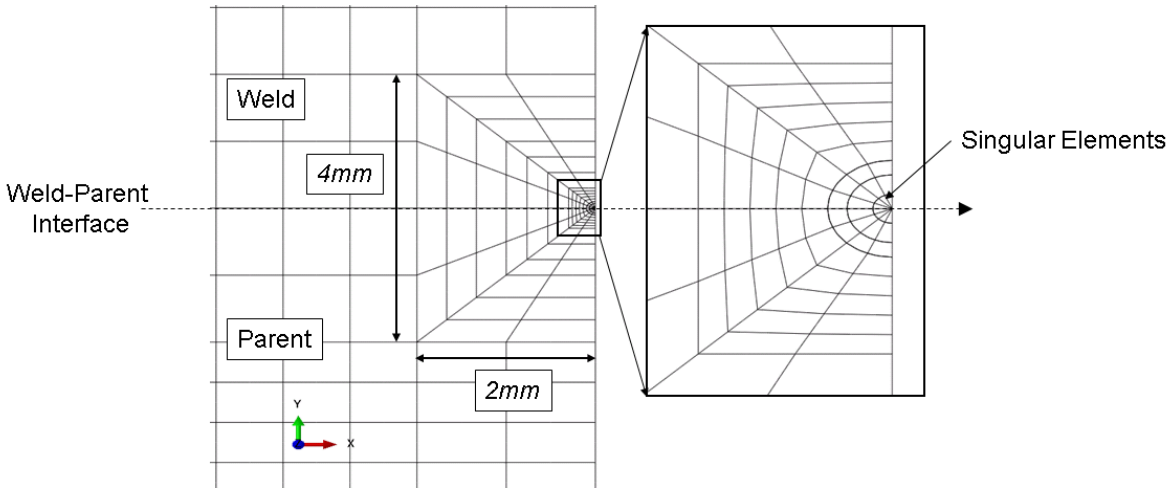

(b) Plot of mesh with singular quadratic elements in the vicinity of the singularity

Figure 3.11: Comparison of mesh with normal quadratic elements and mesh with singular quadratic elements in the vicinity of the singularity

ideal weldment. In order to account for the global bending only and discount the peak stresses at the edges of the weld interface, stresses were linearised across the weld interface and then shown that while the peak stresses were dependent on mesh refinement, the linearised stresses remained unaltered.

Linearised stresses across half width of the weld interface are plotted along with the actual von Mises stresses for two different mesh sizes (figure 3.15). It can be seen that the linearised stresses are independent of mesh size. The maximum linearised stresses were then projected back on the von Mises stress curve (figure 3.16) in order to determine a distance around the point

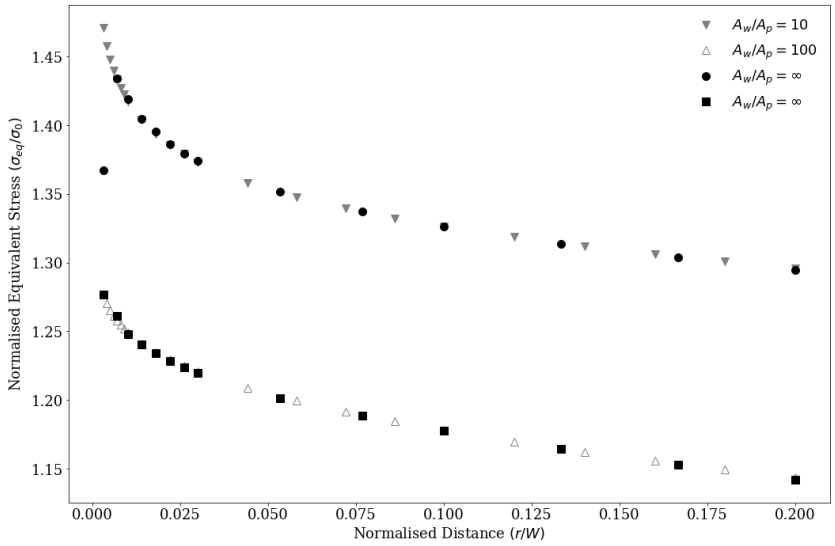

Figure 3.12: Plot of normalised equivalent stresses versus normalised distance along the weld interface for conventional and singular elements

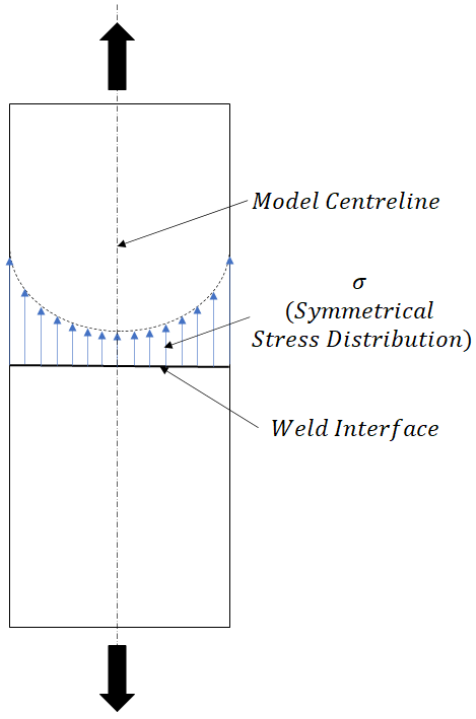

Figure 3.13: Schematic showing non-uniform and symmetrical axial stress distribution at the weld interface in the model

of singularity where the artificial peak stresses due to stress singularity are significant. This distance around the point of singularity is defined as the singularity zone $'r'_s$ and the stresses

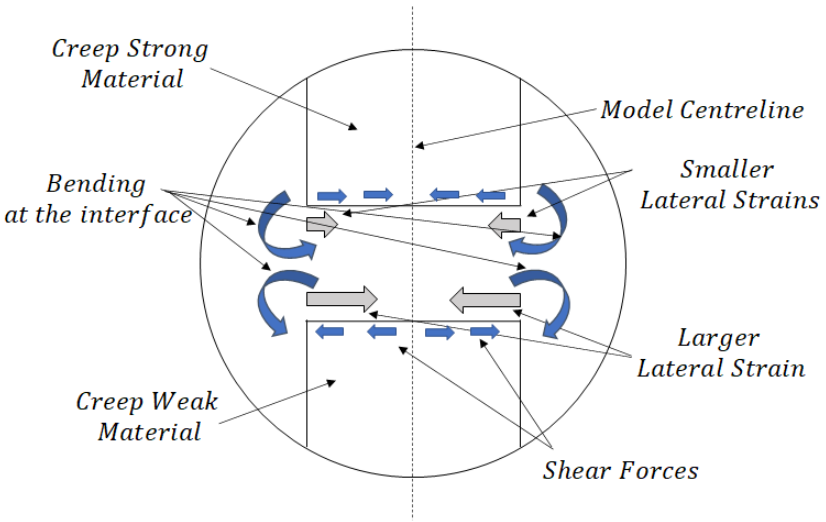

Figure 3.14: A schematic of the decomposed weld interface of the model explaining the origin of bending as a result of lateral strain mismatch

and strains in this zone will be ignored for calculating stress and strain concentrations.

FE analyses revealed that the singularity zone extends to around 0.04 times the width of the weldment $'W'$ irrespective of the weld geometry, level of creep mismatch and stress levels. This is illustrated in figure 3.17.

In all the FE analyses described in the following sections, stresses and strains in the singularity zone were neglected for interpretation of stress and strain distributions in the models.

3.3.2 Results and Discussion

The model described in section, was run with for an applied uniform axial stress of 100MPa for $\frac{A_w}{A_p} = 0.1$. Figures 3.18 and 3.19 present the von Mises stress and equivalent creep strain distributions in the model after the stationary state was achieved (20,00,000 hours). The singularity zone has been masked out in the plots. It can be seen that a creep mismatch results in a global redistribution of stresses. As the weld is creep hard, the highest stresses appear in the weld whereas the peak creep strains in the parent.

In the present context, a stress concentration factor (SCF) at a point is defined as the ratio stress at that point to the nominal stress. In this case, the nominal stress is taken as the uniform uniaxial stress acting far away from the weld interface. Two different measures of the stress concentration factor are used here, one for the maximum principal stress and one for the von

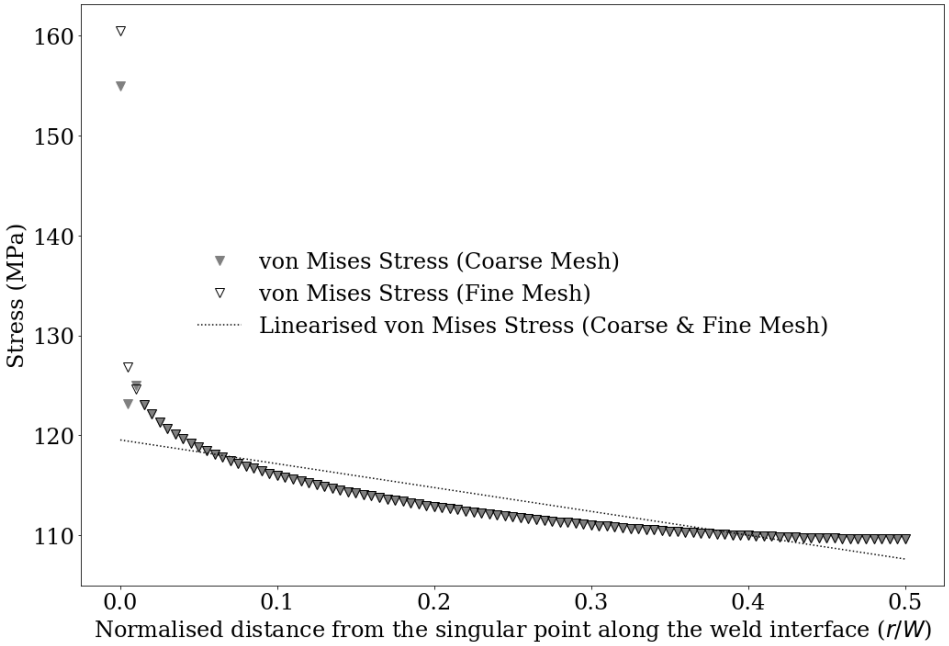

Figure 3.15: Plot of von Mises stresses along with linearised stresses along normalised distance from the singular point along the weld interface

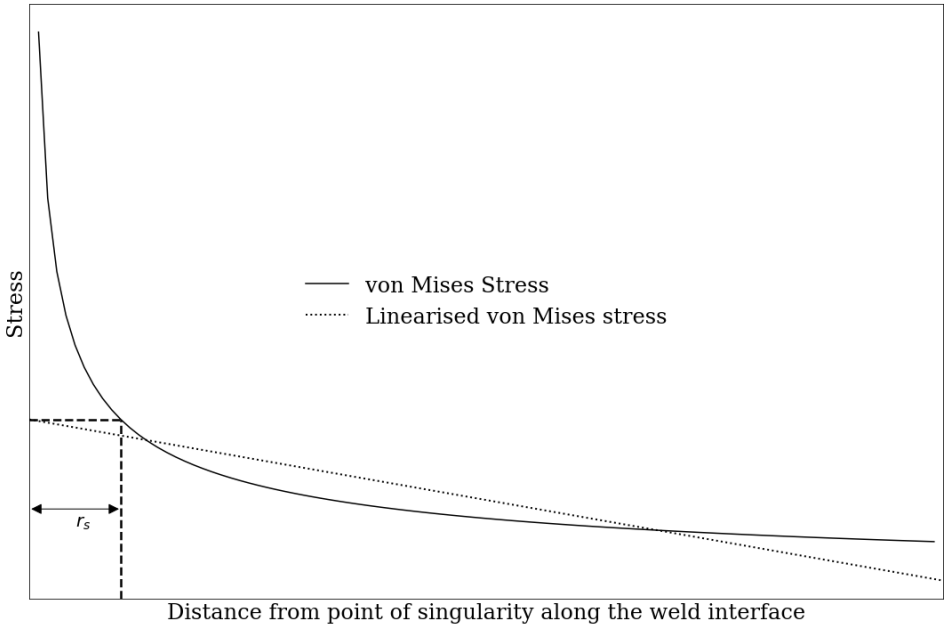

Figure 3.16: Plot of von Mises stresses along with linearised stresses along normalised distance from the singular point along the weld interface

Mises equivalent stress as defined below:

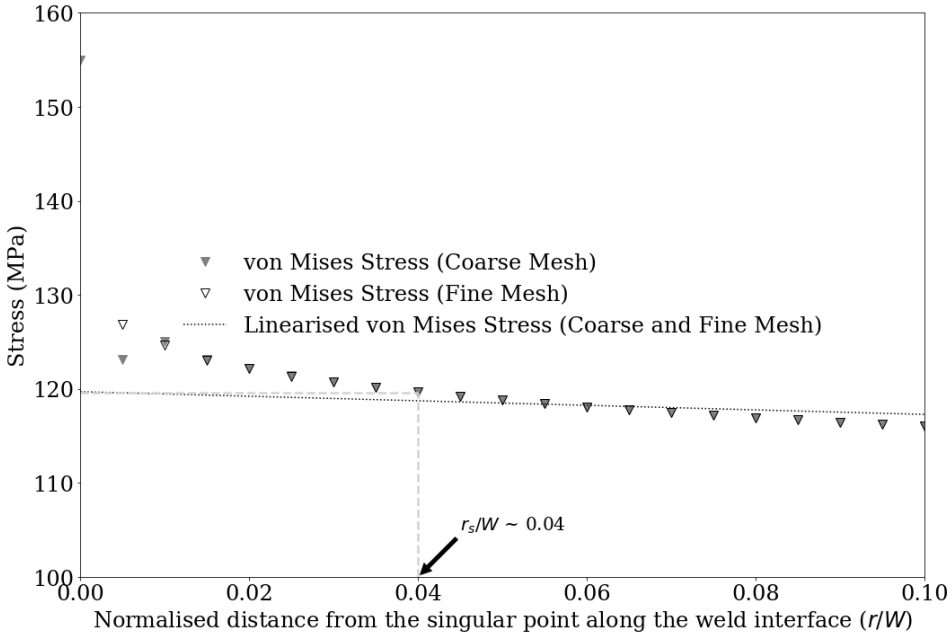

Figure 3.17: Plot of linearised and von Mises stresses along normalised distance from the singular point in order to show where on the von Mises stress plot the maximum magnitude of linearised stress occur

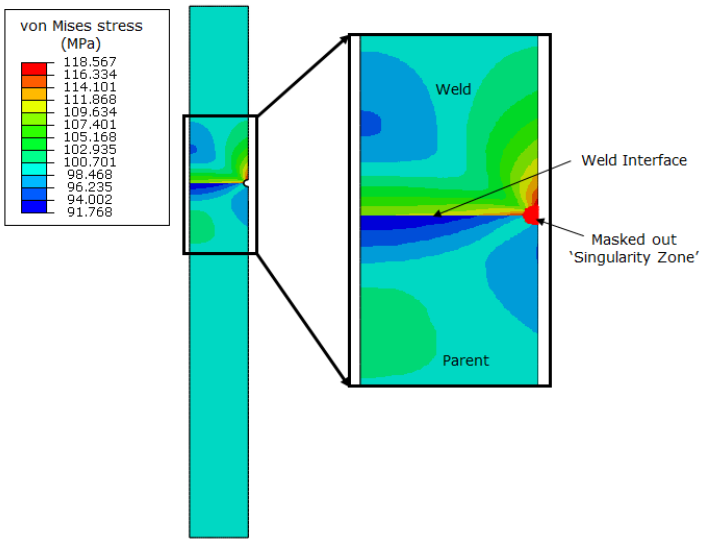

Figure 3.18: Contour plot of von Mises equivalent stresses in the weldment for $\frac{A_w}{A_p} = 0.1$

(3.6a)
$$K_{\sigma_{eq}} = \frac{(\sigma_{eq})_{max}}{\sigma_{nom}},$$

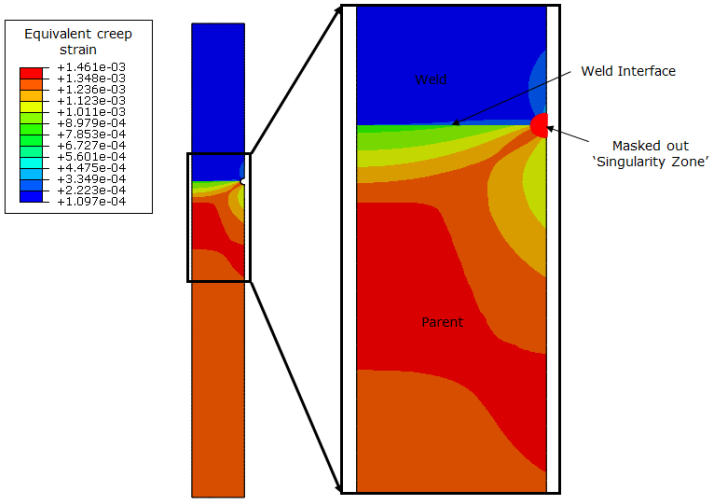

Figure 3.19: Contour plot of equivalent creep strains in the weldment for $\frac{A_w}{A_p} = 0.1$

(3.6b)
$$K_{\sigma_1} = \frac{(\sigma_1)_{max}}{\sigma_{nom}}$$

where, $K_{\sigma_{eq}}$ and K_{σ_1} are the stress concentration factors for the von Mises equivalent stress and the maximum principal stress respectively, σ_{eq} and σ_1 are von Mises equivalent stress and maximum principal stress and σ_{nom} is the nominal stress. The reason for using two different measures of SCFs is to capture the result of any stress triaxility arising out of creep mismatch which would make the two values different.

As creep strains are a function of time, it is more prudent to use creep strain rates instead of creep strains in order to measure enhancement of creep strains due to creep mismatch. Therefore, a strain rate enhancement factor (SREF) is defined as the ratio of the maximum creep strain rates in the model to the nominal creep strain rate. Nominal creep strain rate is defined as the secondary creep strain rate in the respective material corresponding to the nominal stress.

(3.7)
$$SREF = \frac{(\dot{\epsilon}_c)_{max}}{\dot{\epsilon}_{nom}},$$

where, $(\dot{\epsilon}_c)_max$ is the maximum equivalent creep strain rate and $\dot{\epsilon}_{nom}$ is the nominal creep strain rate.

Although, the focus of the present work is restricted to creep deformation with creep damage kept out, since the purpose of any creep deformation modelling exercise is ultimately to support

creep damage predictions, the strain rate enhancement factor defined above will be slightly modified to take into account the multiaxial stress state in the material. However, a detailed discussion on creep damage is avoided. For 316H steels, creep damage accumulation at a material point is a function of the creep strain rate, stress multiaxiality and creep ductility of the material (Holmstrom et al [142]). As creep mismatch results in a re-distribution of stresses in a weldment, it can be expected that the stress state will be multiaxial. Therefore, in order to account for the stress triaxiality as well, an equivalent SREF is defined as the ratio of SREF and a suitable stress triaxiality factor. The Spindler fraction (SF) (Spindler et al [143]) is the most commonly used triaxiality factor for 316H steels and hence in this case, the Spindler fraction was used for measuring stress multiaxiality.

The Spindler fraction is defined as:

$$SF = e^{(p(1-\frac{\sigma_1}{\sigma_{eq}})+q(1-\frac{\sigma_h}{\sigma_{eq}}))} \tag{3.8}$$

where σ_h is the hydrostatic stress and p and q are two constants. For 316H steels, p = 2.38 and q = 1.04.

Therefore an equivalent strain rate enhancement factor (ESREF) is given by:

$$ESREF = \frac{SREF}{SF} \tag{3.9}$$

Figure 3.20 shows contour plots of the SCFs calculated in the model, both for the von Mises equivalent as well as maximum principal stresses for $\frac{A_w}{A_p} = 0.1$. It can be seen that the maximum values occur in the weld, which is the creep strong material. The SCFs calculated for the von Mises stress and the maximum principal stress are equal indicating that there is insignificant stress triaxiality in the creep strong material due to creep mismatch.

Figure 3.21 shows contour plots of Spindler fraction in the model. A value of 1 indicates uniaxial stress state and the lower the value, the higher is the stress triaxiality. It can be seen that Only the parent (creep weak) sees a high level of stress triaxiality arising out of material mismatch.

As has been noted earlier, since the maximum stresses occur at the creep strong material and the maximum creep strains in the creep weak material, in case of $\frac{A_w}{A_p} < 1$, the SCFs were calculated for the weld and equivalent SREF for the parent and vice versa.

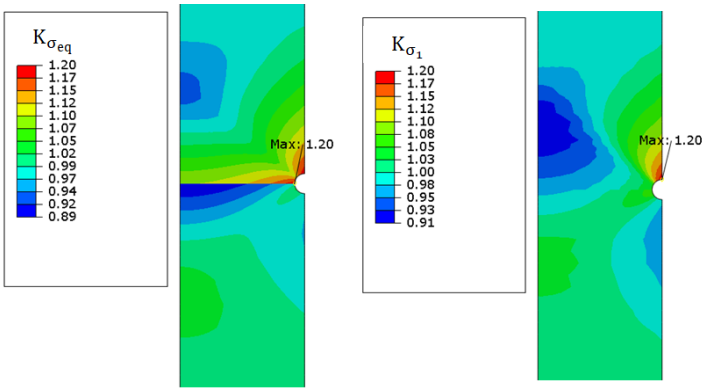

Figure 3.20: Contour plot of SCFs for von Mises and maximum principal stresses in the weldment for $\frac{A_w}{A_p} = 0.1$

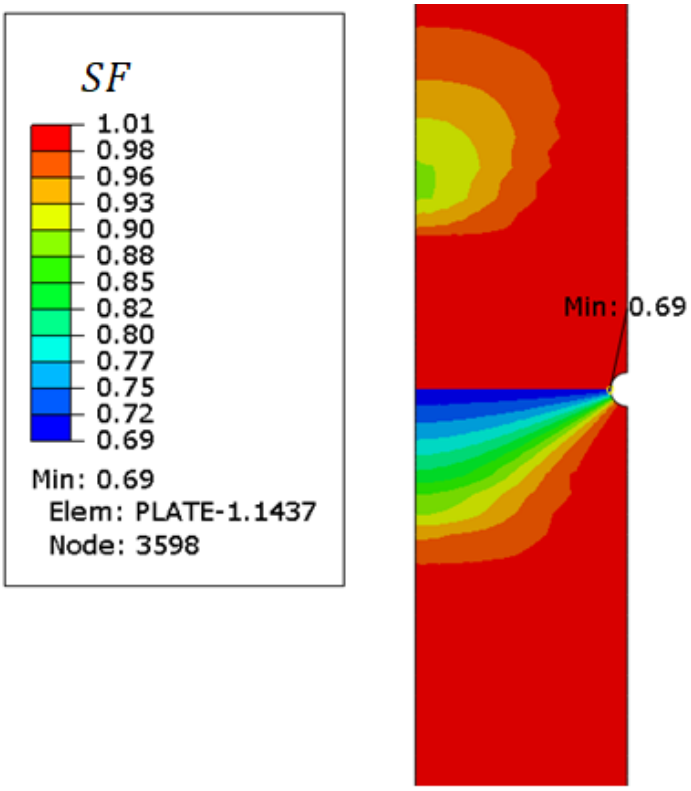

Figure 3.21: Contour plot of Spindler fraction in the weldment for $\frac{A_w}{A_p} = 0.1$. A value close to 1 denotes a perfectly uniaxial stress state.

3.3.2.1 Effect of creep rate mismatch

Figure 3.22 shows the evolution of the peak SCFs in the creep strong material for a range of $\frac{A_w}{A_p}$ ratios against nominal creep strains in the respective creep weak material. The peak SCFs were

taken from those integration points in the model which were leading in the evolution of SCFs. Such integration points will be called as 'leading integration points' henceforth. The reason for using nominal creep strains instead of time for the abscissa is for better representation of plots for different levels of creep mismatch in the same figure. It can be seen that the SCFs increase first, reach a peak and then decrease to a stationary value. The plot reveals that the SCFs are independent of whether the weld is creep strong or creep weak. However, the SCFs are strongly dependent on the level of mismatch, for $\frac{A_w}{A_p} = 0.1 or 10$, the SCFs lie below a value of 1.2 whereas for $\frac{A_w}{A_p} = 0.01 or 100$, the SCFs reach a maximum value of 1.4.

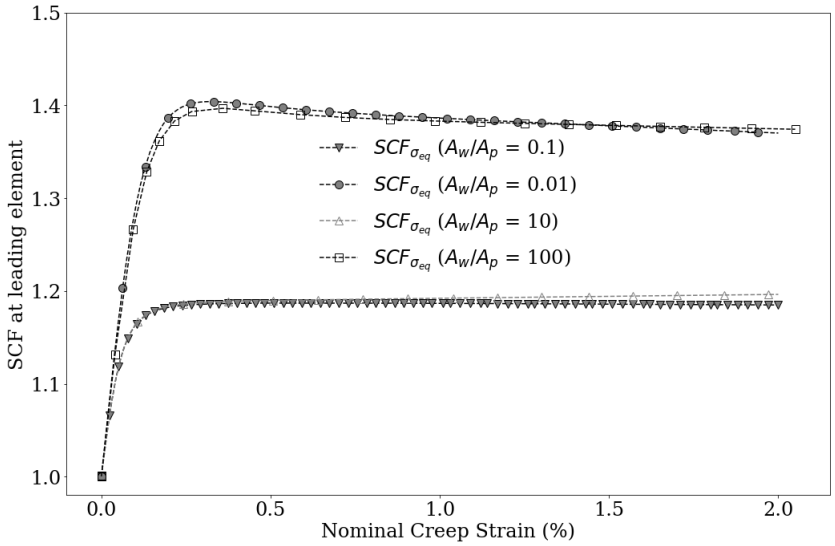

Figure 3.22: Plot of SCFs for von Mises and maximum principal stresses against nominal equivalent creep strains in the parent for $\frac{A_w}{A_p} = 10$

Figure 3.23 shows the evolution of the peak equivalent SREFs in the creep weak material for a range of $\frac{A_w}{A_p}$ ratios against nominal creep strains in the respective creep weak material. All equivalent SREFs were taken from the leading integration points in the models. The equivalent SREFs depend primarily on the level of mismatch, an approximate value of 1.31 for $\frac{A_w}{A_p} = 0.1 or 10$ and a value close to 2.5 for $\frac{A_w}{A_p} = 0.01 or 100$.

A high degree of creep rate mismatch (greater or equal to $\frac{A_w}{A_p} = 0.01 or 100$) between the weld and the parent would mean that the failure will predominantly be in the weaker material unless the creep strong material has an abnormally low level of ductility. The creep life of the weldment will therefore be only dependent on the creep rupture properties of the creep weak material. Therefore, it can be stated that a mismatch level of $\frac{A_w}{A_p} = 0.1 or 10$ should serve as the upper bound

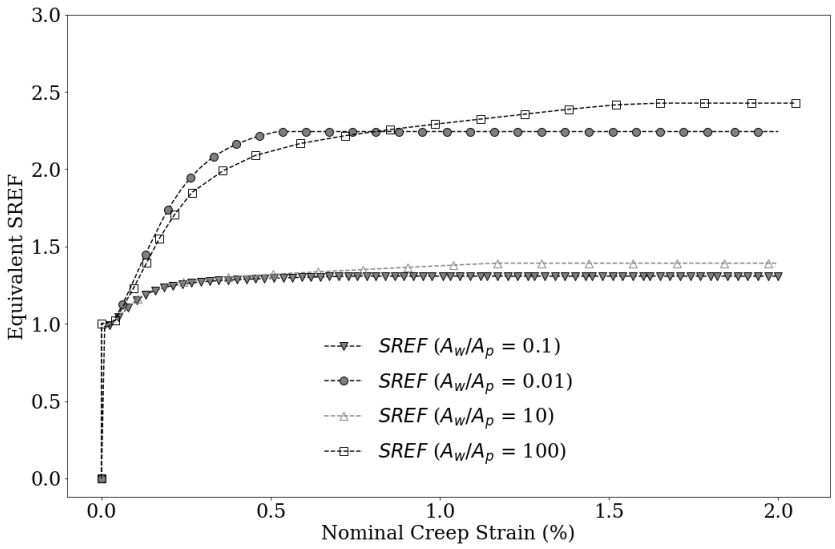

Figure 3.23: Plot of equivalent SREFs in the creep soft parent against nominal equivalent creep strains in the parent for $\frac{A_w}{A_p} = 10$

case for calculation of SCFs and equivalent SREFs. Hence, all the subsequent analyses will use a $\frac{A_w}{A_p}$ value of 0.1 or 10.

3.3.2.2 Effect of applied stress

Figure 3.24 shows the variation of SCF and equivalent SREF with magnitude of applied stress for $\frac{A_w}{A_p} = 0.1$. It can be seen that the SCF remains constant and independent of the applied stress. However, the peak equivalent SREF increases with the applied stress. Chellapandi and Chetal [57] showed that the SCFs increase with applied stress, which is found to be untrue in this case.

3.3.2.3 Effect of weld aspect ratio

Figure 3.25 shows the variation of SCF and equivalent SREF with the weld aspect ratio for $\frac{A_w}{A_p} = 0.1$ and an applied stress of 100MPa. It can be seen that both the peak SCFs and the peak equivalent SREFs are independent of the weld aspect ratio.

3.3.2.4 Discussion

It can be observed from the above results that the peak SCF has a bounding value of 1.19 for all practical levels of creep rate mismatch in a similar metal weldment. Also, since in practical situations, the level of primary stress in a component remains much lower than 100MPa, the

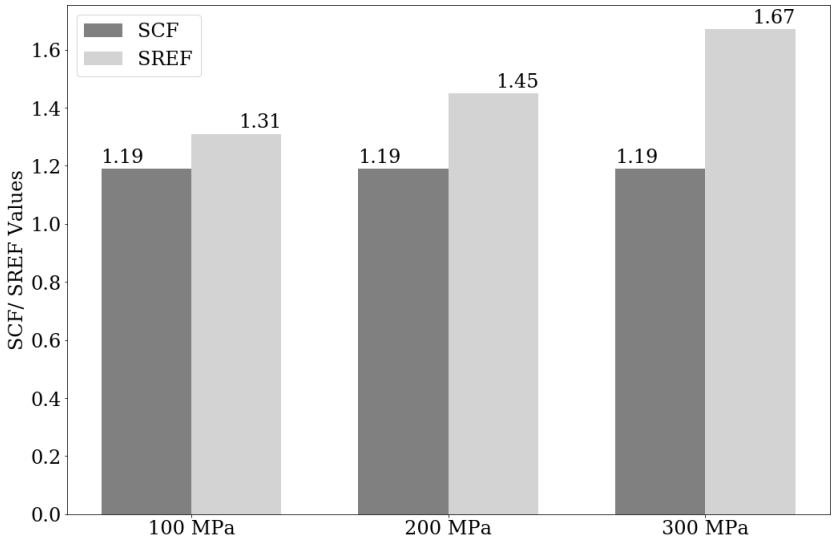

Figure 3.24: Variation of SCF in the creep hard weld and equivalent SREF in the creep soft parent against applied stress

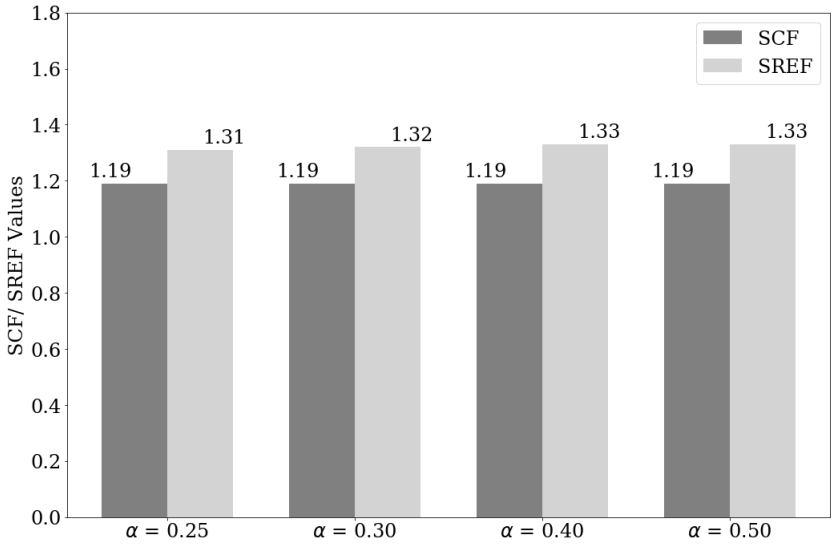

Figure 3.25: Variation of SCF in teh creep hard weld and equivalent SREF in the creep soft parent against applied stress

peak equivalent SREFs have a bounding value of 1.31. While it is true that the creep strong material sees a higher level of equivalent stress due to the stress concentration effects, failure can also occur in the creep weak material depending on the magnitude of enhanced creep strain rates due to mismatch and it's multiaxial creep ductility.

This work did not consider the effects of elastic modulus, multi-axial loading and elastic-

plastic mismatch between the weld metal and the parent. An elastic modulus value of 150MPa was used in all the analyses as at typical plant temperatures of $550°C$, 316H steels have a mean elastic modulus of 150MPa (RCC-MR [34]). It can be assumed that SCFs will decrease with decrease in elastic modulus as that will lead to a greater relaxation of stresses. Therefore any temperature higher than $550°C$ will result in a lower value of maximum SCF. Although, multi-axial loading has not been considered here, the results show that the multiaxiality arising out of material mismatch does not change the maximum SCF (as the maximum SCF for the principal stress and von Mises remained the same). A modified equivalent SREF for multi-axial loading can be obtained by dividing the equivalent multi-axial loading from the plane stress case by a suitable triaxiality factor corresponding to the loading. Since Norton's law was used for creep deformation which does not include the effect of any existing plastic strains, it can be said that any mismatch in elastic-plastic properties should not significantly affect the stress and strain re-distributions due to creep mismatch.

Conventional codes for creep design of weldments (ASME BPVC Section VIII Div 1, ANSI B31.1) use strength reduction factors applied to parent material creep strengths in order to calculate rupture lives of the weldments. These reduction factors are obtained either by comparing weld metal creep strengths to the parent material. This approach lacks any consideration of any metallurgical notch effect created by a mismatch of creep properties between the weld metal, HAZ and the parent material.

In nuclear pressure vessel codes such as ASME Code Case-47, the R5 method and RCC-MR, a more detailed approach is followed which involves consideration of both stress based as well as strain based failure of the weldment. In these codes, creep damage due to primary stresses are calculated using the creep rupture curves for either the parent material or both the parent and the weld metal. Creep damage due to the relaxation of secondary stresses are then calculated using a ductility based approach where conservatism is introduced by using appropriate weld strength reduction factors as well as limits on the allowable creep strains. The overall damage is then obtained as a sum of the two creep damage terms as well as any fatigue damage forcyclic loading. The total damage is then used to calculate the life of the weldment. This involves significant elastic/ inelastic analyses. However, only parent material properties are used for those analyses.

In ASME Code Case-47, strength reduction factors are used for calculation of creep rupture

lives of weldments, which are obtained from crossweld creep rupture tests. This approach is better than the conventional codes as it implicitly considers any existing notch effect due to creep mismatch. However, this approach suffers the drawback of obtaining rupture data for each specific combination of constituent materials. This is because no clear correlation is established between the level of creep mismatch and the corresponding reduction in life. In the R5 method (Volume 2/3 [2]), two different approaches are used for similar and dissimilar metal welds. For similar metal welds, no reduction factor is used for creep rupture calculations. However, for some specific materials, separate creep curves are used for the weld metal and the parent to obtain minimum creep life. For dissimilar metal welds (R5 Volume 6 [2]), for some combination of weldments, such as a $2\frac{1}{4}CrlMo:316$ joints, a stress concentration factor of 1.25 is used on the rupture stress. This was obtained by performing crossweld rupture tests.

None of the above methods explicitly account for any metallurgical notch effect due to a creep mismatch in a weldment. This work addresses the issue and attempts to develop an alternate route of calculating creep rupture lives of weldments by taking into consideration any stress re-distribution in a weldment owing to creep mismatch. A simple method for determining creep rupture lives for 316H welds is described here, which takes into account both the stress and strain rate increase in the weldment and also the multi-axial state of stress. The method consists of the following steps:

1. Peak SCFs and SREFs are calculated for the assumed level of creep mismatch and applied stress in the weldment
2. The rupture stress for the creep strong material is calculated as a product of the SCF and the nominal equivalent stress
3. The rupture life of the creep strong material is calculated using the creep rupture stress calculated in the previous step
4. The rupture life of the creep weak material is calculated using the nominal equivalent stress divided by the SREF
5. The minimum of the lives calculated for the creep strong and creep weak material gives the life of the weldment

Figure 3.26 shows a flowchart of the above steps.

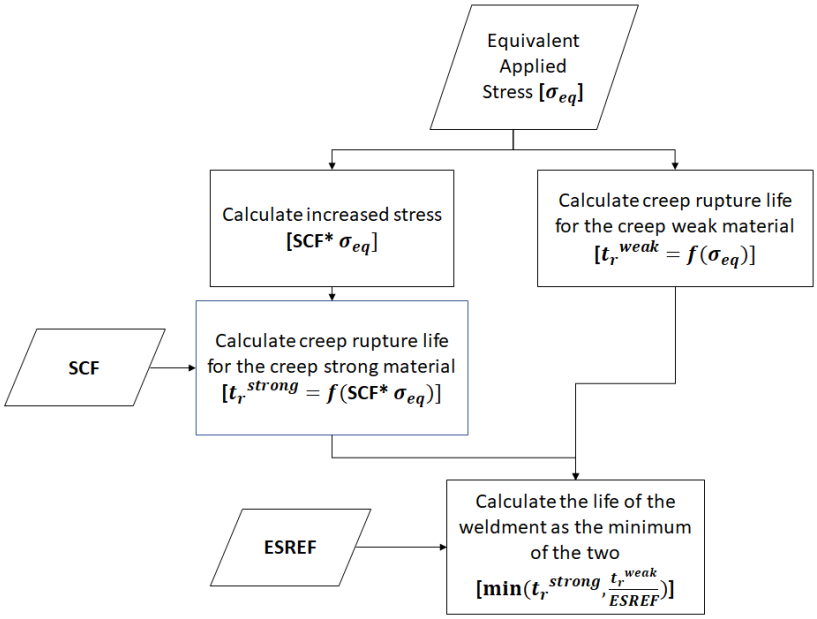

Figure 3.26: Flowchart showing the steps to calculate creep rupture life of a weldment

There are a few limitations of this approach. The application of this approach requires the knowledge of whether the weld is over-matched or under-matched which is sometimes difficult to ascertain due to the highly heterogeneous behaviour of the weld metal.

3.3.3 Conclusions

The following are the most important conclusions from this work:

1. A review of stress singularity in a bi-material weld model in creep showed that the strength of the singularity is independent of the state of loading i.e. axisymmetric or plane strain

2. Time independent plasticity does not alleviate stress singularity arising out of creep mismatch

3. A computationally economical FE model was developed using singular elements at the edge of a weld interface

4. Use of linearised stresses for calculation of stress and strain concentration due to creep mismatch in a bi-material weld model helps to ignore artificial peak stresses arising due to stress singularity

5. Since both stress and creep strain distributions are important for assessing rupture lives, measures for both are needed to fully define the effects of creep mismatch. Therefore, a strain rate enhancement factor was introduced, which took into account any increase in the creep strain rate from the nominal values under a loading condition. Also, the effect of stress triaxiality was included in the definition as that contributes to a faster accumulation of damage for the same strain rate.

6. Maximum stress concentration factors increased with an increase in creep mismatch while unaffected by the magnitude of applied stress and the weld aspect ratio. The maximum equivalent SREF increased with increase in mismatch as well as the magnitude of applied stress but unaffected by the weld aspect ratio. Since the maximum level of mismatch in a similar metal weldment cannot be practically greater than one order of magnitude, the corresponding SCFs can serve as bounding values for use in creep design. For design, rupture stresses will be significantly lower than 100MPa and therefore, the SREFs obtained for 100MPa and one order of magnitude mismatch in creep rates between the parent and the weld can serve as bounding values for design.

7. Finally, a method was proposed to calculate creep rupture lives of a weldment using both the stress and strain concentration effects arising out of creep mismatch.

CHAPTER 4

INVESTIGATION OF VARIATION OF CREEP RATES IN A 316H MULTI-PASS WELD

> *"All generalizations are false, including this one."*
>
> Mark Twain

Weldments are generally heterogeneous due to the inherent variation of microstructure and/or morphology introduced during the welding process (Chassignole et al [144]). Multi-pass austenitic steel welds have heterogeneous elastic-plastic and creep properties with a distinct difference between the weld and the base metal. The variation of mechanical and creep properties across a weld may lead to localisation and increase of creep strains and multi-axial stress states. Both creep strains and stress multiaxiality affect creep damage accumulation. Therefore, it is essential to characterise elastic-plastic and creep properties in a weldment for accurately modelling creep damage. Creep and creep-fatigue failures have been commonly found to occur in the heat affected zone (HAZ) of multi-pass 316H welds (Skelton et al [145], Bouchard et al [146]). The HAZ may develop graded creep properties due to cyclic strain hardening during the welding process. Digital Image Correlation (DIC) creep tests performed on a 316H crossweld specimen revealed a non-uniform distribution of creep strains across the weldment, with different creep rates at the weld, HAZ and the base metal (Sakanashi et al [4]). At present, there is a scarcity of HAZ creep data which prohibits an accurate characterisation

of creep rates across a 316H multi-pass weld. Moreover, there is also a lack of any qualitative estimates of the type of variation and the extent of the material zone in which the creep rates vary. A qualitative model of the variation of creep rates in the HAZ can greatly aid development of analytical models for weldment creep by a) giving an idea of the effective size of the material zone where the creep rates vary and b) the nature of variation.

Therefore, in order to characterise the HAZ creep behaviour, it is important to first investigate the creep behaviour of different material regions in the weld. One of the key indicators of creep behaviour is the minimum creep rate which can be relatively easily measured using localised tests such as an impression creep test. It should be noted that the interest of this work is limited to the determination of the any variation of creep rates on the HAZ/parent side of a 316H weldment and in the vicinity of the weld fusion line. Such a region of material with different creep properties than the far away parent material represents a strain affected zone (SAZ) and its extent may be different than the weld HAZ. However, for the sake of convenience, HAZ/parent or HAZ are used to represent this region of creep variation in this treatise. In this chapter, minimum creep rates across the HAZ/parent section of a multi-pass 316H weldment were investigated using impression creep tests in order to build a profile of minimum creep rates versus distance from the weld fusion line in the HAZ/parent section of the test weldment. As the focus was on creep deformation and not damage, impression creep test was chosen over an indentation creep test. A detailed description and literature survey on impression creep test can be found in section 2.3.1.

In this work, an ex-service multi-pass 316H was chosen. The Test Weldment (Internal transmittal [147]) is a similar metal weld where the parent material is 316H and the weld metal is 316L. The parent and the weld metal, therefore, have very similar compositions except slightly different carbon content. In a multi-pass weld, the HAZ generally has a different microstructure compared to the parent material. In addition to that in a multi-pass weld, a significant portion of the parent material, extending beyond the HAZ, undergoes cyclic strain hardening with each weld pass. Therefore, the test weldment can be considered to be a composite material with three distinct material regions: parent, HAZ and the weld, with a continuous or discontinuous variation of creep properties across it. The Test Weldment may have degraded in strength due to prolonged in-service operation in the plant. The original weld was partially repaired but the test weldment specimens were taken away from the repaired section for the present work.

Impression creep tests were performed on minature specimens taken from different regions

in the ex-service weldment in order to investigate the minimum creep deformation rates at each material region in the weld. Due to a variation in temperature and strain range as a function of distance from the weld fusion line during welding, it is possible that there is a significant variation of creep deformation rates in the HAZ/parent as a function of distance from the weld fusion line. Therefore, multiple specimens were extracted from different regions at different distances from the weld fusion line within the weld HAZ/parent. Localised creep tests on weldments can be found in literature. Prasanna et al [148] performed indentation creep tests on stainless steel welds. Hyde et al [99] performed impression creep tests on parent, weld and HAZ sections of a ferritic steel weld. Vijayanand et al [149] performed impression creep tests on a 316LN welded joint in order to grade the creep deformation rates across it. The impression creep tests described in this work used the same set up and a similar specimen design as Hyde et al [99]. In order to confirm the accuracy of the test method for qualitatively assessing the minimum creep rate variation in the weld HAZ/parent, impression creep tests were also performed on a weld and a parent test specimen and the results were compared against a finite element model of the test set up for the parent material.

4.1 Impression Creep Tests

4.1.1 Test Material

The weldment used for all the experimental work in this project is an ex-service 316H steel multi-pass weld. The weldment is a new girth weld made on a 316H ex-service parent material (Internal transmittal [147]). In addition, the girth weld included two weld repairs. The weld was made using a Manual Metal Arc (MMA) welding process. The parent material used in this work is a single cast of 316H, Cast 69431. The manufacturer of the weldment was Firth-Brown. The components were forged into cylinders for superheater headers with dimensions 565mm long, 431.8mm outside diameter and 304.8mm inside diameter (63.5mm thick) and were solution heat treated at $1050^{\circ}C$ for 3 hours followed by a water quench. The material for the present work was extracted from the Heysham 2C2/3 header. This header was in the ex-service condition and details of the service conditions and chemical compositions of the header can be found in Table 4.1 and Table 4.2 respectively. All data on the material were supplied by EDF Energy (Internal transmittal [147]). This material was in service for 65000 hours at a service temperature of $490^{\circ}C$

Initial Condition	Service (hours)	Service Temperature ($°C$)	Primary Hoop Stress (MPa)
1050$°C$ and 3h water quench	65000	490 to 530	~40

Table 4.1: Service Conditions of Cast 69431 HYA 2C2/3 Header material

Element	Composition (%)	Element	Composition (%)
C	0.07	N	0.03
Si	0.42	Al	<0.005
Mn	1	Cu	0.15
S	0.016	Nb	<0.005
P	0.021	Sn	0.012
Ni	11.4	Ti	<0.005
Cr	17.1	V	0.036
Mo	2.3	W	0.06
Co	0.09	Ta	<0.01
Bo	0.002	-	-

Table 4.2: Composition of Cast 69431 316H steel

Welding details	Heysham 2C2/3 Weld
Type	HYA/HRA S5
Geometry	Girth
Preparation	V and V root
Weld Process	MMA
Thickness (mm)	63.5
Condition	As welded and repair welded
Weld Metal	Babcock Type S
Repair depth (%)	75
Comments	Repaired once, HAZ not removed
Length (mm)	100

Table 4.3: Welding details of the Heysham 2C2/3 weld

to 530$°C$.

The weldment used in this work is a new multi-pass girth weld made on the Heysham 2C2/3 header material described above. In addition, the girth weld included two weld repairs at 90° and 270°. The weld was made using an MMA process. These repairs removed the full width of the original girth weld and were 100mm long (at the maximum depth), 75% of the thickness in depth. The welding details are given in Table 4.3. Babcock S type 316L weld filler metal was used with a δ-ferrite composition of 3-8%. The supplied material blank is shown in figure 4.1.

In this thesis, the term "Test Weldment" will refer to the new weld (with repairs) made on the ex-service cast 69431 316H header material as described above. The terms "Parent", "HAZ" and "Weld" will indicate the parent material, the Heat Affected Zone (HAZ) and the weld metal of the Test Weldment respectively. However, it should be noted that the material blank used

Figure 4.1: Supplied material blanks of ex-service 316H steel weldment

Temperature $°C$	Elastic Modulus, E (GPa)	Poisson's Ratio, ν	0.2% Proof Stress, $\sigma_{0.2}$ (MPa)	UTS, σ_{UTS} (MPa)
550	165	0.3	170	588

Table 4.4: Composition of Cast 69431 316H steel

for fabricating test specimens for this work were taken from an area away from the repaired section. Therefore, the weld repair will not affect the HAZ or the weld properties of the ex-service weldment. Figure 4.2 shows the geometry of the test weld. The weld groove has an angle of 15°.

The temperature dependent physical and mechanical properties of this material are given in table 4.4. The elastic modulus and Poisson's ratio values are taken from (Hares et al [150]) and the proof stress and ultimate strength are taken from (Oh et al [151]).

Figure 4.3 shows the stress strain response of the parent and HAZ material sections of the test material at 550°C (Internal transmittal [152]). The HAZ material displays a higher yield strength relative to the base metal. This is because of strain hardening of the HAZ during the welding cycles.

Although the RCCM-R model described in section 2.2.4 satisfactorily describes the mean, upper bound and lower bound creep deformation behaviour of 316H steels, there is significant cast to cast variation of mechanical properties along with variation due to service exposure.

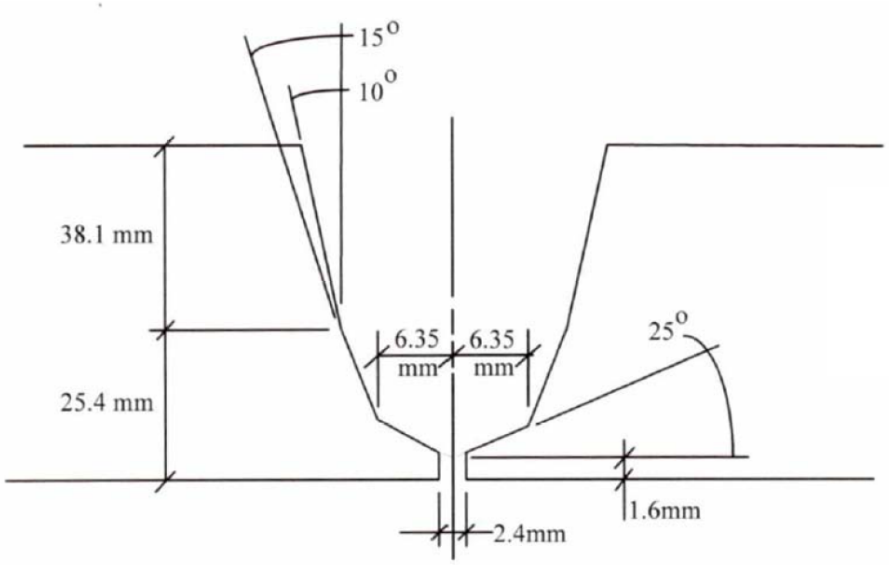

Figure 4.2: Test weld geometry

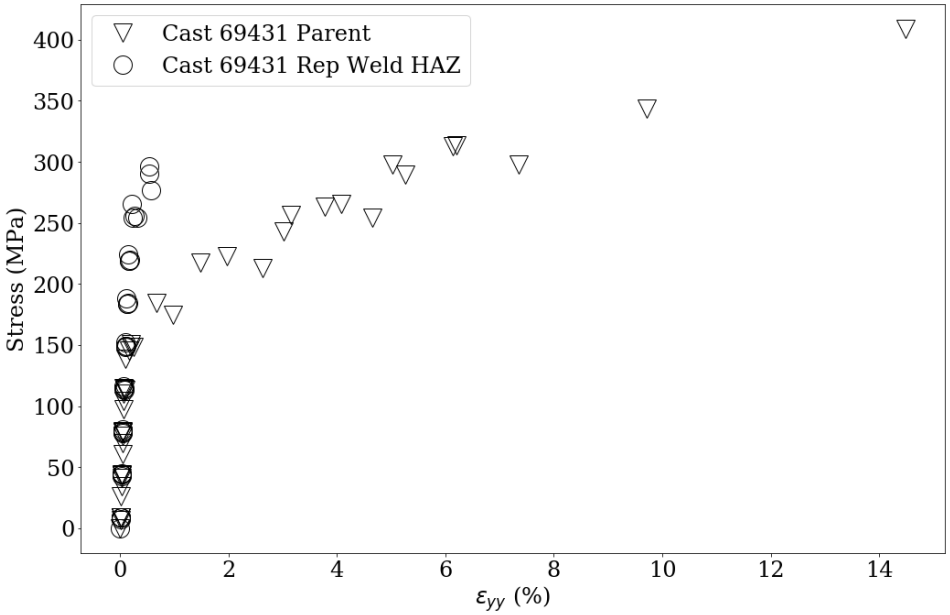

Figure 4.3: Stress strain curves of Cast 69431 REP weld

Therefore, for a better comparison of results from this work, conventional creep test data was obtained from earlier tests conducted on Cast 69431 ex-service material at a test temperature of $550°C$. Figure 4.4 shows the creep strain curves for the cast 69431 parent material for different true stress values (Internal transmittal [152]).

Figure 4.5 shows the creep strain curves for the cast 69431 HAZ material for different true stress values (Internal transmittal [153]).

4.1.2 Specimen Design

Figure 4.6 shows a schematic of the test material blank indicating locations from where different specimens were extracted. A total of five specimens were extracted from the HAZ/Parent at varying distances from and starting at the weld fusion line. One specimen each from the far away parent and the weld centreline were also extracted to serve as benchmarks and comparison with available conventional test data. Figure 4.7 gives a 2D sketch showing the final dimensions, orientations and locations of the machined specimens with respect to the weld fusion line. The machined and finished specimens were 8mm x 8mm with a thickness of 1.75mm each (Figure 4.8). A minimum thickness of 1.75mm was selected for all the impression creep test specimens.

All machining was done using wire electro discharge machining (EDM) followed by grinding of the top and bottom flat surfaces to achieve a surface finish of R_a = $0.2\mu m$.

4.1.3 Test Data Analysis

As described in equations 2.7 of section 2.3.1, two conversion factors, η and β are required for interpretation of impression creep test data. These conversion factors are a function of geometry of the indenter and the specimen as described in section 2.3.1. A schematic of an impression creep test specimen in figure 4.9 shows the important geometric dimensions for a rectangular specimen impacting the values of the conversion factors. Hyde et al [94] showed that for a specimen with length b, width w, thickness t and with an impression area (indenter width) of d, the conversion factors are functions of the ratios $\frac{w}{b}$, $\frac{w}{d}$ and $\frac{h}{d}$.

Hyde et al [154] evaluated the creep conversion factors for a rectangular indenter for a range of indenter and specimen geometry. For a rectangular specimen with $\frac{w}{b}$ = 1 and $\frac{w}{d}$ = 10, the conversions factors were plotted against $\frac{h}{d}$ in Hyde et al [94] and are presented here in figure

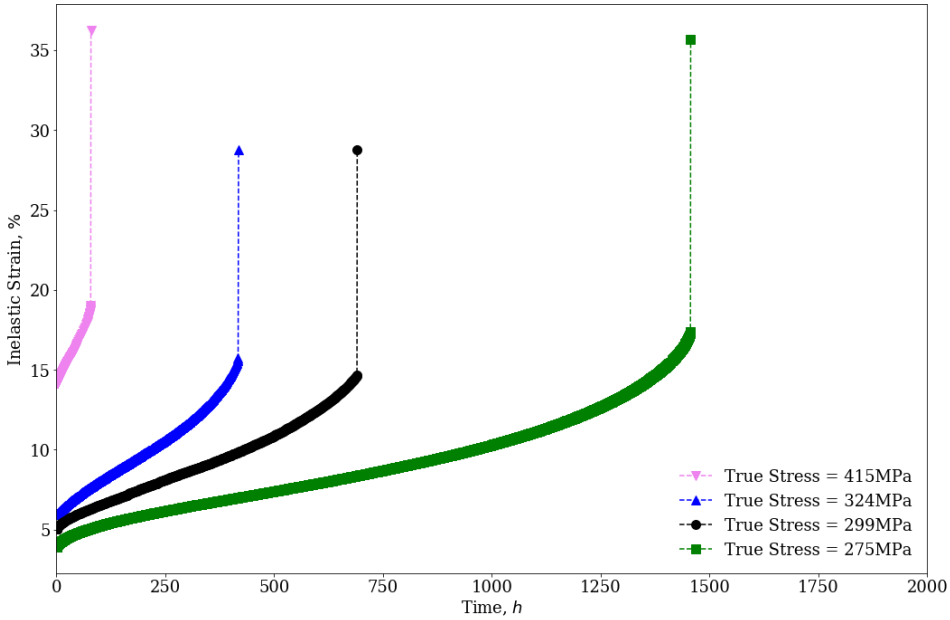

(a) Plot of creep strain versus time for stresses in the range $[275MPa, 415MPa]$ at a temperature of $550°C$

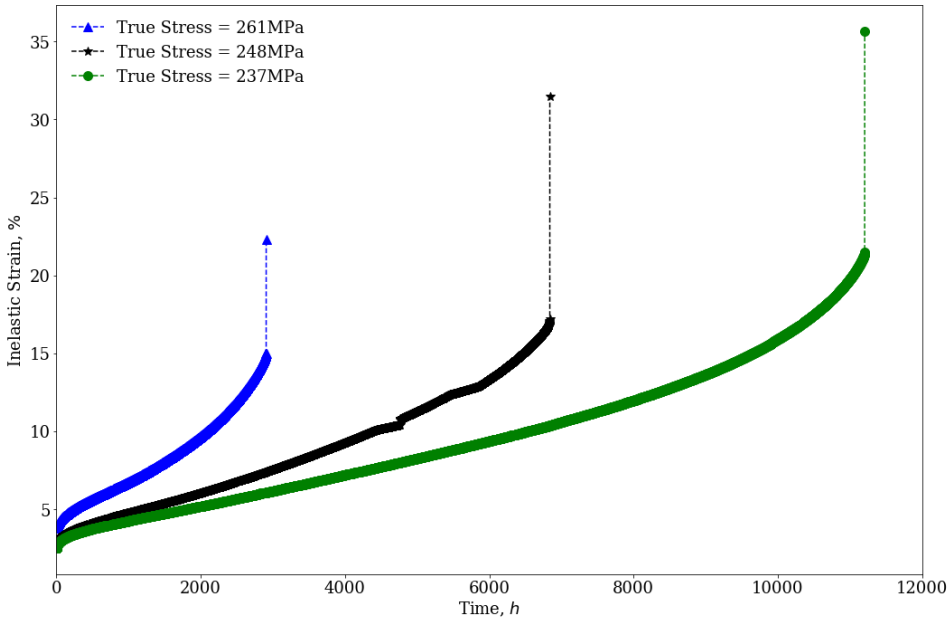

(b) Plot of creep strain versus time for stresses in the range $[237MPa, 261MPa]$ at a temperature of $550°C$

Figure 4.4: Creep strain curves for Cast 69431 parent material for different stresses

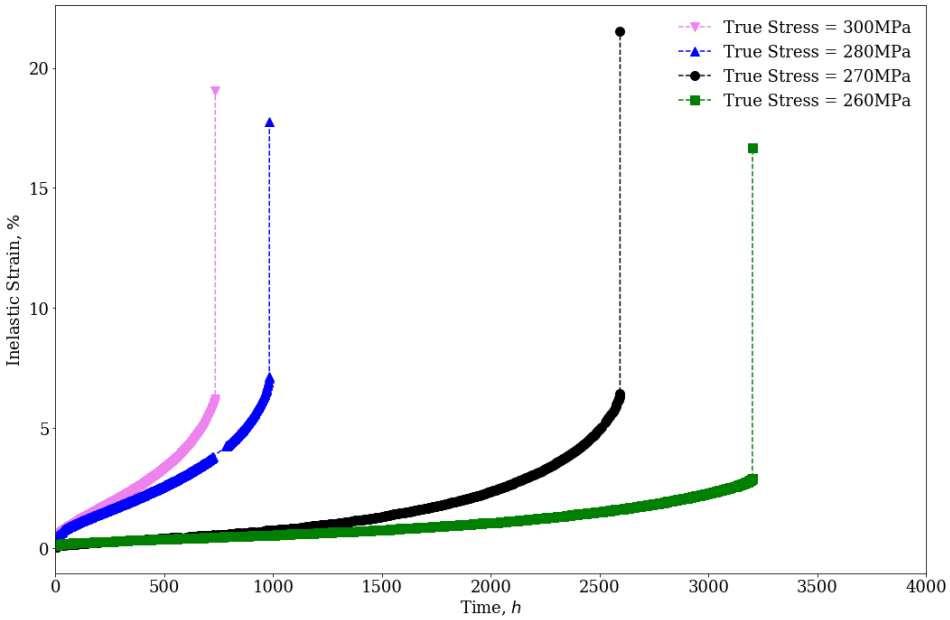

Figure 4.5: Creep strain curves for Cast 69431 HAZ material for different stresses. Creep strain versus time for stresses in the range $[260MPa, 300MPa]$ at a temperature of $550°C$

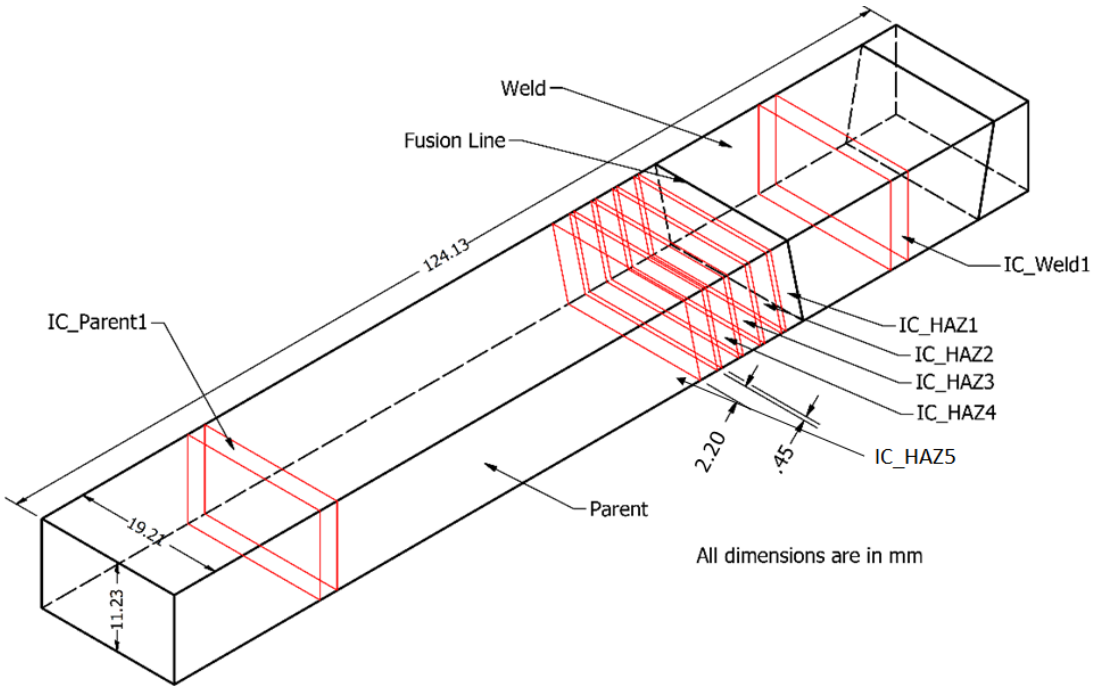

Figure 4.6: Schematic showing the test raw material and the different locations along the weldment from where the test specimens were extracted

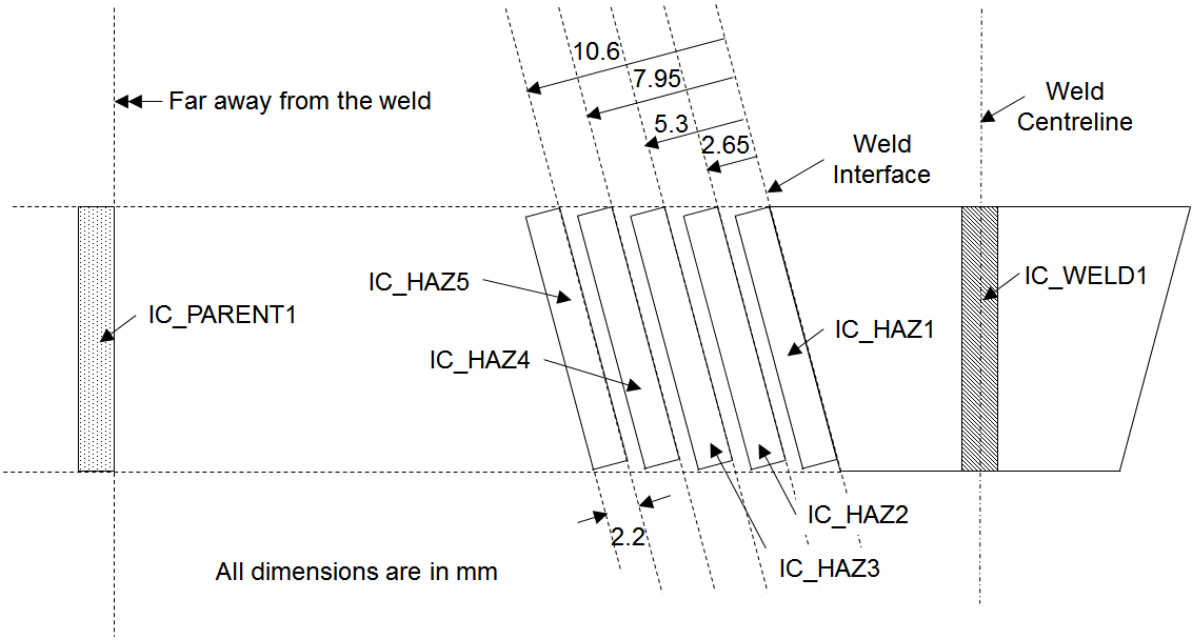

Figure 4.7: Schematic showing the actual distances of the machined test specimens from the weld fusion line

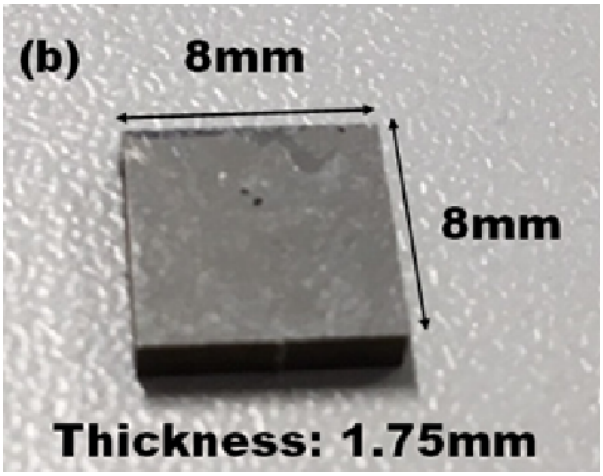

Figure 4.8: A photograph of a typical impression test specimen showing the important dimensions

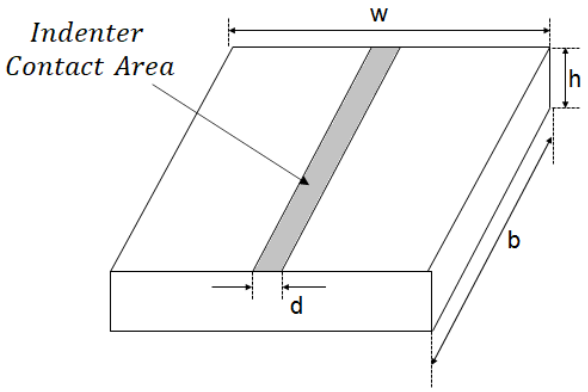

Figure 4.9: A schematic of a rectangular impression creep test specimen where length of the specimen is $'b'$, the width is $'w'$ and the thickness is $'h'$; the indenter width is $'d'$

4.10. For the test specimen shown in figure 4.8, the ratio $\frac{h}{d}$ has a value of 2.1875, which results in a value of 0.4429 for η and a value of 1.92 for β.

4.1.4 Test Set Up

The test design temperature and design equivalent uniaxial stress were $550°C$ and 330MPa respectively. As can be observed from figure 2.3 and section 2.2.1 of chapter 2, dislocation creep will be dominant at this stress and test temperature and hence power law creep will remain valid. The indenter used was a rectangular nimonic indenter of 0.8mm width (h). A value of 0.4429 for η meant that an indenter pressure of 745.1MPa was required to be applied on the test specimens for an equivalent uniaxial stress of 330MPa. As the test machine used a dead weight loading mechanism, it was impossible to apply the exact design pressure. Given the dimensions of the indenter and the test specimen, a force of 4820N was selected for the tests which resulted in an applied pressure of 753.1MPa or an actual equivalent uniaxial test stress of 336.6MPa.

Indenter penetration was measured using two linear variable differential transformers (LVDT) on two sides of the specimen (Figure 4.11). An induction furnace was used for heating up the specimen. Figure shows a photograph of the test set up at Nottingham University indicating the upper and lower loading bars (Figure 4.12). Table 4.5 shows the test parameters for each specimen tested.

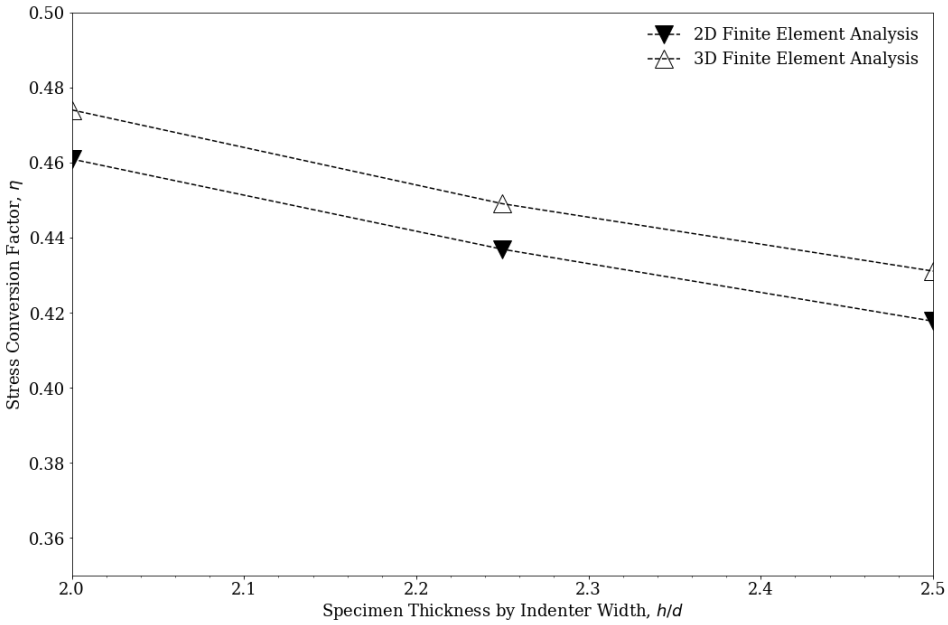

(a) Plot of eta

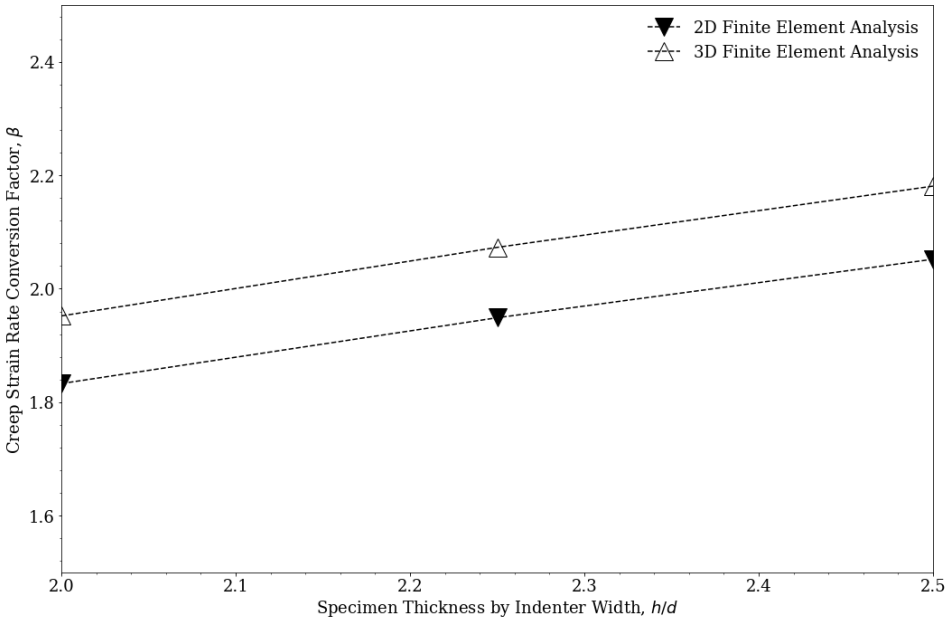

(b) Plot of beta

Figure 4.10: Plot of the impression creep conversion factors against the ratio of the indenter width to specimen thickness for a rectangular indenter

Specimen	Temperature ($°C$)	Test Equivalent Uniaxial Stress (MPa)	Test Load (N)	Total Run Time (h)
Parent	550	336.6	4820	416.83
HAZ1				332.87
HAZ3				306.67
HAZ5				432.37
Weld				522.63

Table 4.5: Test parameters for the impression creep test

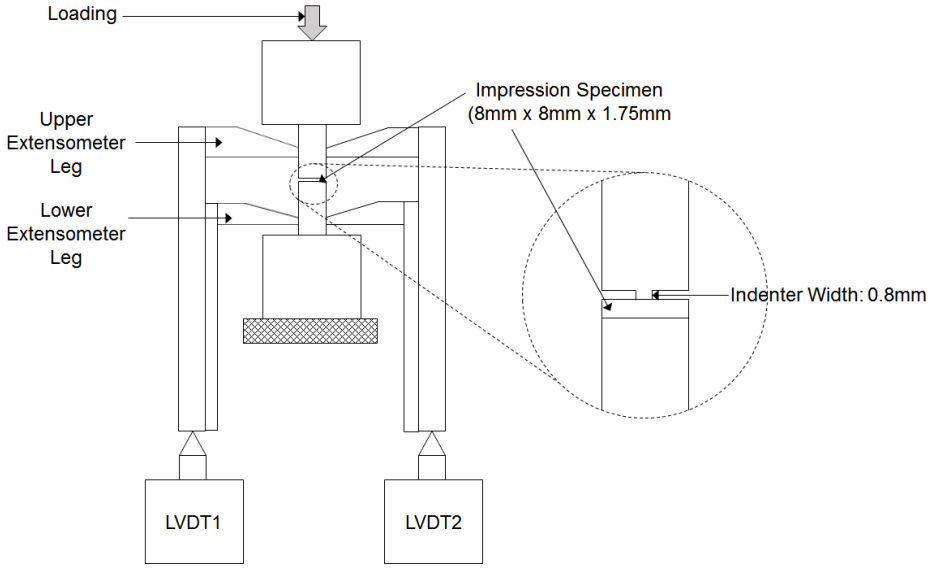

Figure 4.11: A schematic of the test set up showing the locations and arrangement of the LVDTs

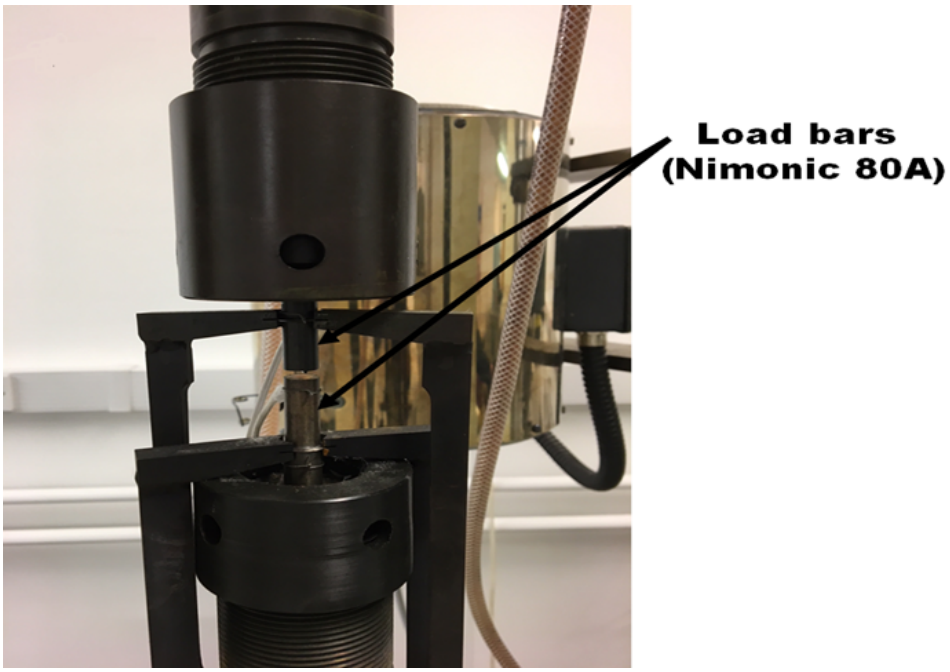

Figure 4.12: A photograph of the impression creep test set up at Nottingham University

4.2 Impression Creep Test Results

Figure 4.13 shows the raw impression creep test results for the Parent specimen. The impression depth versus time is plotted for LVDT1, LVDT2 and an average of the two. It can be seen that there is a significant difference between the two LVDT results which can be attributed to the indenter not being perfectly flat on the specimen. Although there is a significant difference in the deformation values of the two LVDTs, the difference in the resultant deformation rates is not considerable. Also, it can be argued that since the same test set up was used for all the specimens with the same configuration of the indenter and because the difference between the LVDT results for all the specimens appears to be similar, the relative variation of creep rates across the different specimens will be unaffected. In other words, the ratio of creep rates for the different specimens obtained from this test set up would remain the same as for a perfectly aligned indenter. Later, comparison of the parent creep results to an FE model based on the documented creep constants for the parent material will help in determining the actual creep rates in the HAZ sections if needed. LVDT1 results show considerable scatter. Figures 4.14 to 4.17 show the raw test results for the specimens HAZ1, HAZ3, HAZ5 and Weld respectively. All the raw results show a similar trend with the HAZ specimens showing a high amount of scatter. It is important to note that it is difficult to get a constant impression rate for any of the specimens even beyond 300h. This is a characteristic of an impression creep test, the penetration/ impression rate never actually becomes constant. This calls for careful analysis of impression creep data.

The raw data from the tests were divided into intervals of 1h each. An average creep rate for each of those intervals was estimated by fitting a straight line for each interval of data. The slopes of the straight lines represent the average impression rates for each interval. The average impression rate for each interval is plotted against time in figure 4.18. As the purpose was to compare the relative creep rates across different samples and LVDT1 results showed a lot of scatter, only LVDT2 raw data was used instead of the average. It can be seen that all the creep rates decrease with time as expected, except the weld results. The weld results show a flat initial portion followed by a tiny amount of variation of impression rate with time. This may be because of complex initial strain redistribution and secondary creep starting early in the weld material even before the initial strain redistribution has completed. Since the maximum duration of test was for the weld sample, which was greater than 500h, for parity, the impression rate at 500h

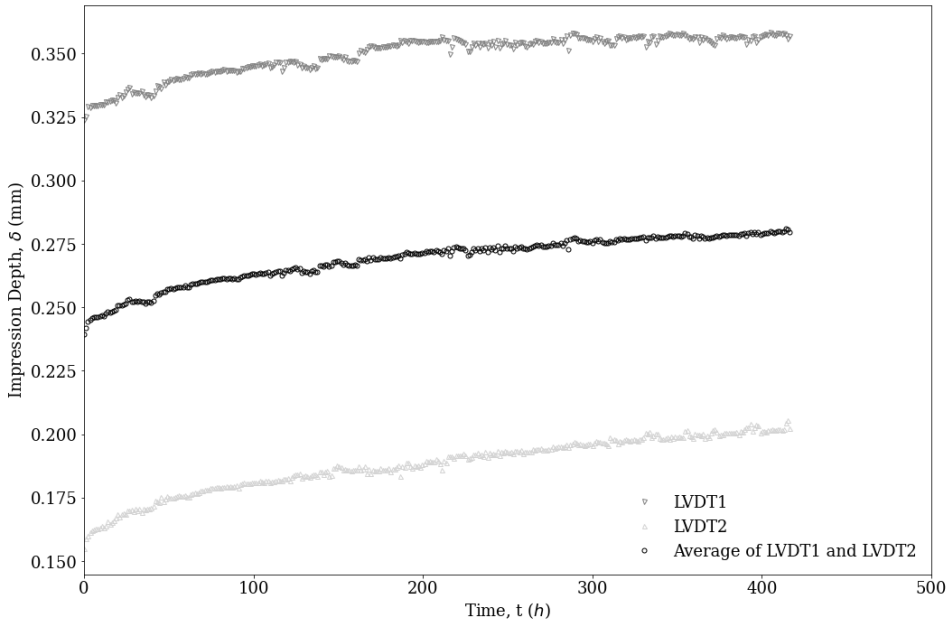

Figure 4.13: Raw impression creep results of the Parent specimen showing impression depth versus time for the two LVDTs and their average

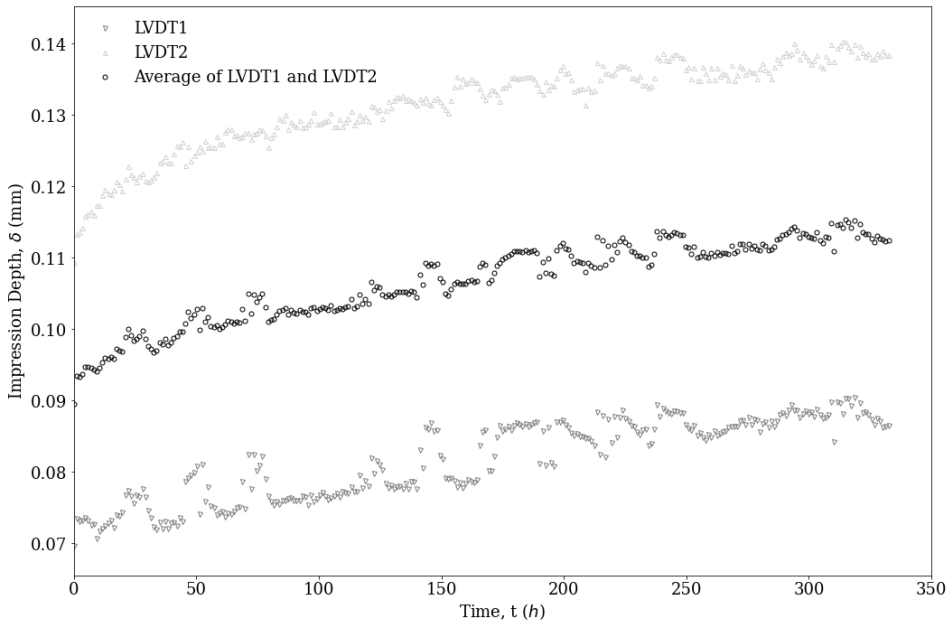

Figure 4.14: Raw impression creep results of the HAZ1 specimen showing impression depth versus time for the two LVDTs and their average

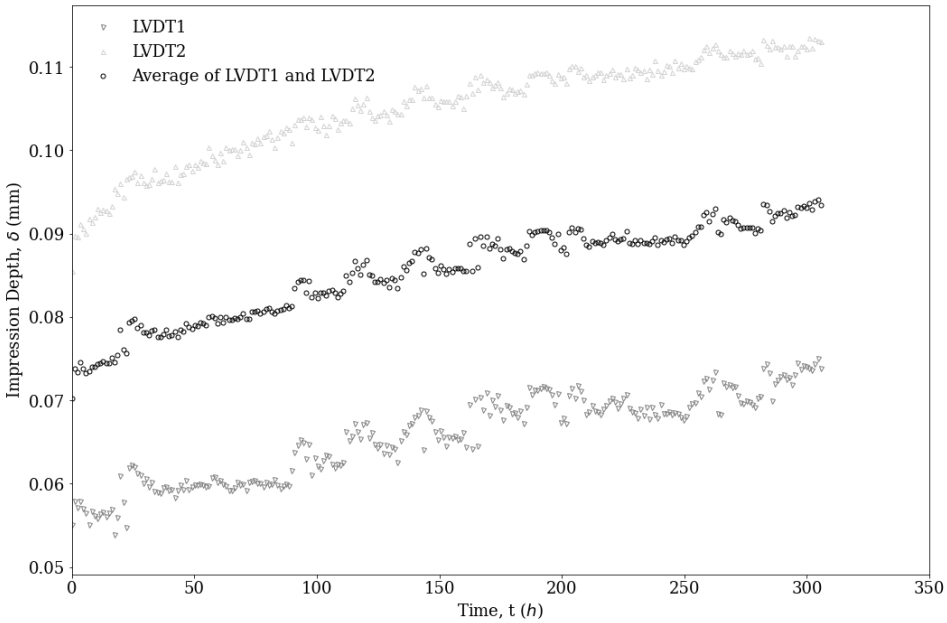

Figure 4.15: Raw impression creep results of the HAZ3 specimen showing impression depth versus time for the two LVDTs and their average

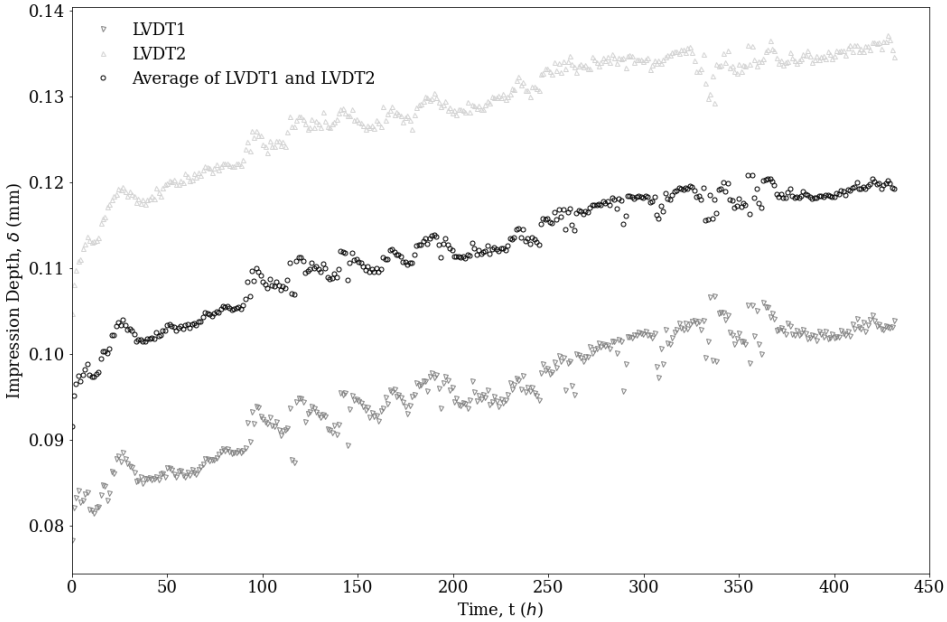

Figure 4.16: Raw impression creep results of the HAZ5 specimen showing impression depth versus time for the two LVDTs and their average

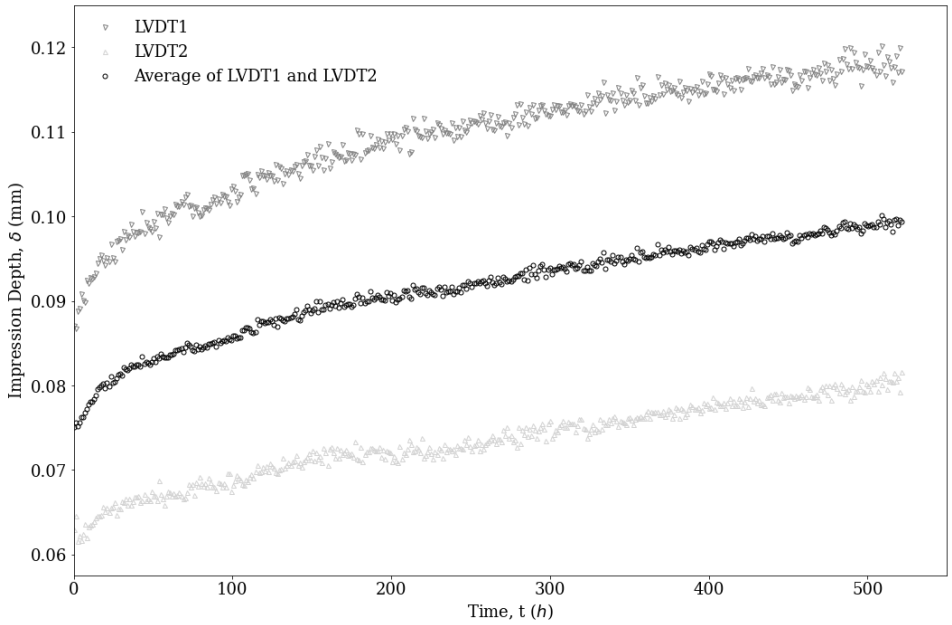

Figure 4.17: Raw impression creep results of the Weld specimen showing impression depth versus time for the two LVDTs and their average

was derived for the minimum creep rate calculations for all the specimens. For the other test specimens, the impression rates were extrapolated at 500h using a power law fit. This should be acceptable as the figures 4.15, 4.16 and 4.17 show that all the specimens had reached steady strain rate levels within their respective test durations.

Using the conversion factors derived in section 3.2.1, the minimum creep rate for each test specimen was derived. A bar plot of the minimum creep rates for the different specimens is shown in figure 4.19. The error bars at the top of the bars represent the error in the power law fits used to calculate the creep rates. It can be seen that the creep rates do not significantly vary between the HAZ specimens. The minimum creep rates in the parent and the weld specimens differ by less than an order of magnitude.

In an early work, conventional creep tests were carried out on the parent and the HAZ sections of the test weldment used for the impression creep tests (parent 316H creep data [152] and HAZ 316H creep data [153]) where round specimens oriented parallel to the welding direction were extracted from the HAZ section. In the present work, square shaped impression creep test specimens were extracted parallel to the weld fusion plane while indenter was oriented perpendicular to it. Therefore, it can be said that the direction of equivalent uniaxial stress or the direction of material flow in the impression creep tests correspond well with the orientation of

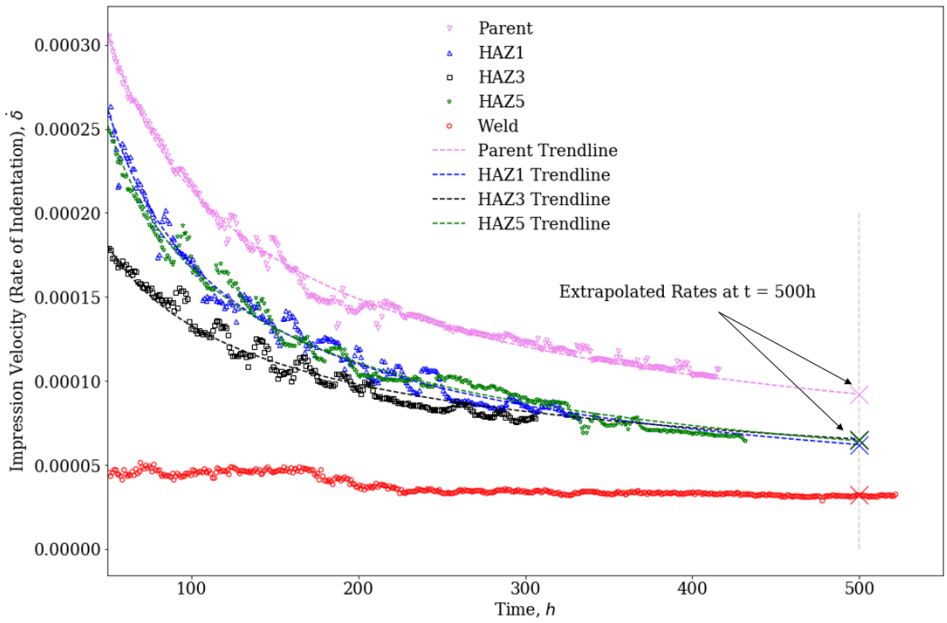

Figure 4.18: Impression velocity (rate of indentation) versus time for all the specimens and power law fits to all the specimens except the weld specimen

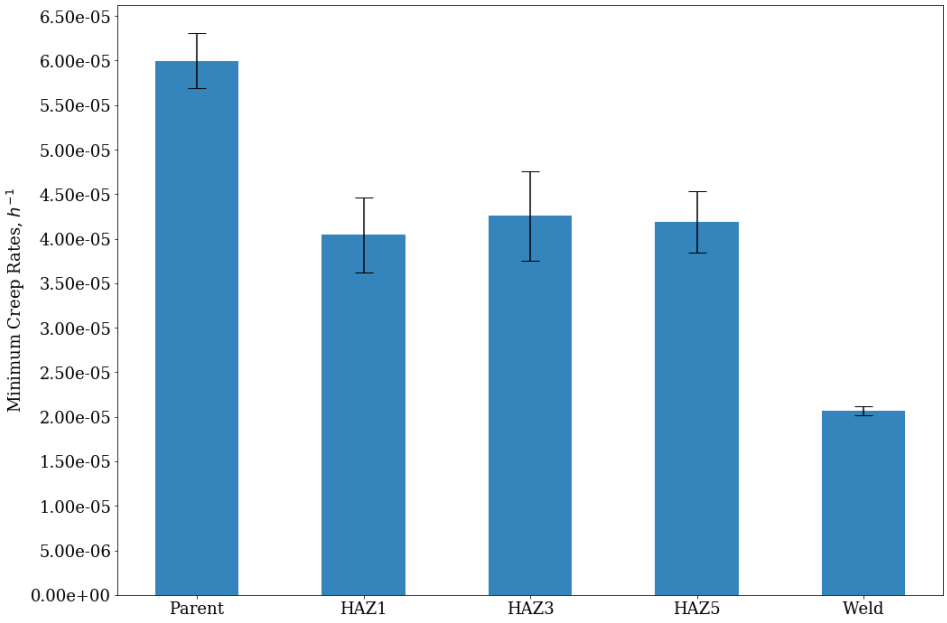

Figure 4.19: A bar chart of the minimum creep rates in the different impression test specimens along with error bars representing the error in the power law fits used to calculate the minimum creep rates

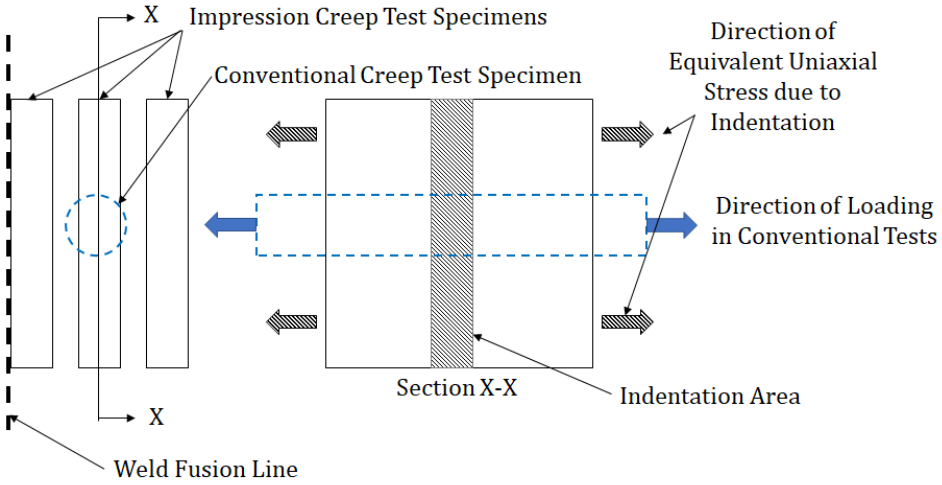

Figure 4.20: A schematic showing the effective loading orientation between the conventional and impression creep tests

loading in the conventional creep tests. Figure 4.20 shows a schematic comparison of the loading directions in both the types of tests.

Figure 4.20 is a schematic comparing the loading orientations of the conventional creep tests and the impression creep test. It can be observed that the orientation of the equivalent uniaxial stress or material flow in the impression creep tests correspond well with the loading direction used for the conventional creep tests. Figure 4.21 shows a comparison of the experimentally derived minimum creep rates for the parent and the weld specimens with that of the RCCM-R and conventional parent creep test data for the same cast of steel as the test material. The creep data from the conventional tests for this cast of 316H steel is presented in section 2.2.4. It can be seen that impression creep test under predicts the creep rate for the parent when compared to the conventional test data. The weld minimum creep rate is about half of that of the parent. The impression test parent creep rate falls well within the bounds of the RCCM-R model and slightly closer to the upper bound. The creep rates from the conventional tests fall on the upper bound of RCCM-R model which is slightly higher than the impression creep test result.

Figure 4.22 shows a comparison of the impression test minimum creep rates for the HAZ specimens with that of the RCCM-R model for 316H parent and conventional HAZ creep test data obtained for the same test material. The creep data from the conventional tests for this weld HAZ is presented in section 2.2.4. The conventional creep test data for HAZ shows a lot of scatter, with a sudden jump in the creep rate at a stress of 280MPa. Unfortunately, the conventional

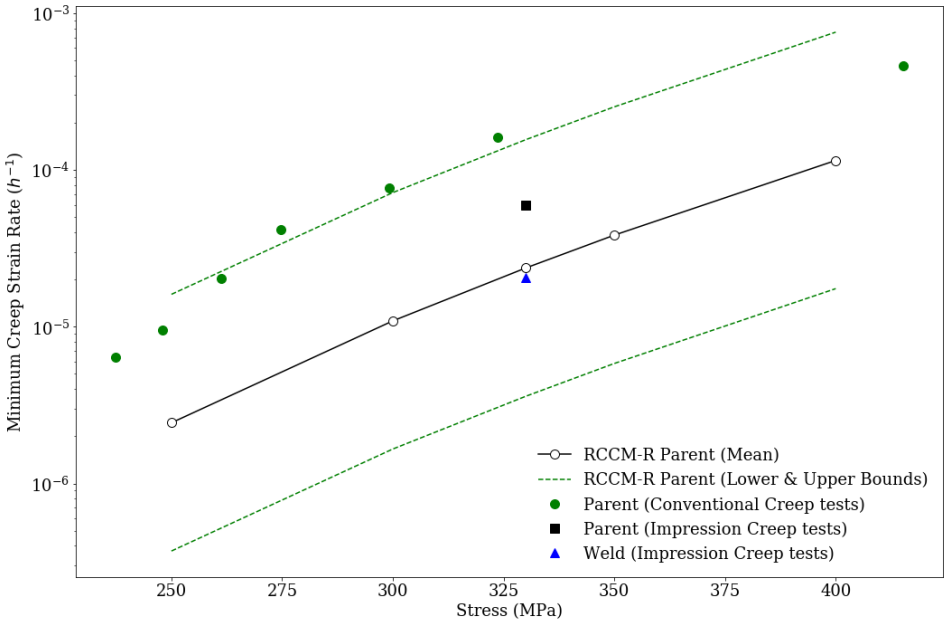

Figure 4.21: A comparison of the impression creep test derived minimum creep rates in the parent and the weld specimens with the RCCM-R model and parent conventional creep test data

creep data for the HAZ exists only for stresses up to 300MPa, much less than the impression creep test equivalent uniaxial stress of 331.6MPa. However, from the trend, it can be seen that the impression creep test under predicts the creep rates in the HAZ samples. The impression creep test results sit well within the upper and lower bounds predicted by the RCCM-R model.

Impression creep data inherently contains scatter (Sastry [98]) and is therefore mainly useful for qualitative assessment. Since only one set of tests were performed at one stress level, it is difficult to match the test results with the documented creep data for either the same cast of material or for 316H steel in general. However, the fact that the impression creep test results fell well within the confidence bounds for the RCCM-R model data, which is an averaged creep data over various casts of 316H steel and test parameters, there is good agreement of the impression creep test results with the documented data.

4.3 Analytical Benchmarking of Test Results

In order to compare impression creep test data to the 316H RCCM-R data for the base metal (Chen et al [35], R66 Materials Handbook [36]), a finite element model was developed for the impression creep test. The FE analysis was conducted in ABAQUS 6.14 finite element suite

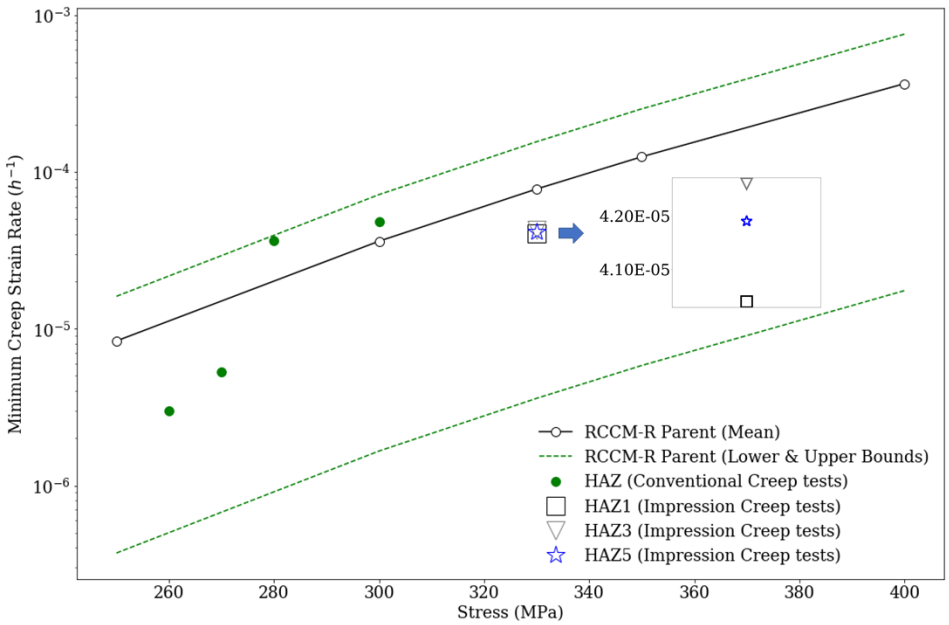

Figure 4.22: A comparison of the impression creep test derived minimum creep rates in the HAZ1, HAZ3 and HAZ5 specimens with the RCCM-R model and HAZ conventional creep test data

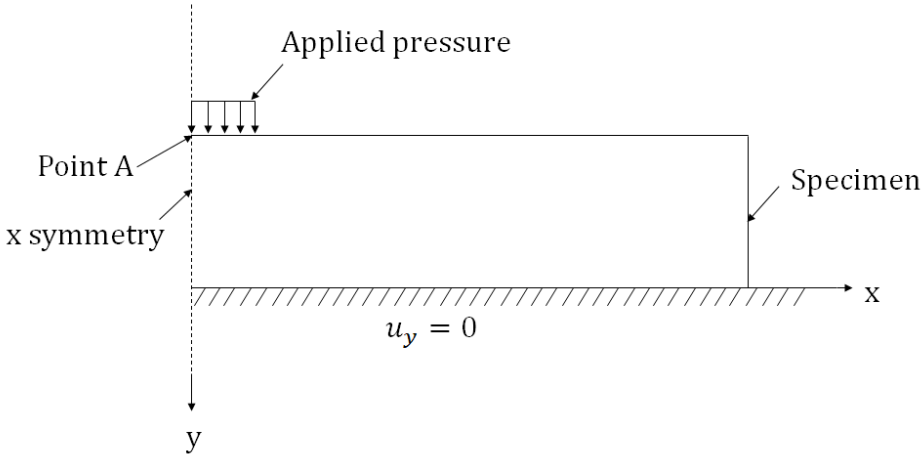

Figure 4.23: Schematic of the FE models showing the geometry and loading conditions

(ABAQUS 6.14 Documentation [132]). Displacement time curve for the indenter from the FE model was then compared against the impression creep test response for the 316H parent.

The geometry of the impression creep test specimens and the indenter enabled the use of a 2D plane strain approximation. As the specimen-indenter arrangement is symmetrical about the indenter axis, only one half of the specimen was modelled. Also, the FE analysis did not model the indenter in order to avoid contact modelling and reduce run times. A contact pressure

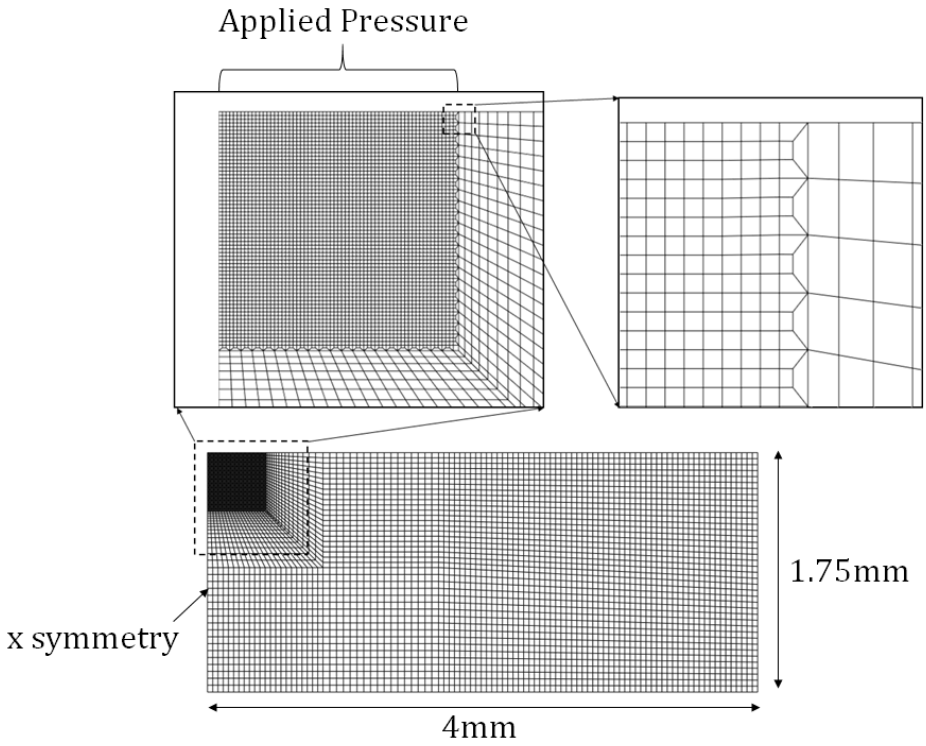

Figure 4.24: FE model mesh. Reduced integration linear elements were used for the analysis

equivalent to the indenter pressure was applied on the specimen and in an area equivalent to the indenter-specimen contact area. Also, instead of using a compression only boundary condition at the bottom edge of the model, a zero vertical displacement boundary condition was used. These simplifications were also used in Hyde and Sun [154] and shown to yield good results. Figure 4.23 shows a schematic of the model geometry with the boundary conditions and the applied pressure.

Mesh sensitivity was performed with both h and p refinements and an optimum mesh was obtained. Reduced integration linear elements were used. Figure 4.24 shows the FE mesh for the model. It can be seen that a good level of mesh refinement has been used in the area of the indenter edge as that area sees a high level of strain during initial plastic deformation and creep.

The elastic constants for the FE model were referred from section **??**. For a lack of published data on the elastic-plastic response of 316H steels at $550°C$ at such high stress levels, the elastic-plastic properties were fitted from the high temperature test data for cast 69431 316H steel as discussed in section **??** and presented in table 4.6. The highlighted row in table 4.6 are extrapolated values to enable convergence of the finite element solution beyond the maximum stress derived from the material test data. The multi-axial creep model as presented in equations

2.20 was applied for simulating the creep response of the material.

The RCCM-R creep constants, as presented in section **??** were used in the FE model. The creep constants are reproduced in table 4.7.

Yield Stress, σ_Y (MPa)	Plastic Strain, ϵ_p
157.44	0
265.84	0.03
313.32	0.05
533.17	0.25
698.10	0.40

Table 4.6: Stress-strain data used in the FE models for the weld and the parent material sections

Figure 4.25 is a contour plot of the equivalent creep strains in the model after 400h. It can be seen that the material under the corner of the indenter sees the highest amount of strains. Also, it can be observed that the zone of material undergoing a significant amount of creep extends to a little more than half the thickness of the specimen from the contact surface. Figure 4.26 presents a plot of total indentation depth or impression depth (δ_t) versus time for the FE model and compares it to the impression creep test results for LVDT2 as only LVDT2 results were used for deriving the minimum creep rates from the impression creep tests. The plot shows that there is a small difference in the initial depth of penetration of less than 0.05mm between the FE and the test results. This can be attributed to various simplifying assumptions made in modelling along with uncertainties associated with elastic-plastic properties of the material. However, it can be observed that the creep response has good agreement between test and modelling. Figure 4.27 plots the impression depth during creep (δ_c) for the FE model along with the impression creep test results for LVDT2. Here, 'δ_c' is defined as the total impression depth minus the impression depth upon initial loading. This plot makes a clear comparison of the creep rates between the analytical model and the experiment. It can be seen that at the FE results correspond closely to the LVDT2 output. These plots suggest that the conversion factors used for interpreting the impression creep data were correct. The validity of the impression creep test data is substantiated by the good correspondence of the FE results to the test results. Since RCCM-R creep data was used for the test, the agreement of analytical and test results indicate that for this cast of steel,

Temperature ($^\circ C$)	C_1	C_2	n_1	C	n
550	2.9618E-12	0.42131	4.18	5.2900E-26	8.2

Table 4.7: RCCM-R model constants for 316H steels

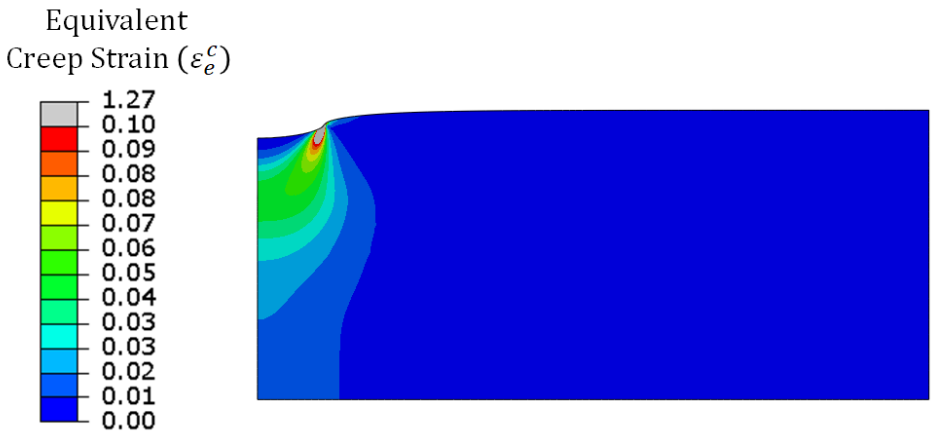

Figure 4.25: Equivalent creep strain distribution in the FE model after 400h

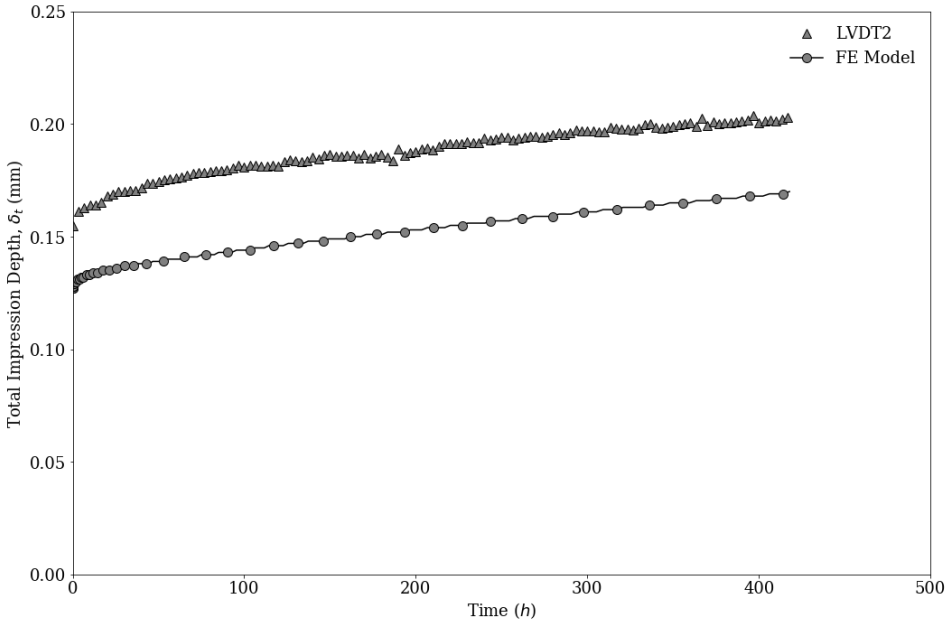

Figure 4.26: Plot of total impression depth with time for LVDT2 and FE analysis

the creep behaviour of this cast of 316H steel lies close to the documented mean creep properties of 316H steels at the test temperature and the applied load.

4.4 Conclusions

In this work it was demonstrated that impression creep tests can be successfully used to profile variation of minimum creep rates across the HAZ of a weldment. Although the results obtained

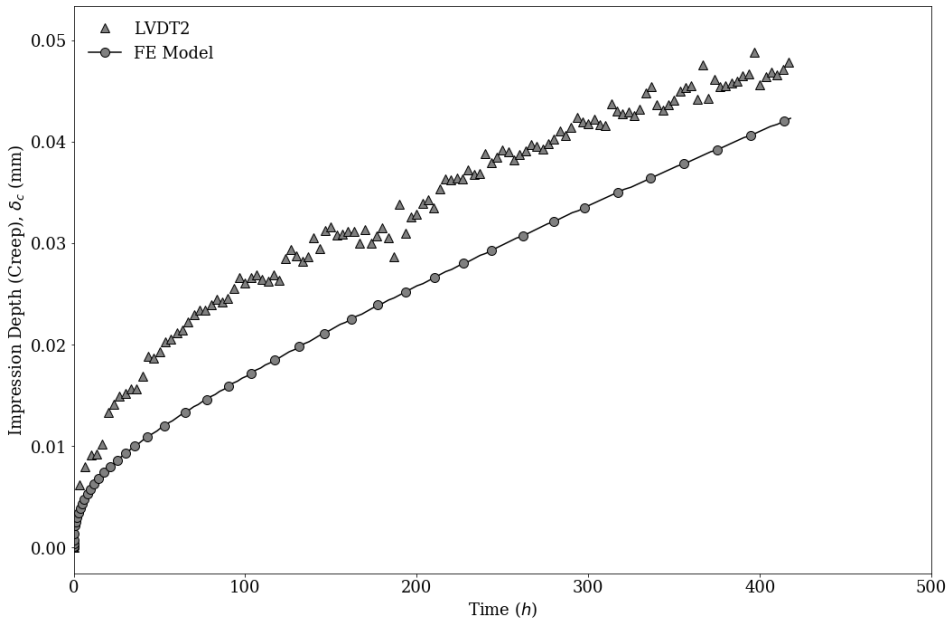

Figure 4.27: Plot of increase in impression depth with time during creep for LVDT2 and FE analysis

from these tests give a qualitative idea of relative variation in creep rates, these tests can be useful along with accurate creep data for the parent material in building more realistic finite element models incorporating a variation in creep rates across the HAZ.

It was found from the tests that in the test weldment, there was insignificant variation of minimum creep rates in the HAZ and base metal at 550°C and an equivalent uniaxial stress of 330MPa. The minimum value in the HAZ was within one order of magnitude of the base metal. Therefore, it can be concluded that for this type of weldments, using parent creep properties for the HAZ section can be used for simplified creep modelling.

A good agreement between the FE creep results and the impression creep tests confirmed that for the material, geometry and loading conditions used, the conversion factors remained constant well into the secondary creep regime. The change in geometry of the specimen during the first few hundred hours of creep deformation is therefore insignificant and hence constant conversion factors based on the initial geometry of a specimen can be safely used to interpret creep data.

CHAPTER 5

MEASUREMENT OF CREEP MISMATCH AND ANALYSIS OF ITS EFFECTS IN A 316H CROSSWELD SPECIMEN

> *"The proper method for inquiring after the properties of things is to deduce them from experiments."*
>
> Issac Newton

Multi-pass weldments exhibit variation of mechanical properties across different material sections (base metal, HAZ and weld metal). The difference in mechanical properties across different sections of material and their complex interaction makes estimation of creep damage evolution in a welded component extremely difficult. The first step in any creep damage assessment of a component is to model creep deformation and hence the accuracy and appropriateness of any creep damage calculation depends highly on the creep deformation modelling. In chapter 3, a theoretical study was conducted to understand stress and creep strain rate raising effects of any creep deformation mismatch across a simplified weld interface which showed that there can be a significant stress concentration effect across an abrupt weld interface due to creep mismatch. Chapter 4 experimentally determined if there exists a significant mismatch of minimum creep rates across different material zones (weld, HAZ and parent) of an ex-service multi-pass 316H weld using localised creep tests. It revealed that in this particular weld sample, there is insignificant (less than an order of magnitude) minimum creep

rate variation across the HAZ and between the near weld interface HAZ and far away parent. Full field creep tests of crossweld samples with all the material regions can help in drawing a complete picture of variation as well as interaction between the different material regions in a weld.

The aim of this chapter is to investigate the creep strain distributions in 316H crossweld specimens using experiments and finite element modelling and thereby develop an understanding of the effects and implications of elastic-plastic as well as creep mismatch between different material regions in the test material. It should be noted that the focus of the work is the region of material in the HAZ/parent side of the weld fusion line where the creep rates vary.

This piece of work attempts to build a picture of full field strains across different material regions of a crossweld and hence requires full field strain measurement techniques such as laser interferometry or digital image correlation (DIC). In this work, DIC based creep test was found more suitable and convenient mainly due to the availability of a test set up. Some of the earliest work on strain measurement using DIC are Peters et al [155], McNeill et al [156], Sutton et al [157], Chu et al [158] and Hung et al [159]. In more recent times, DIC based strain measurement technique has been successfully applied to creep testing (Lyons et al [105], Boyce et al [100], Sakanashi et al [160], Sakanashi et al [161] and Narayanan et al [162]). A comprehensive description on the DIC technique and discussion on earlier work on DIC based strain measurement has been given in chapter 2. Although, complete strain information over an entire gauge area can be obtained from DIC tests, they do not explain the stress states at each material point in the gauge area. In order to fully model the creep deformation process, it is important to estimate both the stress as well as the strain histories at each material point in the specimen. Therefore, finite element models were developed in conjunction with the aforementioned DIC creep tests and a complete picture of stress and strain history in the test material has been developed. Finite element modelling has been used along with DIC based strain measurement in some of the earlier work Cooreman et al [163], Moerman et al [164], Gerbig et al [165] and Narayanan et al [162].

5.1 DIC Creep Tests

Three DIC creep tests were done at a temperature of $550°C$ and different constant stress levels (Table 5.1). All the tests were conducted in a dead weight testing machine and a 3 zone induction

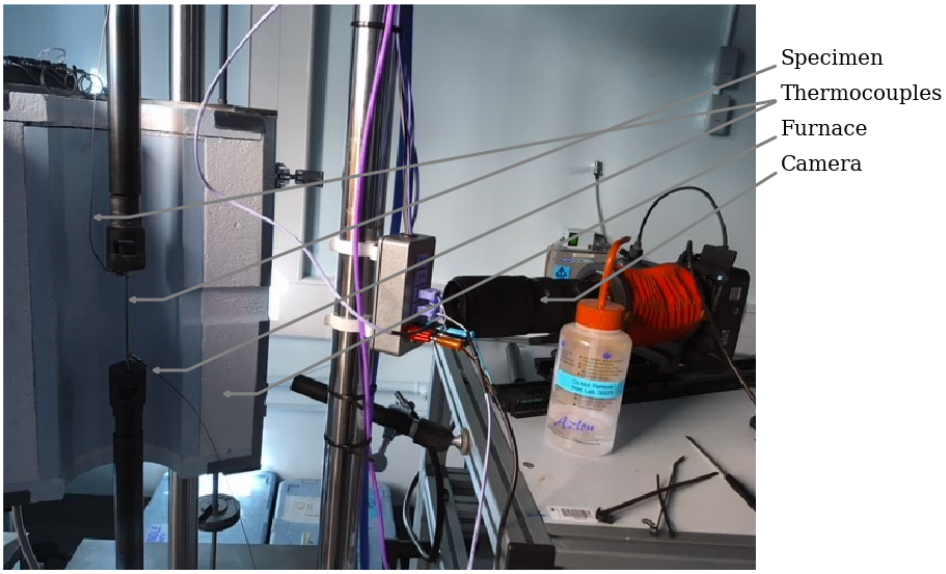

Figure 5.1: DIC Creep Test Set Up

heating furnace (figure 5.1). Thermocouples were fitted at the top and bottom of each specimen. It was shown that for this test set up, the middle zone temperature remains within $1°C$ (Sakanashi et al [161]). The specimens were placed at the middle zone of the furnace and oriented in a way to ensure that the gauge section of the specimens were clearly visible through the furnace window for imaging.

Test Name	Duration (h)	Temperature ($°C$)	Applied Stress (MPa)
2A	46	550	330
2B	2500	550	250
2C	342	550	300

Table 5.1: DIC creep test matrix

5.1.1 Test Material and Specimen Design

Section 4.1.1 of chapter 4 describes the test material used for all the tests for this research work. All the specimens have been extracted from an ex-service cast 69431 rep weld (4.1.1). Each specimen was extracted from a different region in the welded section.

All the test specimens have been designed following the rules described in ASTM standards ([166], [167]). Figures 5.2 and 5.3 show the specimen designs for the tests 2A, 2C and 2B. Since the main area of interest of the work is the strain hardened zone (SAZ) where the creep strain rate

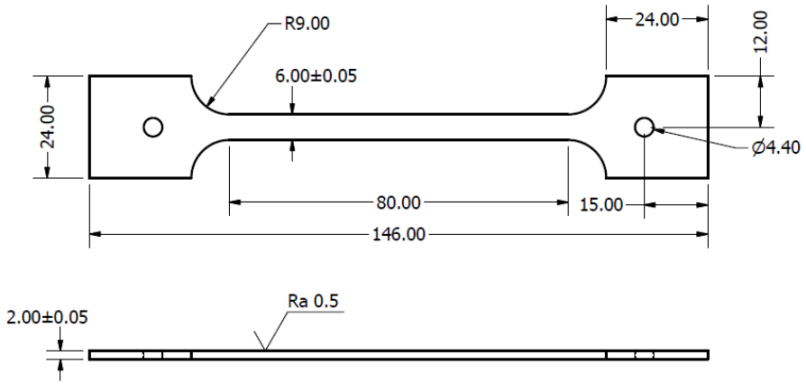

Figure 5.2: Specimen drawing for tests 2A and 2C

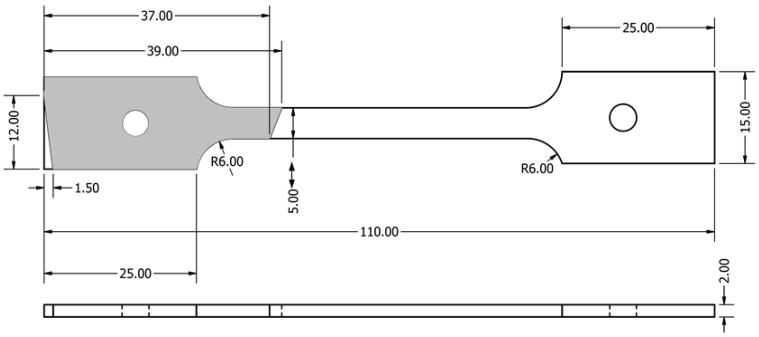

Figure 5.3: Specimen drawing for test 2B

varies and a limitation existed on the maximum length of each specimen, the test 2B specimen (figure 5.3) extracted from the thicker section of the weld is unsymmetrical with the weld situated at one end of the specimen.

5.1.2 Test Apparatus

A dead weight type tensile testing machine was used for all the tests. The frame was manufactured by Phoenix Calibration and Services Limited and has a lever arm ratio of 1:25 for load application. The furnace has three heating zones and the temperature is controlled manually with three different settings. The furnace was supplied by Severn Thermal Solutions Limited. A small window (40mm x 20mm) is located in the middle of the furnace for enabling DIC imaging. Heat padding was used at the top and bottom of the furnace and also on any gaps between the window frame and the outer wall of the furnace. N-type thermocouples were used for the tests which

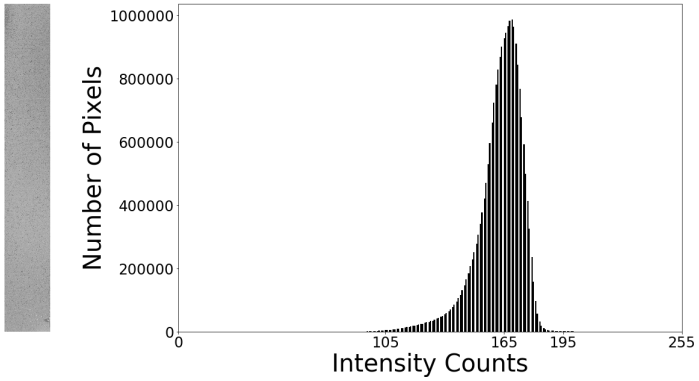

Figure 5.4: Image Histogram of Test 2A Speckled Specimen

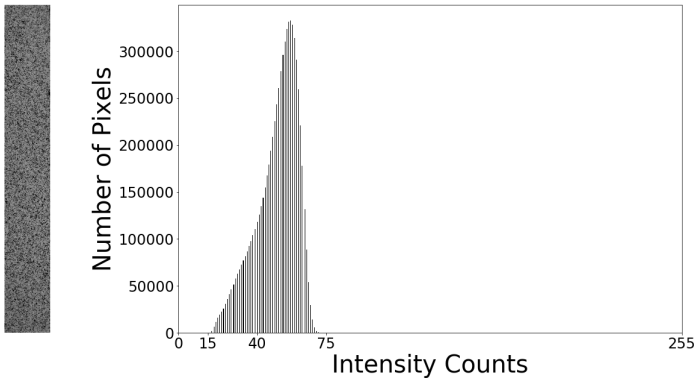

Figure 5.5: Image Histogram of Test 28 Speckled Specimen

were supplied by TC Direct.

5.1.3 Specimen Speckle Pattern

The measurement accuracy of DIC is highly affected by the image contrast (Crammond et al [168]). The image contrast determines the shape of the image intensity function. A higher contrast leads to better image correlation. Image contrast can be analysed by using image histograms. An image histogram is a plot of the number of pixels versus image intensity for an image. For an 8-bit image, the intensities vary from 0 to 255 pixels. The images obtained for the test specimen speckle patterns were converted to 8-bit images and their histograms have been plotted in (figures 5.4, 5.5 and 5.6). It can be seen that the images have sufficient contrast for the DIC tests.

The size of the speckle pattern is another important parameter as it determines the minimum

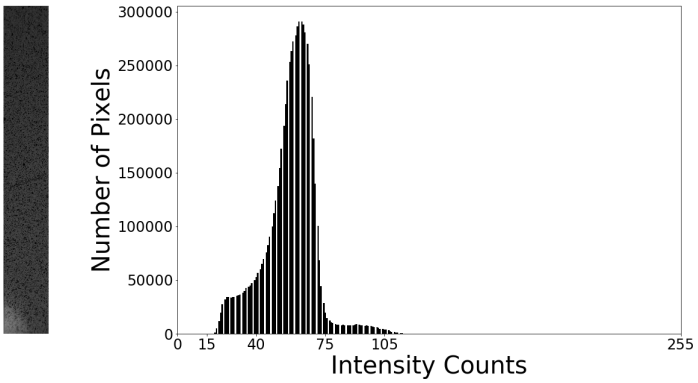

Figure 5.6: Image Histogram of Test 2C Speckled Specimen

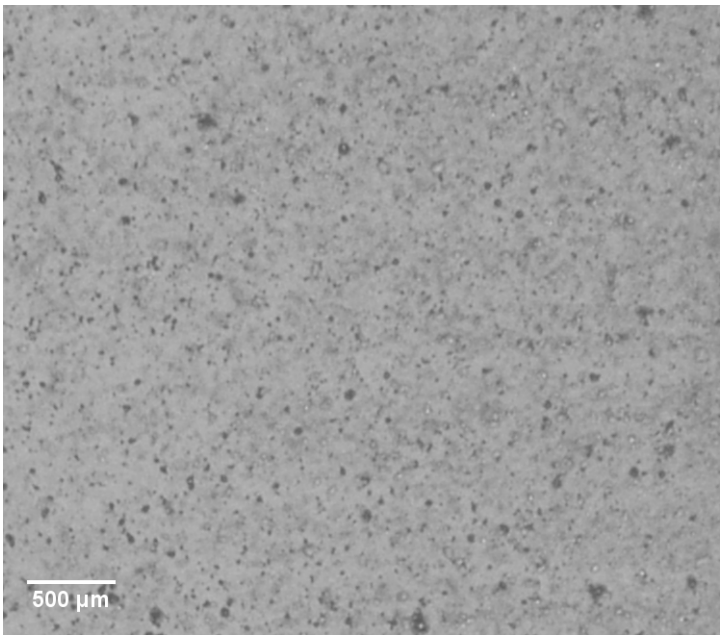

Figure 5.7: Image Histogram of Test 2A Speckled Specimen

subset size which can be used for image correlation. The aim is to generally have a high number of speckles within the subset used as this increases accuracy. However, too many speckles within a subset also adds to noise. Figures 5.7, 5.8 and 5.9 show the speckle sizes for tests 2A, 2B and 2C. It can be seen that the average speckle size across all the images is approximately $20\mu m$.

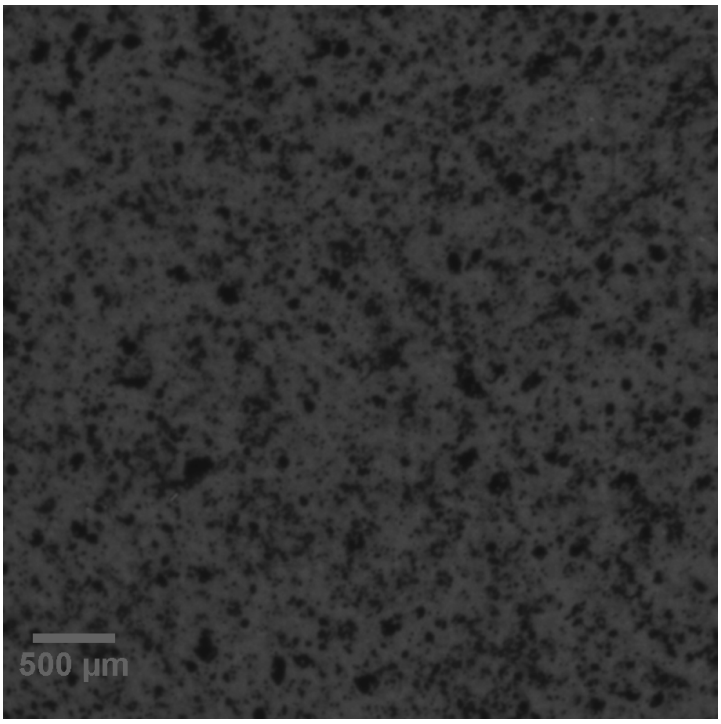

Figure 5.8: Image Histogram of Test 2B Speckled Specimen

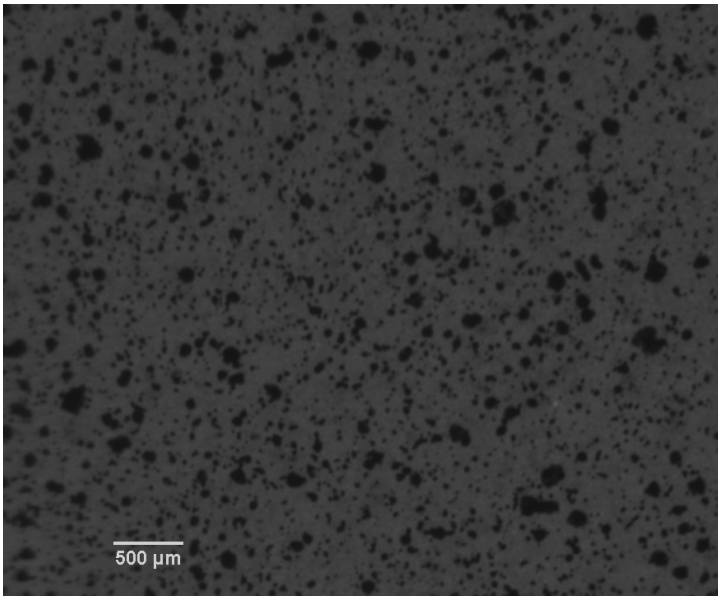

Figure 5.9: Image Histogram of Test 2C Speckled Specimen

5.1.4 Test Procedure

For each test, at first a load cell was used to calibrate the dead weight loading corresponding to the test load. Two N-type thermocouples were used for each test. The thermocouples were calibrated against a master thermocouple at 550°C. Table 5.2 shows the calibration temperatures for each set of thermocouples used in the tests. One thermocouple was attached to the top and another at the bottom of each specimen by wires and it was ensured that the tip of each thermocouple tightly remained in contact with the specimen face. For test 2C, two small holes were drilled on the specimens to hold the thermocouples. For each test, the specimen was then attached to the machine using specialised grips and the furnace was adjusted to position it between the specimen grips with the specimen gauge area clearly visible through the furnace window. The furnace was then closed and the camera was focussed on the gauge area for image checks. After the specimen, furnace and the camera were installed in place, the furnace was heated overnight and gradually to the test temperature. After approximately 10h of thermal soaking for each test, a reference image of the specimen was taken at the test temperature with 0 load (a small load of 5N was used to stabilise the load chain which is neglected here). The specimen was then loaded up slowly to the test load. For specimens 2A and 2B, an image was taken at each step of loading. This was to approximate a tensile response of the specimen since no separate high temperature DIC tensile tests were done on this material.

Test Name	Thermocouple	Calibration Temperature ($°C$)	Test Temperature ($°C$)
2A	Upper	551.3	550
	Lower	551.9	
2B	Upper	550	550
	Lower	553	
2C	Upper	554.9	550
	Lower	555	

Table 5.2: Thermocouple calibration for DIC creep tests

5.1.5 Data Analysis

The colour images obtained from the DIC tests were taken using a digital SLR camera (Nikon) which uses a colour filter called a "bayer array" (Matsutani and Takashi [169]). A bayer array consists of alternate layers of red-green and green-blue filters (figure 5.10). Thus, each pixel location in such a photograph will have only one colour information. For DIC data analysis,

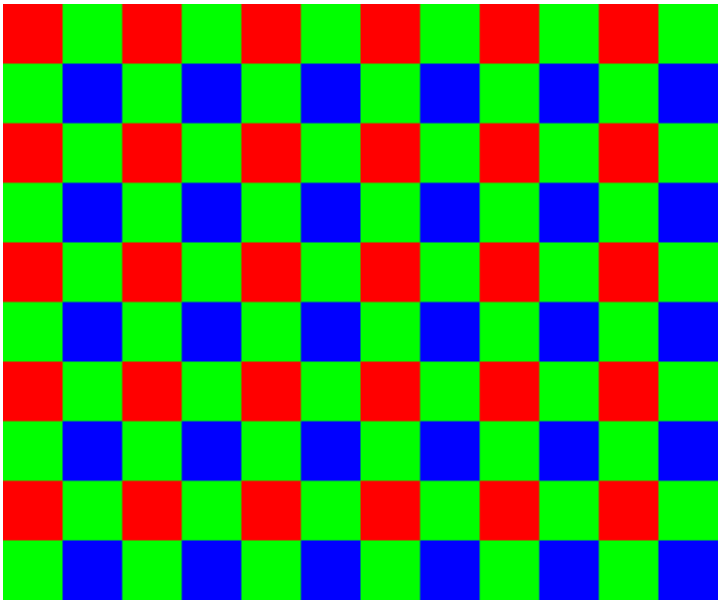

Figure 5.10: Schematic showing a bayer pattern

greyscale images are needed which consists of image intensity values at each pixel location. Therefore, in order to derive information of all the colours at each pixel location, it is mandatory to interpolate intensity values of all three colours at each pixel location. This process is called colour demosaicing (Forsey [170], Lukac et al [171]). In this work, a demosaicing scheme as described in (Forsey and Gungor [172]) was used. The method first performs demosaicing on the images using a bi-cubic interpolation followed by conversion to 16-bit greyscale images.

The greyscale images were analysed in Davis 8 software ([110]). All the images were corrected for rigid body rotations and translations followed by a Fourier transform based DIC algorithm for calculating deformation fields. A Gausian smoothing filter was used on the displacement field before calculating true strains. A subset size of 99 and a step size of 25 was used. All analysis parameters are listed in table 5.3.

Parameter	Value
Subset Size	99
Steps Size	25
Time Series	Relative to first
Outlier Filter	3x3 Gaussian smoothing filter

Table 5.3: DIC analysis parameters

Figures 5.11, 5.12 and 5.13 show the temperature histories of tests 2A, 2B and 2C respectively. It can be seen that temperatures for the top and bottom thermocouples for tests 2A and 2B

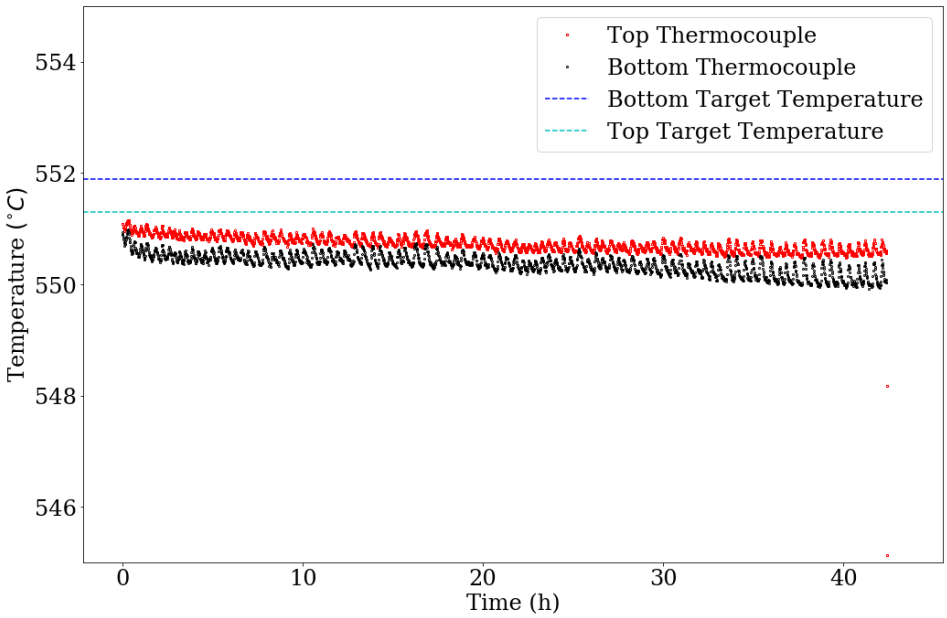

Figure 5.11: Temperature history of Test 2A

remained close to the target temperatures throughout the tests whereas for test 2C, there is a divergence of temperatures recorded by the top and bottom thermocouples between 120h and 170h of the test. Test data from test 2C may be unreliable beyond 120h of test duration. As the main objective of these tests is limited to creep deformation during the primary and secondary stages, data obtained up to 120h for test 2C should still be useful. For test 2B the top thermocouple temperature considerably deviates after about 3000h possibly due to large displacements associated with tertiary creep so all DIC test results up to 3000h should be valid.

For assessing noise levels associated with the test analysis parameters and the speckle patterns used, a test image correlation was performed on two images of test 2A taken at two different times before the application of load and at a temperature of 550°C. The result (figure 5.13) shows that in most of the gauge area, the longitudinal strains (ϵ_{yy}) had a magnitude of less than 0.1%. At the edges, there are tiny zones of strain values of up to 0.3%. Thus, the noise levels should be considered satisfactory.

5.2 Test Results

Specimen 2B (250MPa) failed at the parent material whereas the other two tests at higher stress levels of 300MPa (Test 2C) and 330MPa (Test 2A) failed in the weld. The creep lives were 43h,

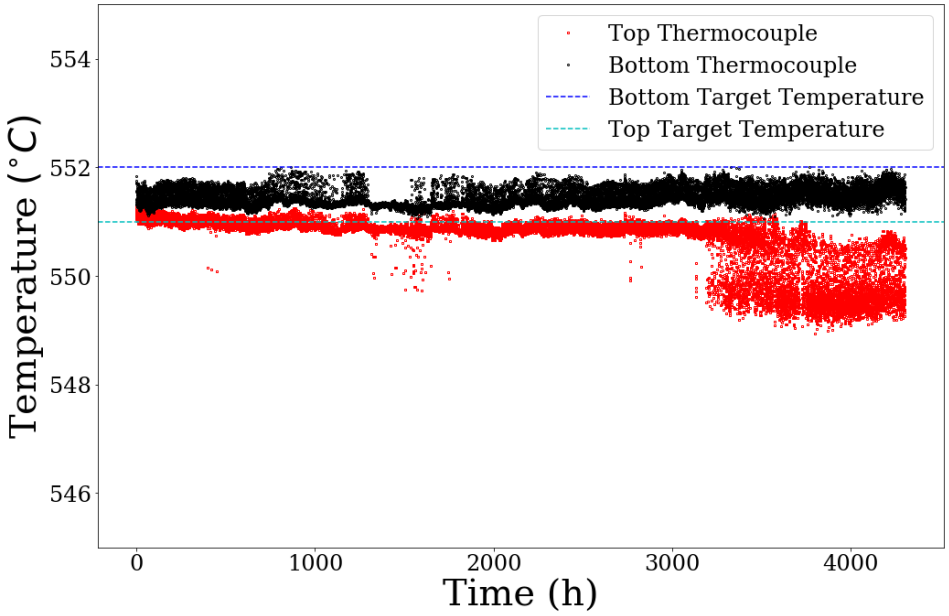

Figure 5.12: Temperature history of Test 2B

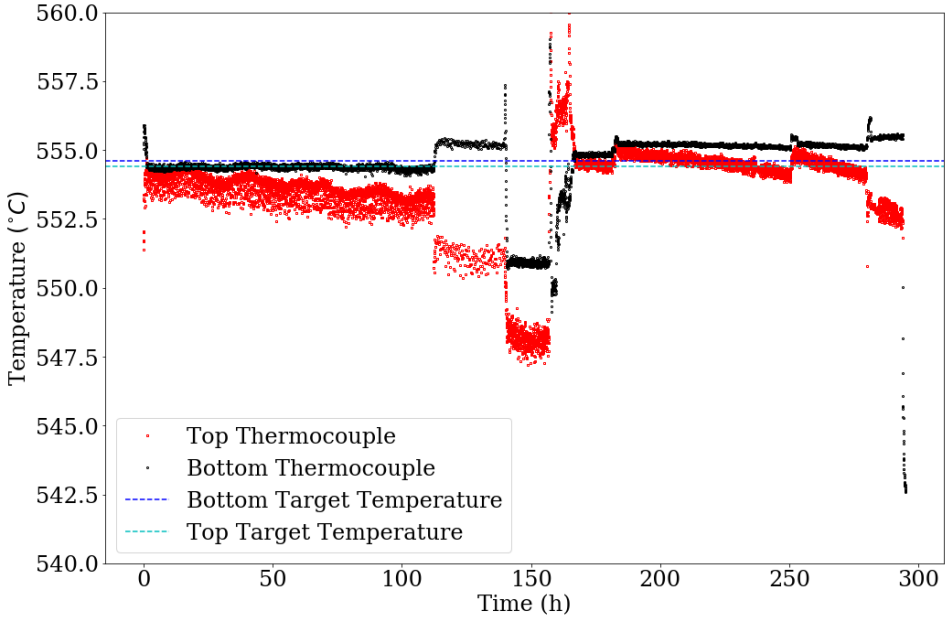

Figure 5.13: Temperature history of Test 2C

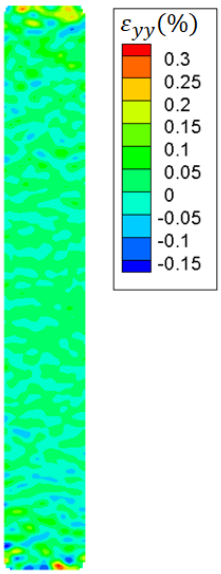

Figure 5.14: Contour plot of longitudinal strains (ϵ_{yy}) as computed between two images of test 2A specimen taken before start of the test and at test temperature. The strain values shown correspond to noise level associated with the DIC data analysis.

4300h and 294h respectively for tests 2A, 2B and 2C.

In the presentation of results, total true longitudinal strains (ϵ_{yy}) are plotted instead of creep strains. This is done to retain the initial plastic strains in the plots. However, for the calculation of tensile properties and creep rates at each material location, the initial loading strains were subtracted from the total strains. In order to derive the creep rates, polynomial fits were made to the creep curves and then the fits were differentiated with respect to time. Minimum creep rates were obtained by taking linear fit gradients over the duration of secondary creep for each material zone (parent, weld and the SAZ) in the specimens. It should be noted here that by "SAZ" a portion of creep strong region near the weld fusion line is meant where the observed creep strains from a test are always lower than the homogeneous parent material. This is different from the heat affected zone (HAZ) of a multi-pass weld and the two may or may not be the same.

5.2.1 Test 2B (σ_{engg} = 250MPa)

Figure 5.15 shows the longitudinal strain (ϵ_{yy}) contours in the gauge section of the specimen at different times from the start of the test. It can be seen that initial strains are insignificant in the weld region, gradually increase in the HAZ/parent (or the SAZ) region as distance from the

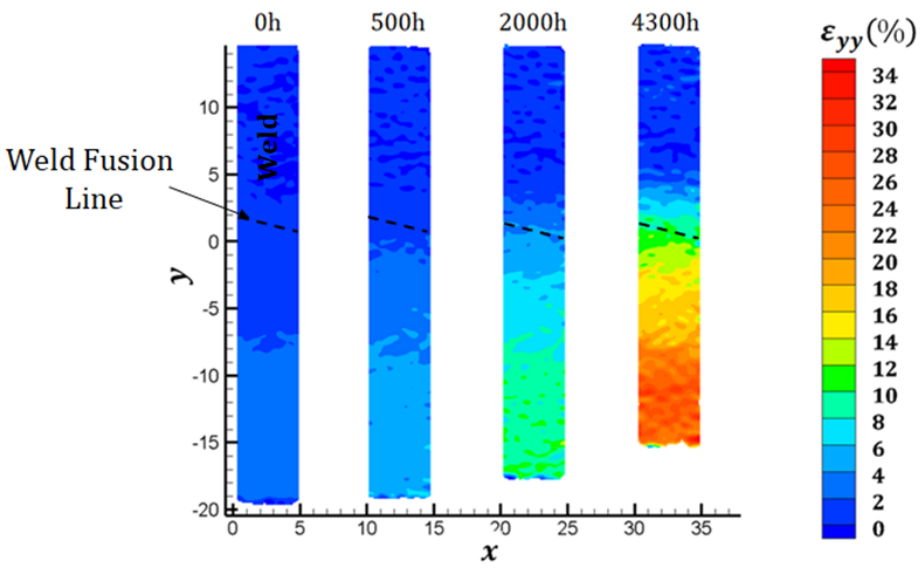

Figure 5.15: Longitudinal strain (ϵ_{yy}) contour plots obtained at different times from test 2B

weld fusion line and finally peak at the parent region at the farthest end. As the test progresses, there is higher and higher accumulation of inelastic strains in the parent whereas the strains in the weld remain comparatively insignificant. A strain gradient exists in the SAZ from the weld fusion line to the far away parent.

Figure 5.16 shows the variation of longitudinal strains ϵ_{yy} along the specimen longitudinal centreline for different times. The strain values are plotted with respect to distance from the weld fusion line (x_w). The variation of ϵ_{yy} in the weld show an undulating pattern. This is a manifestation of weld bead to bead variation of material properties. In the HAZ/parent region adjacent to the weld fusion line, the strain values are similar to the weld and then it gradually increases with distance from the fusion line to a maximum at the parent. As creep strain accumulates, the far away parent region accumulates strains at higher rates than the weld and the SAZ. By observing the strain variation in the SAZ region, an approximate width of the SAZ has been estimated and the SAZ/parent boundary is depicted in the figure 5.16.

Figure 5.17 shows evolution of inelastic strains with time for different material points at varying distances from the weld fusion line. One of the points is in parent, one in the weld and three material points at different locations in the SAZ. The inelastic strain rates gradually increase from the weld through the SAZ and to the parent. It is interesting to notice that the creep rate starts increasing in the parent and near-parent SAZ regions beyond 2000h. This can

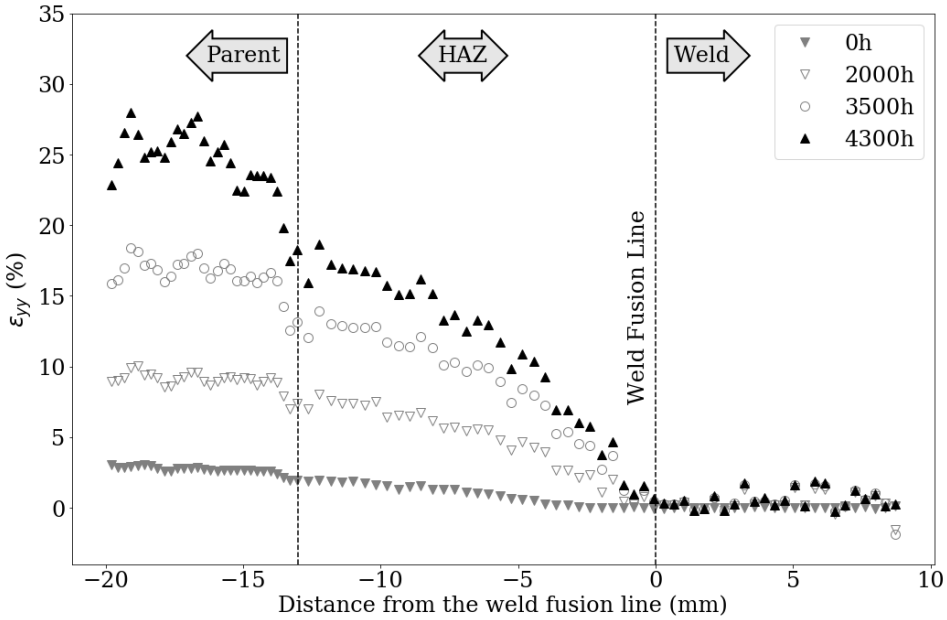

Figure 5.16: Longitudinal strain (ϵ_{yy}) plots along the specimen longitudinal centreline at different times for test 2B

be a mix of both tertiary creep and an increase in true stress due to reduction in area of the specimen. These plots are useful in fitting creep models to different material regions.

In order to approximately work out true stress variation which can be useful in evaluating FE modelling results, an average reduction of area was calculated along the longitudinal centreline for each specimen from the DIC test results. Figure 5.18 shows an area reduction plot along the specimen centreline for test 2B. This plot looks very similar to figure 5.16. The plot also shows that there can be a significant change in true stress at any section in the crossweld with the evolution of creep strains.

5.2.2 Test 2C (σ_{engg} = 300MPa)

Figure 5.19 shows the longitudinal strain (ϵ_{yy}) contours in the gauge section of the specimen at different times from the start of the test. It can be seen that initial strains in the weld are considerably lower than that of the parent. As the test progresses, there is higher and higher accumulation of inelastic strains both in the parent and the weld and somewhere between 100h and 200h, the longitudinal strains in the weld become higher than the parent. It should be noted that there was some divergence in the test temperatures for this test between 120h and 170h. However, barring a very small period of time, temperature variation was maintained within 5°C

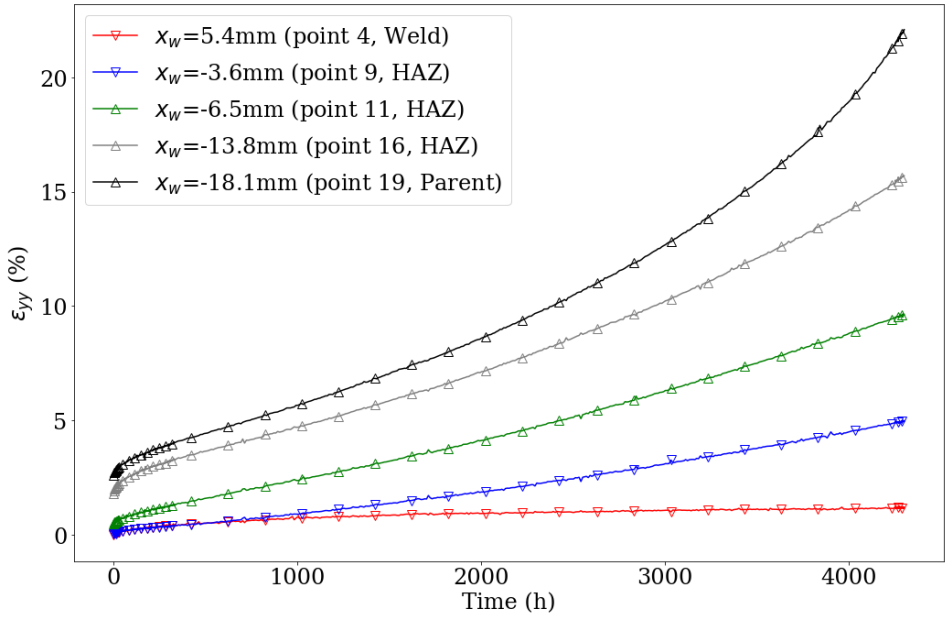

Figure 5.17: Time history plots of longitudinal strains (ϵ_{yy}) at different locations in the test 2B specimen

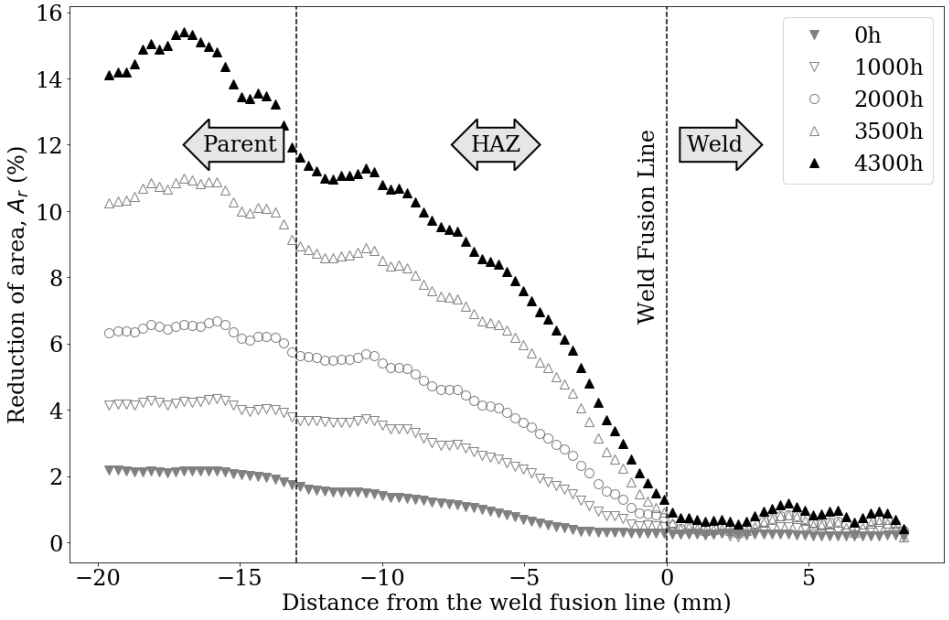

Figure 5.18: Area reduction plots along the specimen longitudinal centreline at different times for test 2B

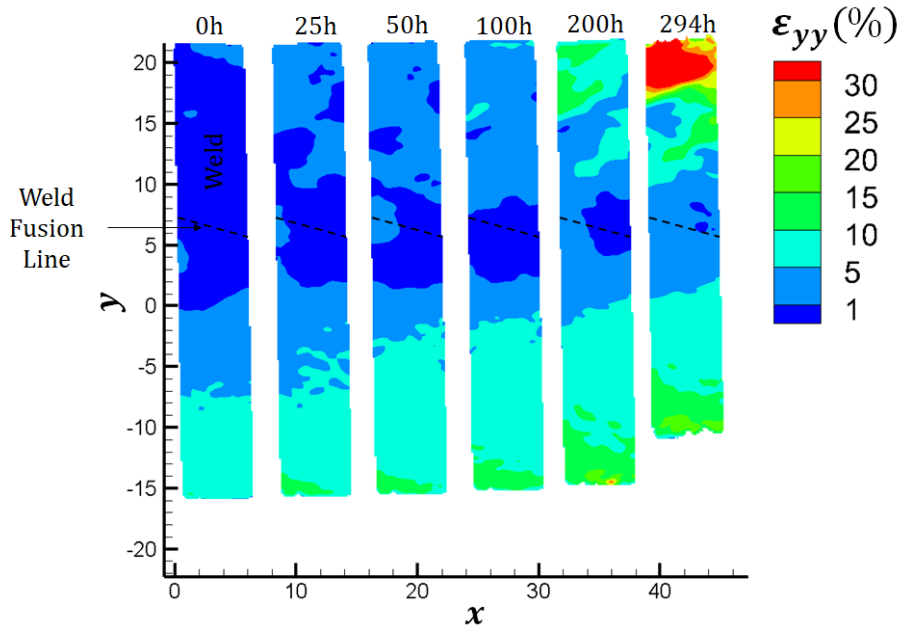

Figure 5.19: Longitudinal strain (ϵ_{yy}) contour plots obtained at different times from test 2C

and corrective action was taken to reset the top and bottom temperatures. It is therefore unlikely that the temperature variation would have caused the strains in the weld to suddenly accelerate and become higher than the parent. It is important to look at all the other results together to be able to confirm if the temperature variation indeed had a significant effect. However, it should be noted that any data extracted from this test for use in the FE modelling is limited to the time before the temperature divergence occurred.

Figure 5.20 shows the variation of ϵ_{yy} along the specimen longitudinal centreline for different times. The strain values are plotted with respect to distance from the weld fusion line. It is interesting to observe the substantial variation of creep strains across different weld beads. Initially, in the SAZ adjacent to the weld fusion line, the strain values are similar to the weld and then it gradually increases with distance from the fusion line to a maximum in the parent. As creep strain accumulates, both the parent and the weld accumulate strains at higher rates whereas strains in a thin zone around the weld boundary does not increase much. In the absence of any other information, it seems like a result of existence of a creep resistant zone of material around the fusion boundary and on the side of the weld which is extremely strong in time independent plasticity as well as creep.

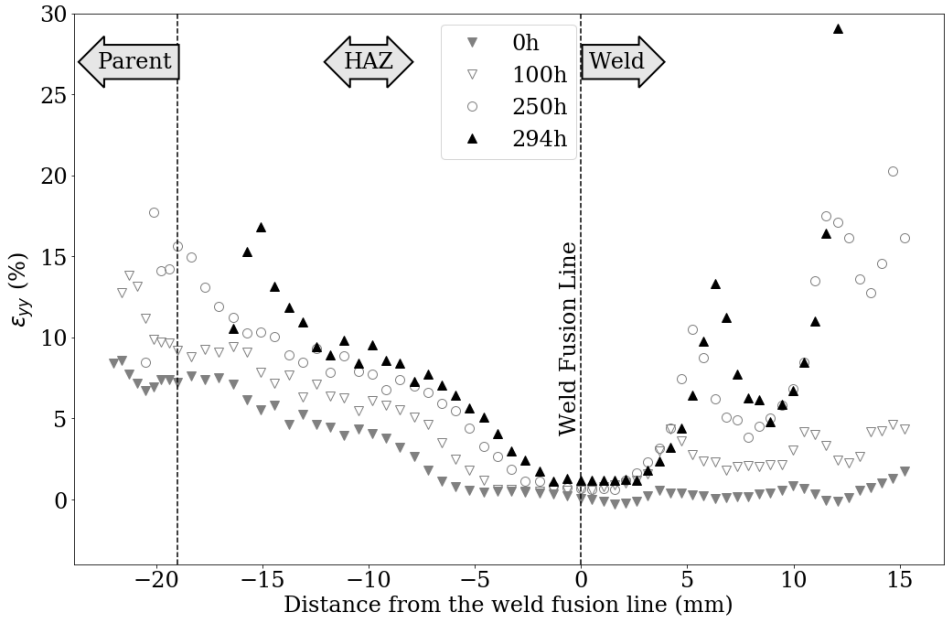

Figure 5.20: Longitudinal strain (ϵ_{yy}) plots along the specimen longitudinal centreline at different times for test 2C

5.2.3 Test 2A (σ_{engg} = 330MPa)

Figure 5.21 shows the longitudinal strain (ϵ_{yy}) contours in the gauge section of the specimen at different times from the start of the test. In this case, a high amount of initial strain can be observed in both the parent and the weld sections whereas the strains in the SAZ remain considerably lower. This is very interesting as the weld should be harder than the SAZ in time independent plasticity. As the test progresses, there is higher and higher accumulation of inelastic strains both in the parent and the weld and somewhere between 10h and 25h, the strains in the weld becomes higher than the parent.

Figure 5.22 shows the variation of ϵ_{yy} along the specimen longitudinal centreline for different times. The strain values are plotted with respect to distance from the weld fusion line. Initially, strains in the parent and the weld are higher compared to the SAZ which shows low levels of strains. As creep strain accumulates, both the parent and the weld accumulate strains at higher rates whereas the strains in the SAZ remain much lower. As the weld accumulates strains at higher rates than the parent, accelerated deformation (which can be a combination of tertiary creep and increase in true stress in the specimen cross section) occurs in the weld before the parent and the failure occurs in the weld.

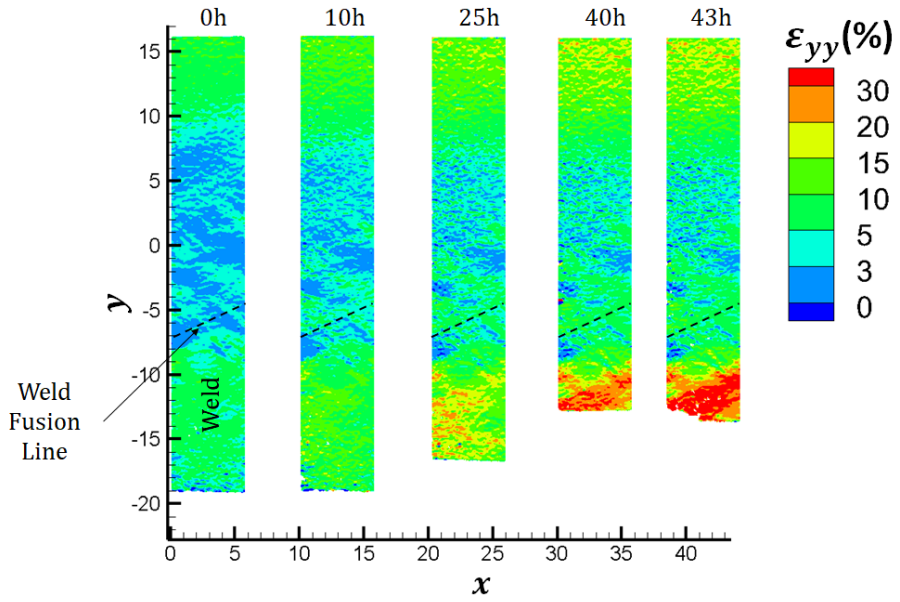

Figure 5.21: Longitudinal strain (ϵ_{yy}) contour plots obtained at different times from test 2A

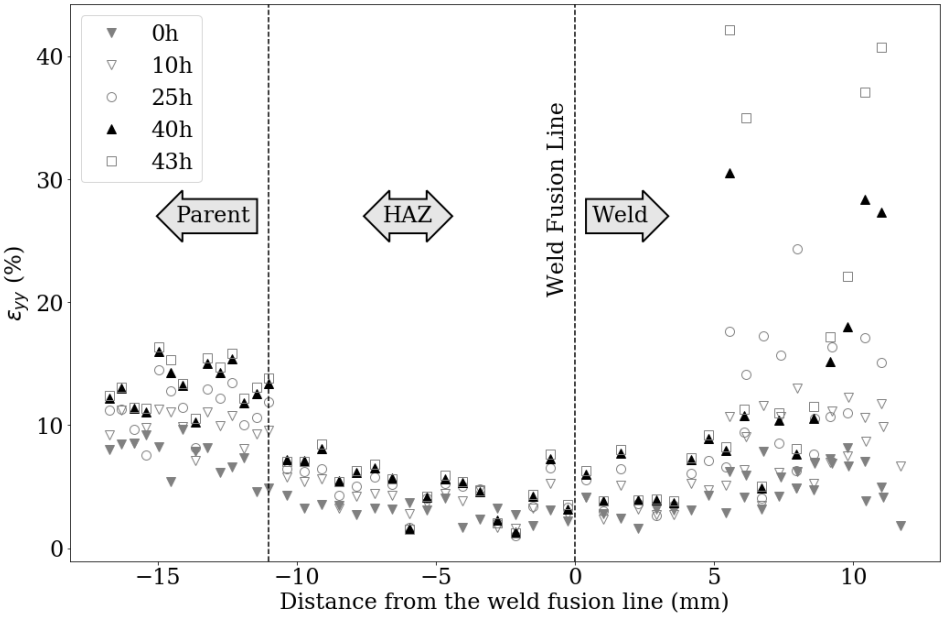

Figure 5.22: Longitudinal strain (ϵ_{yy}) plots along the specimen longitudinal centreline at different times for test 2A

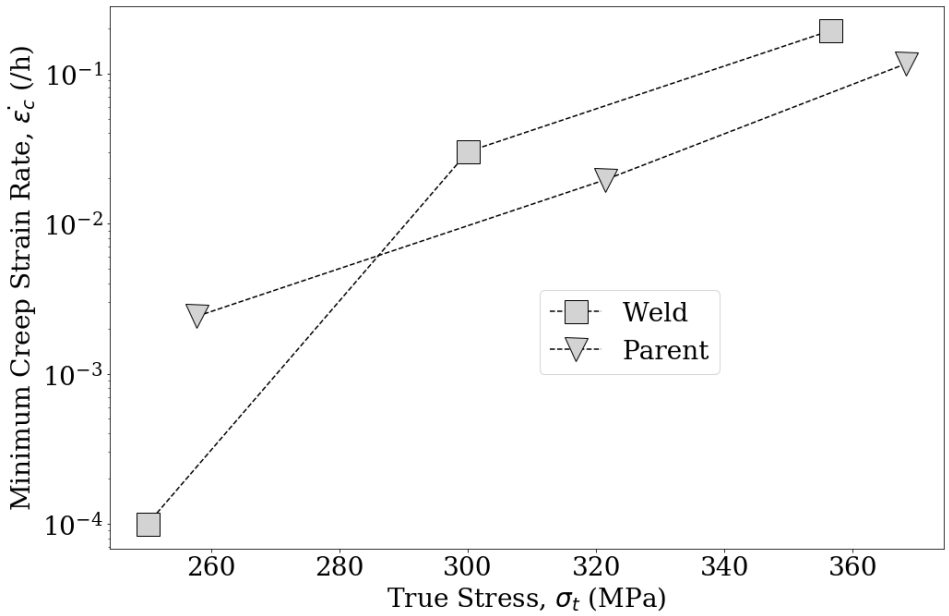

Figure 5.23: Plot of minimum creep rate versus applied stress for the parent and the weld sections derived from the DIC creep tests

Figure 5.23 shows a plot of minimum creep strain rates versus applied stress for both the parent and the weld material as calculated from the DIC creep test data. Here, estimated true stress values have been used as there is significant initial plasticity at such high applied stress levels. It can be seen that at 250MPa, the minimum creep strain rate in the weld is lower than that of the parent 316H material. However, somewhere between 250MPa and 300MPa, the strain rate in the weld becomes higher than the parent. This indicates that the dependency of creep strain rate on applied stress is higher in the weld than the parent. This is an important factor to consider for interpreting crossweld creep test data. Also, it can be seen from the plot that since the weld incurs lower initial plastic strains than the parent, the true stress values for the weld are lower than that of the parent for the same applied stress.

The above results indicate that although the weld is considerably stronger in creep than the parent at lower stresses, it becomes softer than the parent at higher stresses. This indicates that the stress dependency (secondary creep stress exponent) of creep is higher in the weld than the parent. Also, it was interesting to see that for an applied stress of 330MPa, there is considerable inelastic strains in the weld. This indicates that although the initial yield strength of the weld is considerably higher than the parent material, the stress strain curve of the weld becomes flatter at high plastic strains.

5.3 Finite Element Modelling

In order to estimate the effect of creep mismatch on the distributions of creep strains and true stresses in the specimens, finite element models were developed to match the logarithmic strain distributions from the tests for the overall gauge area of the test specimens. The FE models were then used to investigate the evolution of true equivalent stresses in the gauge area during creep.

As the specimens were adequately thin (2mm - 2.5mm), a 2D plane stress formulation was used for the models. For specimens 2A and 2C, only half of the specimens had to be modelled taking advantage of the symmetry as the welds were located at the centre of teh gauge sections. For test 2B, the whole specimen had to be modelled. Figure 5.24 shows a schematic of the specimen geometries along with the loading and applied boundary conditions. Specimen 2B was hinged at both the ends which closely simulated the actual test boundary conditions. A control point was defined each at the specimen holes and connected to the periphery of the respective holes using a kinematic coupling. The rotation degree of freedom was not coupled. The bottom hinge was fixed while a concentrated load was applied to the top one equivalent to the load applied at the respective creep test. Specimens 2A and 2C used the symmetry condition at the centre of the weld and only half of the geometry was defined. A control point was defined at the top specimen holes and the respective hole periphery was connected to it using kinematic coupling. Rotation degree of freedom was not coupled. A point load was applied to the top control points for specimens 2A and 2C.

Full integration plane stress quadratic elements (CPS8) were used for all the FE models. The reason for using full integration quadratic elements was to enable the use of singular quarter node elements at the free edges of the weld interface in the models. Mesh sensitivity analyses were performed using simple and single material elastic-plastic properties and a sufficiently refined mesh was derived for each of the models. Figure 5.25 shows the FE mesh for model 2B. Singularity elements were used near the edges of the weld interface as shown in the figure. Figure 5.26 shows the FE mesh for the 2A and 2C FE models.

Material properties for the FE models had to be carefully chosen in order to simulate the actual cast of the 316H steel used in the test material. Both the elastic-plastic as well as the creep deformation properties were taken from conventional tests done on the same cast of parent 316H and on HAZ/parent samples taken from the same weld described in section 4.1.1 of chapter 4. Figure 4.3 depicts the true stress-strain response of Cast 69431 316H test weldment and

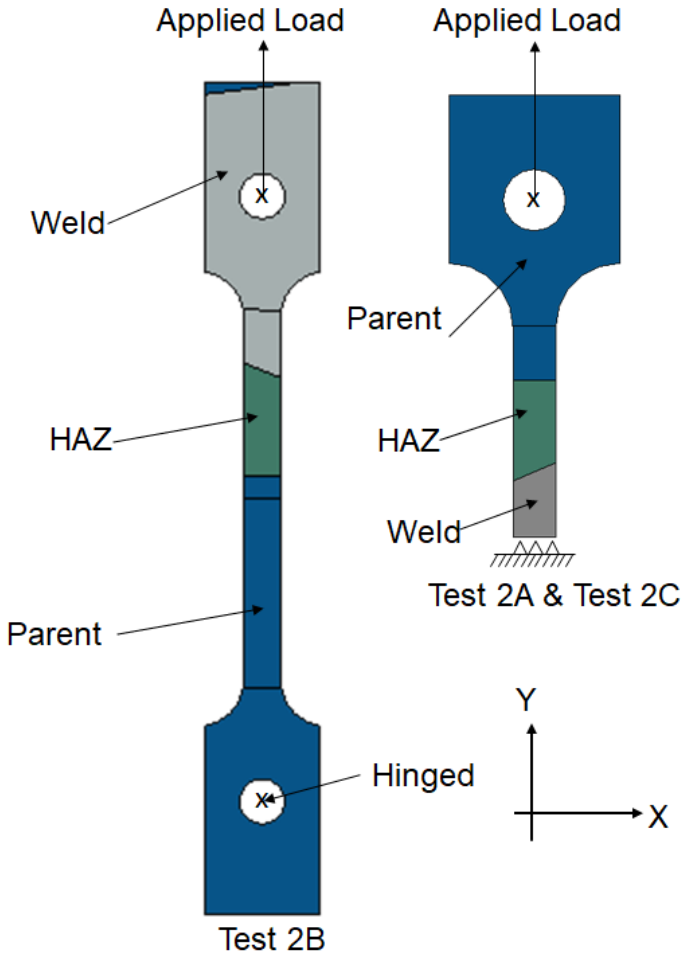

Figure 5.24: Schematic of the FE models showing the geometry and loading conditions

figures 4.4 and 4.5 present it's creep response at 550°C. In order to compare the FE modelling results to the DIC tests, it was important to match the material properties of the crossweld specimens as closely as possible. Since the DIC creep tests were performed at high stress levels (>250MPa), a close approximation of the elastic-plastic stress-strain curve for the material models was necessary. In the FE models, three material zones were used: parent, SAZ and the weld. For the parent and the SAZ, data was available from the conventional tests. Since welds are highly heterogeneous and varied from weld to weld, publishing weld data in as-welded condition is practically impossible. Therefore, for the weld section of the FE models, a fitted elastic-plastic and creep model were used from the DIC creep tests. This should not effect the independence of the FE models as the main goal is to examine the creep mismatch effects in the SAZ and the parent sections of the models. Since the weld strains varied significantly along the weld length in the

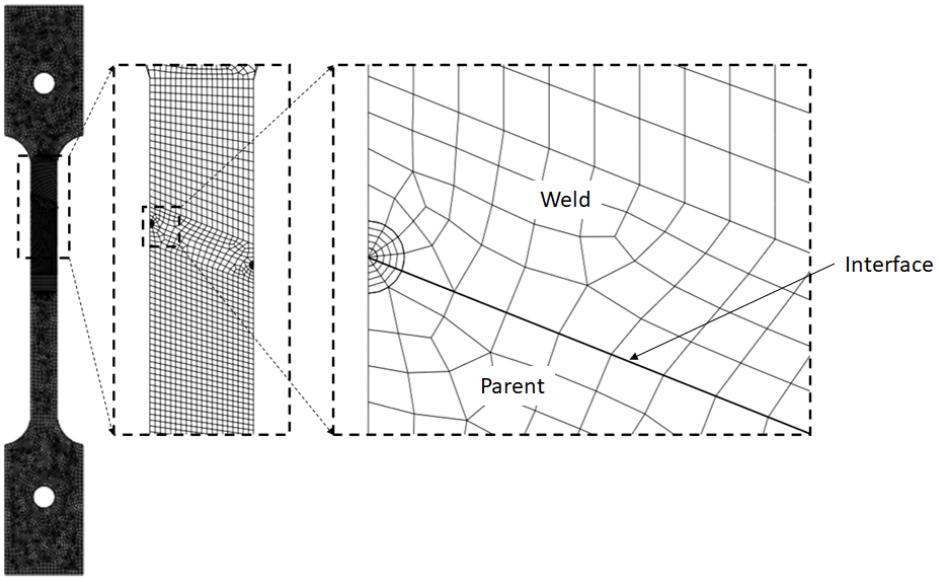

Figure 5.25: Schematic of the FE models showing the geometry and loading conditions

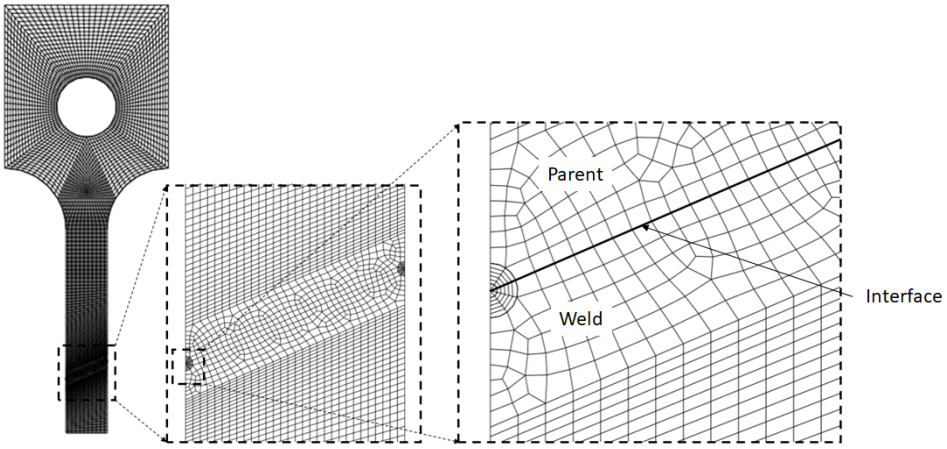

Figure 5.26: Schematic of the FE models showing the geometry and loading conditions

DIC test specimens, all weld data for the material fits were extracted from a zone around 5-10mm away from the welded interface so that the mismatch between weld and SAZ across the weld interface (if any) is retained. Regression fits obtained from the conventional tests (parent and SAZ) were compared to the data obtained from the DIC creep tests (parent and weld). Figure 5.27 shows the fit comparisons of stress strain curves between conventional creep tests and the DIC creep tests for the same cast. Table 5.4 lists down the yield strengths and plastic strains for the parent and the weld material as obtained from the fits. The end points of the stress-strain curves were obtained by extrapolation and hence highlighted. A Norton-Bailey creep model (equation 2.4) was fitted for primary and secondary creep for the parent material. The accuracy of the creep model fits can be qualitatively assessed from figure 5.28. In this figure 5.28, the fitted creep strain evolution with time, as obtained from the regression model is compared against actual data from the conventional creep tests. The plots show considerable matching. Table 5.5 presents the primary and secondary creep deformation parameters used for the following strain hardening multi-axial formulation of the Norton-Bailey creep equations (reproduced from equations 2.20 of chapter 2):

$$(\dot{\epsilon}^c_{ij})_{primary} = \frac{3}{2}\sigma'_{ij} C_1^{\frac{1}{C_2}} C_2 (\epsilon^c_e)^{\frac{C_2-1}{C_2}} {\sigma_e}^{(\frac{n_1}{C_2}-1)}, \tag{5.1a}$$

$$(\dot{\epsilon}^c_{ij})_{secondary} = \frac{3}{2}\sigma'_{ij} C {\sigma_e}^{n-1}, \tag{5.1b}$$

$$\dot{\epsilon}^c_{ij} = Max((\dot{\epsilon}^c_{ij})_{primary}, (\dot{\epsilon}^c_{ij})_{secondary}) \tag{5.1c}$$

$$\dot{\epsilon}^c_e = \sqrt{(\frac{1}{2}\dot{\epsilon}^c_{ij}\dot{\epsilon}^c_{ij})} \tag{5.1d}$$

where, i and j are the coordinate indices, $(\dot{\epsilon}^c_{ij})_{primary}$ are the primary creep rate components, $(\dot{\epsilon}^c_{ij})_{secondary}$ are the secondary creep rate components, $\dot{\epsilon}^c_{ij}$ are the effective creep strain rate components, σ'_{ij} are the stress deviatoric tensor components, ϵ^c_e is the equivalent creep strain and σ_e is the equivalent von Mises stress while C_1, C_2 and n_1 are primary creep constants and C and n are secondary creep constants. A detailed discussion on this creep model is made in literature survey (Chapter 2).

The elastic-plastic as well as creep deformation properties for the SAZ section were not separately modelled. It was assumed that plastic hardening in the SAZ would see a gradual

Parent		Weld	
Yield Strength, σ_Y (MPa)	Plastic Strain, ϵ_p	Yield Strength, σ_Y (MPa)	Plastic Strain, ϵ_p
157.44	0	-	-
265.84	0.03	280	0
313.32	0.05	300	0.00076
533.17	0.25	356	0.043
698.10	0.40	423.45	0.097

Table 5.4: Stress-strain data used in the FE models for the weld and the parent material sections

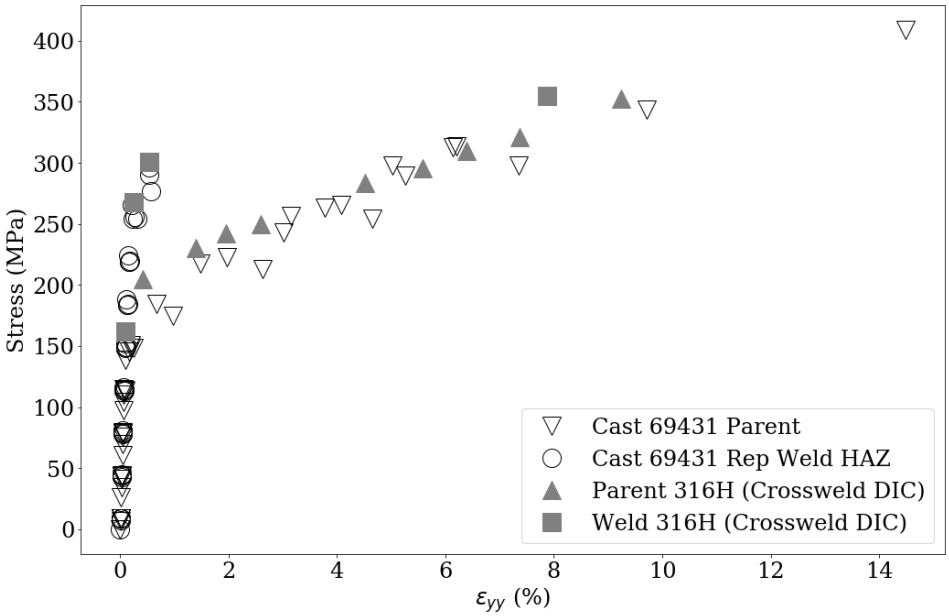

Figure 5.27: Stress strain curves of Cast 69431 REP weld

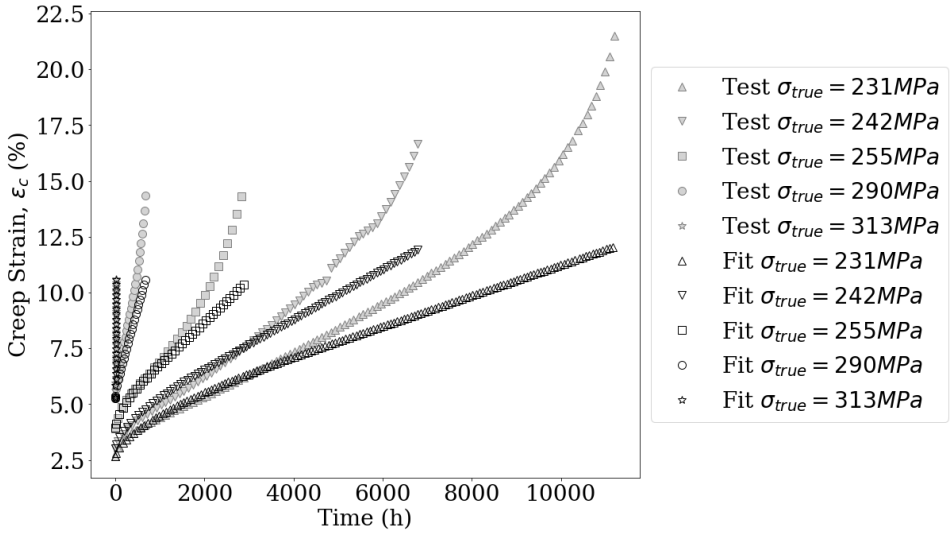

Figure 5.28: Creep model comparison with actual creep data for 316H Parent

Material	C1	C2	n1	C	n
Parent/ SAZ	2.9618D-12	0.42131	4.18	3.99025E-22	6.961
Weld	1.12131E-10	0.633182331	3.482723323	6.76083E-58	21.4

Table 5.5: Creep constants from data fits for the parent and the weld

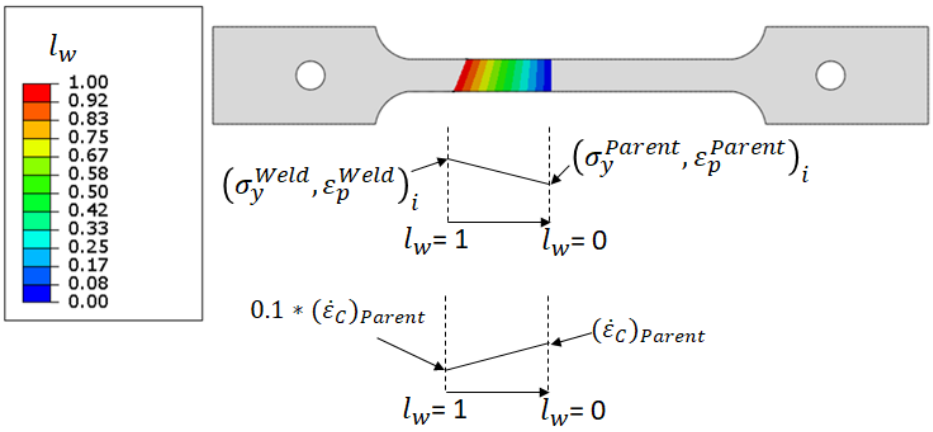

Figure 5.29: Test 2B FE model showing the variation of the state variable l_w and schematic variation of stress-strain and creep properties across the SAZ. The subscript 'i' indicates a point on the material stress-strain curve as presented in table 5.4

variation from the weld to the parent section. Therefore, a linear variation of plastic hardening was assumed between the weld and the parent in the FE models. Also, the DIC creep tests showed that a thin region around the weld interface displays extremely high strength in both time independent plasticity and creep. Therefore, for creep, it was assumed that the creep rates in the SAZ would linearly vary between 0.1 times the parent creep rate at the weld boundary to that of the parent at the other end. This partly follows from the local creep tests done in the previous chapter which showed that the minimum creep rates in the SAZ were lower than the parent but within an order of magnitude. In order to implement gradual variation of both creep as well as plastic hardening in the SAZ, a state variable (l_w) was defined using a USERFLD subroutine in ABAQUS 6.14 (ABAQUS 6.14 Documentation [132]). Figure 5.29 shows how l_w varied in the SAZ in the FE model and how the plastic hardening and creep rates varied as a function of l_w. The length of the SAZ section was kept at 12mm as was approximately observed from the DIC creep tests.

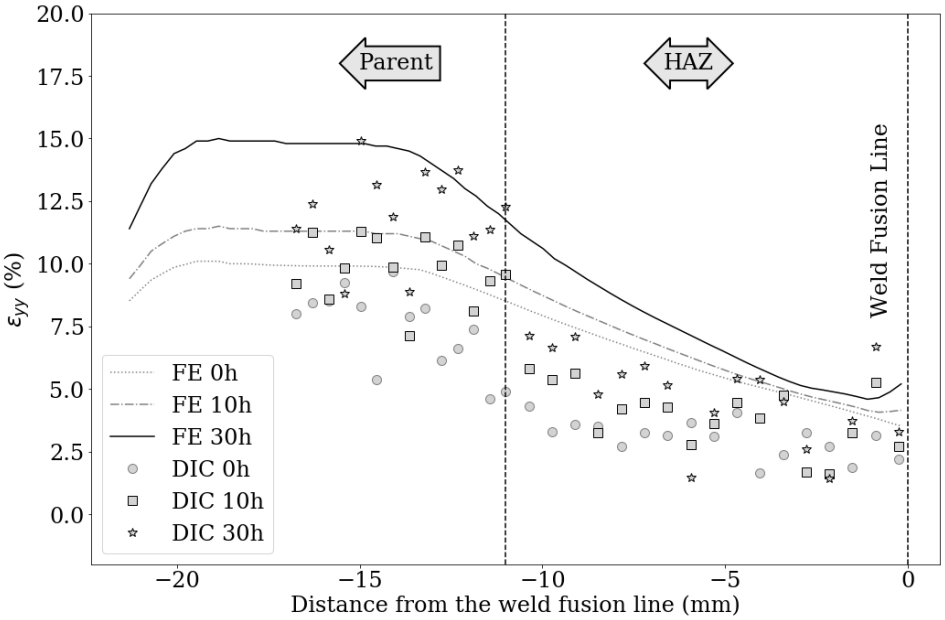

Figure 5.30: Comparison of longitudinal strain (ϵ_{yy}) evolution with time between DIC creep test and FE model of specimen 2A

5.3.1 FE Model Results

FE results from only models 2B and 2CA are presented here as these are the two bounding applied stress cases. During analysis, it was observed that reduction of area had a significant effect in a gradual increase of true stress for each analysis case. For comparison with DIC creep test results, longitudinal logarithmic strain (ϵ_{yy}) values were plotted along the longitudinal centreline of each specimen from the FE analyses.

Figure 5.30 and figure 5.31 show the comparison of longitudinal strain evolution obtained from FE analysis for specimens 2A and 2B respectively against data obtained from the DIC creep tests. The results for the weld material has been deliberately omitted as the main regions of interest are the parent and the SAZ sections.

Figure 5.30 shows good correspondence of FE results with the corresponding DIC creep tests. However, the FE over predicts the strain evolution in the SAZ and the parent sections. In the SAZ section, the trends match well. A better correspondence can be derived by additional creep tests and a more complex modelling of the SAZ region.

FE results for specimen 2B shows better correspondence with the DIC creep tests (figure 5.31) compared to specimen 2A results. However, there is a slight bulge in the strain values near

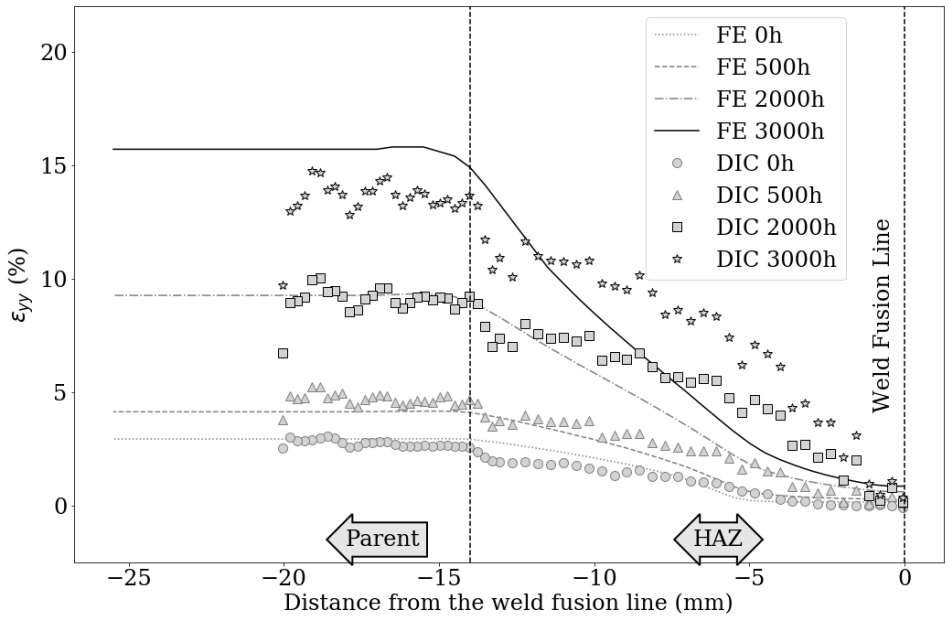

Figure 5.31: Comparison of longitudinal strain (ϵ_{yy}) evolution with time between DIC creep test and FE model of specimen 2B

the weld fusion line from the tests at 2000h and 3000h which is not captured in the modelling. This also may be due to non-linear variation of mechanical properties through the SAZ in the test material.

As an additional level of checks, strain evolution with time during creep were compared for different material points in the parent and the SAZ between the FE results and the tests. Figures 5.32, 5.33 show the longitudinal strain evolution with time for 2A and 2B respectively. It can be seen that for test 2A, there is slight over prediction of strains by the FE model for the parent material and a considerable over prediction for the SAZ. For test 2B, there is excellent matching between the FE and the test results. It should be noted that during creep tests at such high stress levels, due to the presence of considerable initial strains in the specimens, the true stresses keep varying through the creep tests. Therefore, the creep strain rates in the specimens never truly become constant and there is always a gradual increase after primary creep. This impacts the creep model fits and thereby the FE model results.

As mentioned earlier, an FE model which is benchmarked with respect to DIC creep test results is useful as it can be used to derive full field true stress information in the region of interest. Using the FE model 2B, contour plots of true stress at different times were derived to illustrate significant variation of true stress throughout a creep test performed at high stress

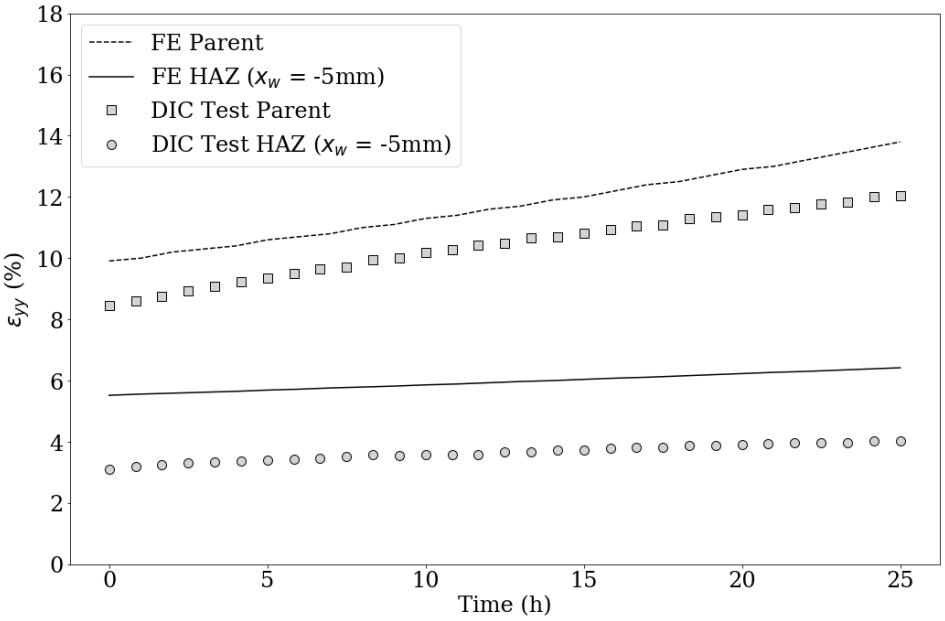

Figure 5.32: Plot of longitudinal strain (ϵ_{yy}) versus time for different material points for test 2A and the corresponding FE model

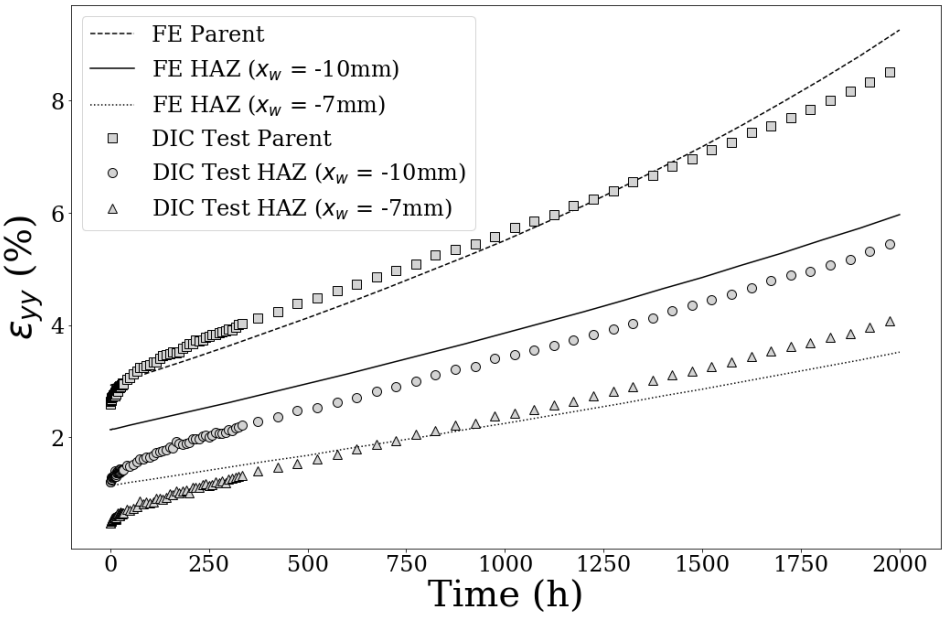

Figure 5.33: Plot of longitudinal strain (ϵ_{yy}) versus time for different material points for test 2B and the corresponding FE model

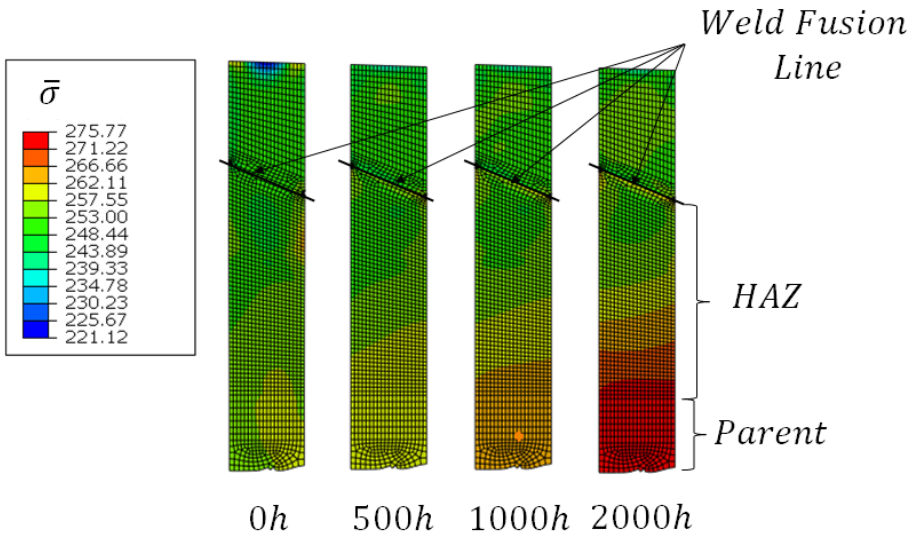

Figure 5.34: Contour plot of true von Mises equivalent stress (σ_e) at different times for FE model 2B

levels. Figure 5.34 shows contour plots of true von Mises equivalent stress at different times for test 2B. It can be seen that the true stress in the parent at the start of the test was approximately 257MPa when the applied stress was 250MPa. At 2000h, the maximum true stress in the parent increases to around 275MPa. This shows that any creep model fits to creep test data for high stress values will have an inherent inaccuracy owing to the true stress not being constant in the test specimen during the creep test. It should be noted that generally creep tests are performed at very high stresses compared to the actual stress levels a component is expected to see during plant operation. Therefore, care should be taken in interpreting creep test data.

5.4 Conclusions

A number of important conclusions were derived from this piece of work as discussed in the following paragraphs.

It was demonstrated that DIC creep tests can be useful in testing crossweld samples where there is a variation of mechanical properties and an associated strain variation in the test specimen. A DIC creep test gives full field strain information and thus variation of mechanical properties in a crossweld sample can be accurately captured.

It was shown that results from a DIC creep test on a crossweld can be used to build and

benchmark finite element models which can incorporate mechanical property variations for a test material more realistically. It is difficult to estimate for example, the extent of a creep strong region or the length through which there can be a gradual variation of mechanical and/ or creep properties in a crosswweld sample. DIC creep tests give a good idea of the extent of that region which can then be incorporated in an FE model. In this work, the observed extent of a creep strong region was smaller than the SAZ of the weld which should extend to more than twice the length of this creep strong region. As has been observed, the variation of creep rates in this region is smaller than an order of magnitude but the observed variation in creep strains is largely due to variation in mechanical hardening.

It was shown that using an FE model benchmarked against the full field strain information derived from a crossweld DIC creep test, the variation and evolution of true stress in the specimen during the creep test can be estimated. This is very useful as creep tests are generally conducted at high levels of applied stress which results in a lot of initial plasticity in the specimens. As creep strains accumulate with time, there is significant change in the cross-section of the specimens leading to a continuous change in true stress at any given point in the specimens accompanied by change in creep strain rates. An accurate estimate of true stress distributions and evolution in the specimen is important in determining creep properties such as the minimum creep strain rate for a given material section. Also, this can be extremely useful in benchmarking creep damage models. True stress information can help in distinguishing increase in creep strains due to tertiary creep from increase in time independent plastic strains due to a reduction in specimen cross-section.

From the DIC creep test data, a higher secondary creep stress exponent was estimated for the weld material than the parent 316H steel. The combination of a high stress exponent for the weld metal, the creep coefficients and the stress levels used for the tests explains why the weld material strains at a lower rate than the parent at comparatively lower values of applied stress but at higher values of applied stress, the behaviour is reversed and the weld enters tertiary creep before the parent and eventually fails. A stress value was estimated by interpolation at which the weld creep rate overtakes that of the parent. Although weld properties are in general highly heterogeneous and are not the main focus of the present work, knowledge of this behaviour is important in a) fixing test stress levels and b) interpreting test data.

The tests showed the presence of a creep resistant zone of a few millimetres around the weld

fusion boundary which displayed stronger elastic-plastic as well as creep deformation properties than the parent or the weld material. The inelastic strains in the zone remained insignificant compared to the weld and the parent throughout the tests.

The tests did not show any significant effect of strain mismatch between the parent and the weld near the weld fusion boundary. It may be argued that such an effect will be minimal for such thin specimens as used in the tests. However, the tests showed that there was no jump in the longitudinal strains across the weld boundary and the variation was gradual. In view of this, it is unlikely that there will be any noticeable constraint effect across such an abrupt weld interface. In future, these tests can be repeated for square section specimens or the benchmarked FE models from these tests can be used in order to study any constraint effects due to material mismatch across the weld fusion zone.

CHAPTER 6

EFFECT OF A SIMULATED WELD CAP ON CREEP OF AN EX-SERVICE 316H WELD

> *"It doesn't matter how beautiful your theory is, it doesn't matter how smart you are. If it doesn't agree with experiment, it's wrong."*
>
> Richard P. Feynman

Stress and strain concentrations exist in butt welds due to various geometrical factors such as misalignment, thickness transition and presence of a weld cap (Pluvinage [173], Perovic [174], Zachary and Burger [175]). Extensive analytical and experimental work was done in the past on deriving stress concentration factors in butt welds arising out of the geometry of the weld, most notable of which are (Lotsberg [176], Smedley et al [177]). Lotsberg [176] used finite element simulations for deriving stress concentration factors arising out of misalignment in butt welds and Stevick and Finnie [178] derived stress concentration factors for longitudinal butt welds at elevated temperatures. A single material model was invariably used for all the cases and any augmentation effect on stress concentration due to material mismatch was ignored. In chapter 5, it was observed that in a crossweld creep test specimen of an ex-service 316H multi-pass weld that there is insignificant strain localisation or stress concentration at the

edge of the weld fusion line due to material mismatch. However, the level of initial plastic strains in the specimens along with a variation of creep and plastic properties in the different zones of the weld affected the overall creep response of the specimens. An investigation of the combined effect of material mismatch as well as weld geometry on the stress and strain distributions in a crossweld specimen can lead to a more realistic estimation of stress and strain concentrations.

The aim of this work is to study the augmenting effect of material mismatch on the stress and strain concentrations in a crossweld specimen with a simulated (fabricated) weld cap. An artificial weld cap was fabricated in a crossweld specimen using wire electro discharge machining (EDM) and DIC creep test was carried out in order to derive full field strain distribution in the gauge section of the specimen, especially at the root of the weld cap. An FE model was then benchmarked to the DIC test which was then used to carry out a comparison of the stress and strain profiles along a specimen ligament for a single and a multi-material model.

6.1 DIC Creep Test

A DIC creep test was performed on a crossweld specimen with a simulated weld cap. The test was performed at an applied load of 3.606 kN and at a test temperature of 550°C. An applied load of 3.604 kN ensured an applied stress of 300 MPa in the far away HAZ of the specimen which had a cross section of 6.01mm x 2mm. The same test set up, as discussed in chapter 5 was used for the test. The crossweld specimen was extracted from the same material block as described in Chapter 5. Figure 6.1 shows the drawing for the capped crossweld specimen and the location of the weld. It should be noted here that owing to the small length of the specimen, the material outside the weld within the specimen gauge area will be HAZ/parent.

For the DIC creep test, at first a load cell was used to calibrate the dead weight loading corresponding to the test load of 3.606 kN. Since dead weight blocks were used, the actual applied load was 3.604 kN which would induce an applied stress of 299.85MPa in the thin section of the specimen. Two N-type thermocouples were used for the test. The thermocouples were calibrated against a master thermocouple at 550°C. Figure 6.4 shows a plot of the thermocouple temperatures against the respective target calibration temperatures. One thermocouple was attached to the top and another at the bottom of the specimen by wires and it was ensured that the tip of each thermocouple tightly remained in contact with the specimen face. Two small holes were drilled on the specimen to hold the thermocouples. The specimen was then attached to the

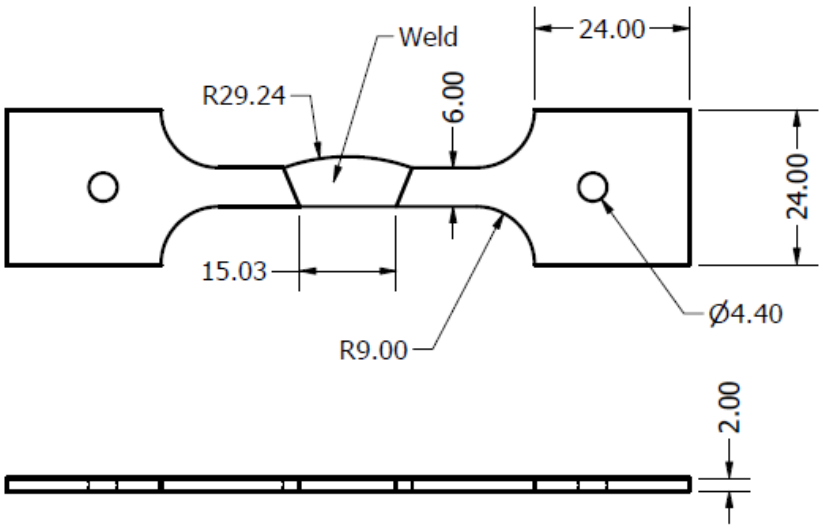

Figure 6.1: Capped crossweld specimen for DIC creep test

machine using specialised grips and the furnace was adjusted to position it between the specimen grips with the specimen gauge area clearly visible through the furnace window. The furnace was then closed and the camera was focussed on the gauge area for image checks. After the specimen, furnace and the camera were installed in place, the furnace was heated overnight and gradually to the test temperature. After approximately 15h of thermal soaking, a reference image of the specimen was taken at the test temperature with 0 load (a small load of 5N was used to stabilise the load chain which is neglected here). The specimen was then loaded up slowly to the test load.

The images obtained for the test specimen speckle patterns was converted to an 8-bit image and the corresponding histogram has been plotted in figure 6.2. It can be seen that the image has sufficient contrast for the DIC test. The histogram lies mainly on the darker side.

Figure 6.3 shows the size of the speckle pattern for the capped crossweld specimen. As can be observed, the speckle size is not small enough to perform an accurate estimate of strain localisation. However, since the focus of the work is to benchmark FE models to the DIC test results for the global strain field in the specimen gauge section, this speckle size will be sufficient.

Figure 6.4 shows the temperature history of the DIC creep test. It can be seen that the temperatures in the top and bottom thermocouples remained close to the target temperatures for up to approximately 450h after which both the temperatures fall by about $1.5°C$. Therefore,

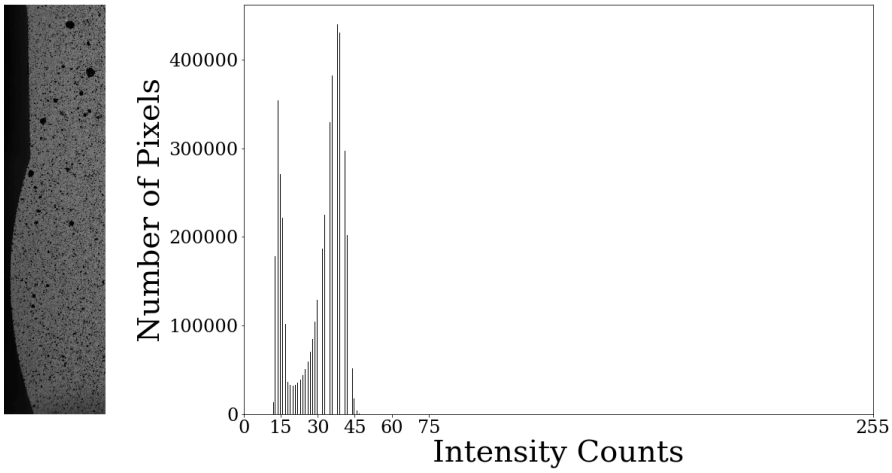

Figure 6.2: Capped crossweld specimen image histogram

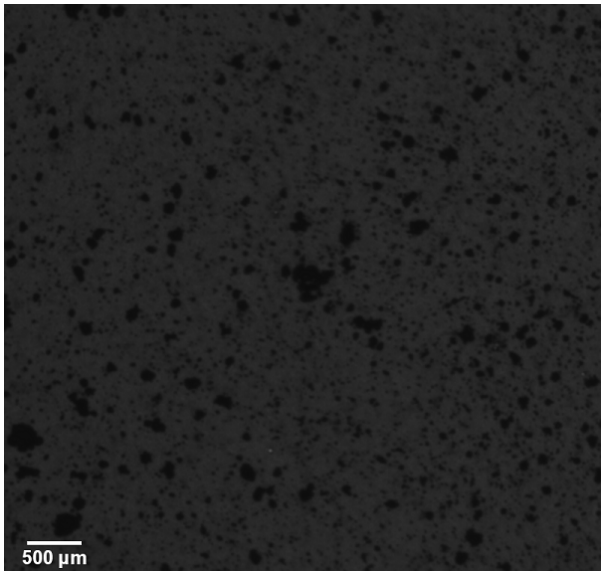

Figure 6.3: Capped crossweld specimen speckle pattern

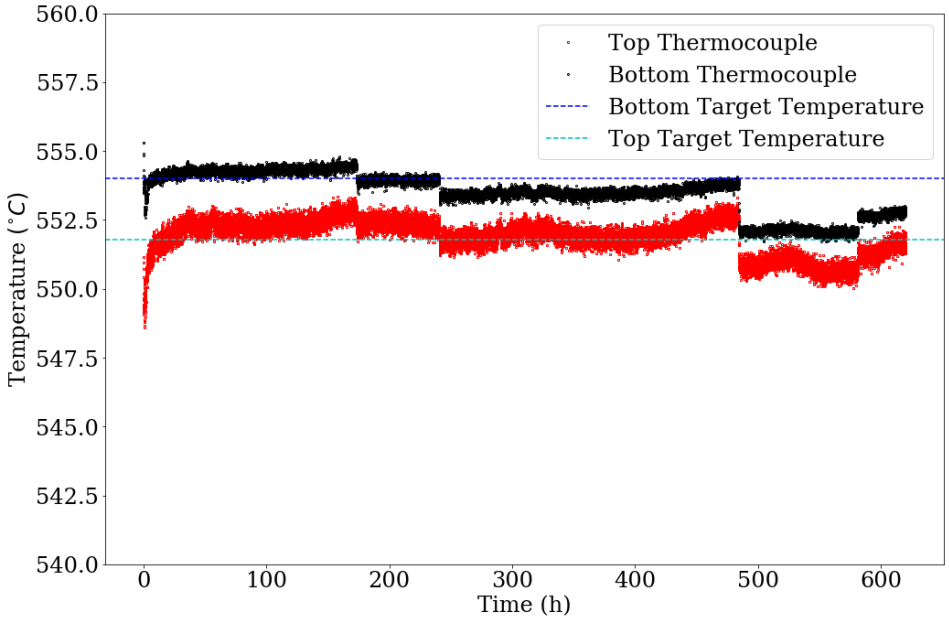

Figure 6.4: Plot of temperatures recorded by the thermocouples and target temperatures of each versus time

it will be assumed that test data up to 450h obtained from this test is reliable. Since the focus of the test is limited to secondary creep in the thinner gauge section of the specimen, the data obtained from the test will be useful.

6.2 Test Results

The test ran for a total of 620h before the test was interrupted due to a power failure in the lab. However, as pointed out in the previous section, there was a dip in the thermocouple temperatures after about 450h of creep time. Test data obtained up to 400h was analysed and used in this work.

In this work, plastic strains during creep were separated from the initial plastic strains upon specimen loading in presenting and analysing results. Figure 6.5 shows a contour plot of initial plastic strains in the specimen after loading was complete. Considerable variation of strains can be noticed which can be due to the bending moment generated in the asymmetric specimen or a variation in material properties or a combination of both. Although there is not much strain concentration at the top edge of the weld cap, there is significant strain localisation in the bottom corner of the weld cap. The higher of the two will be considered while comparing with FE results in the next section.

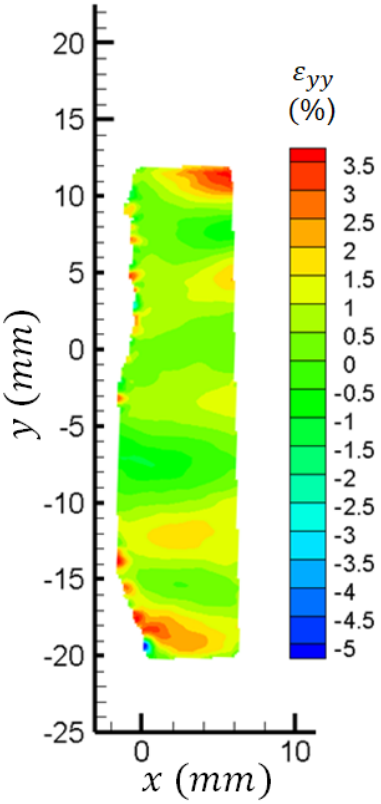

Figure 6.5: Contour of elastic-plastic initial loading strains

A contour plot of evolution of longitudinal strains during creep is plotted in figure 6.6. The longitudinal strains plotted here are the net strains during creep deformation which were derived by subtracting the initial longitudinal strains at the start of creep from total longitudinal strains at any given point of time ($(\epsilon_{yy})^{creep}$). It can be seen from figure 6.6 that a strain concentration is developed at the edges of the weld cap on the HAZ/parent side of the specimen.

Creep strains were plotted across the width of the specimen at different distances (x_w = $2.63mm, 5.96mm, 9.35mm$) from the wedge of the weld cap and at different creep times. Figure 6.7 shows that there is a significant bending moment near the weld ($x_w = 2.63mm$) with the strains going from positive from the left edge to slightly negative on the right. As we move away from the weld (figures 6.7 and 6.8), the strain profiles flatten indicating a more uniform stress acting across the width of the specimen.

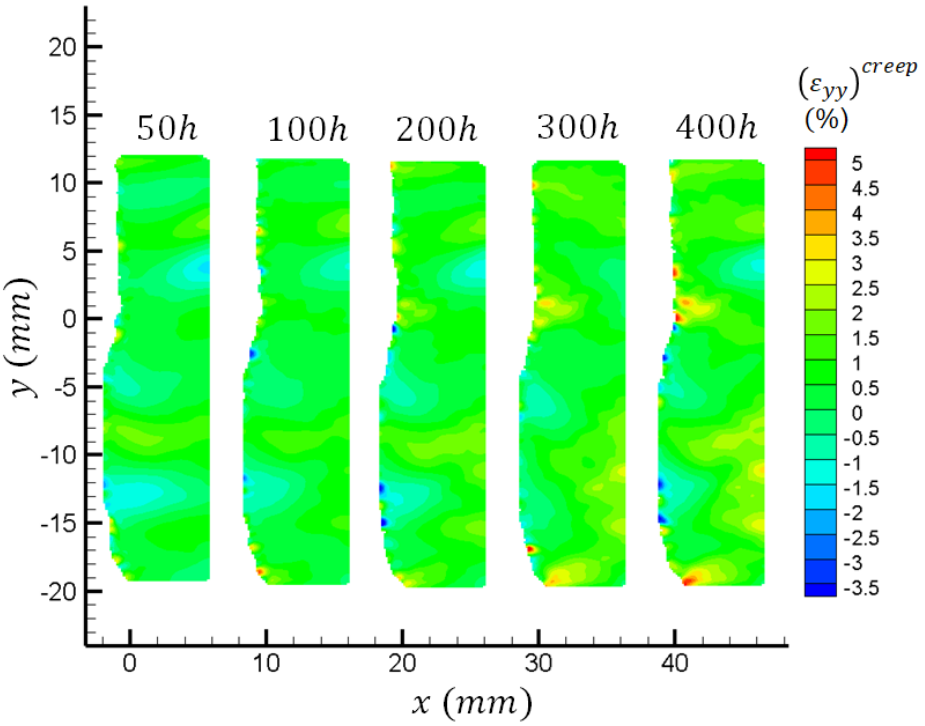

Figure 6.6: Contour of elastic-plastic strains accumulated during creep at different creep times

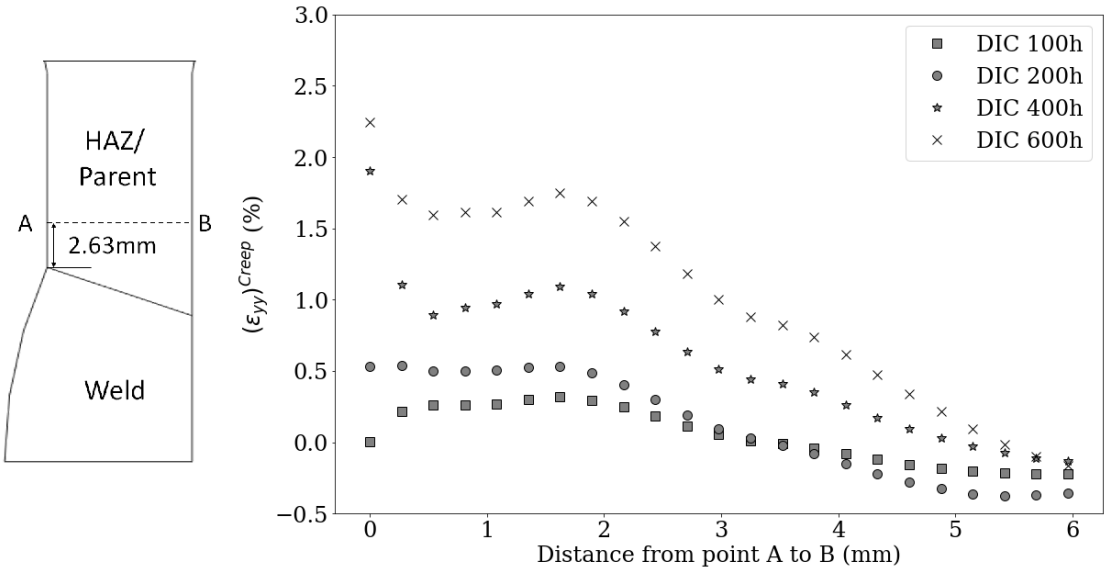

Figure 6.7: Plot of creep strains versus distance for a horizontal line in the specimen for x_w = 2.63mm for different creep times

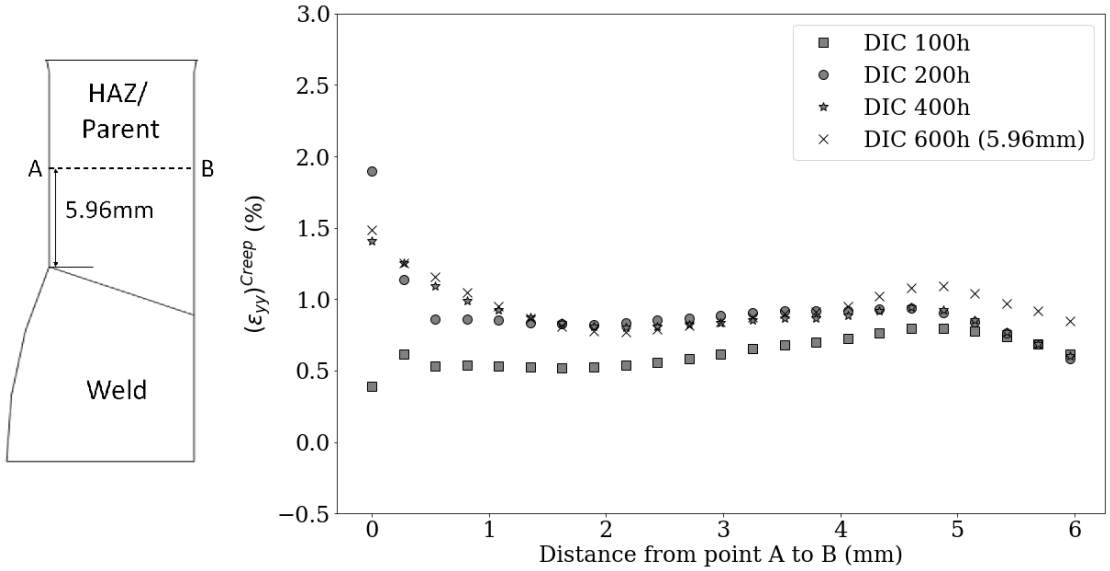

Figure 6.8: Plot of creep strains versus distance for a horizontal line in the specimen for x_w = 5.96mm for different creep times

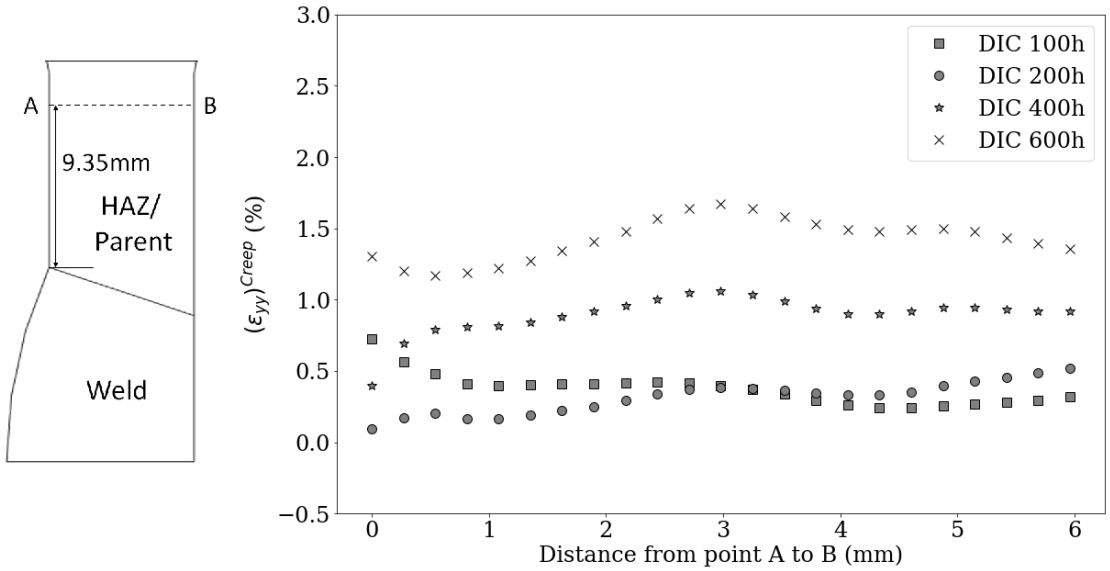

Figure 6.9: Plot of creep strains versus distance for a horizontal line in the specimen for x_w = 9.35mm for different creep times

6.3 FE Modelling

In order to estimate the augmented effect of creep mismatch in the presence of a geometrical notch such as a simulated weld cap as used in the DIC creep test, a finite element model was developed to match the logarithmic strain distributions obtained from the DIC creep test. The FE model was then used to investigate the difference in the effect of weld cap between a homogeneous material and a bi-material weld interface.

As the specimen was adequately thin (2mm), a 2D plane stress formulation was used. Only half of the test specimen had to be modelled taking advantage of the symmetry as the weld was located at the centre of the gauge section. Figure 6.10 shows a schematic of the specimen geometry along with the loading and applied boundary conditions. The specimen was hinged at the top end and a vertical symmetry condition applied at the bottom face which closely simulated the actual test boundary conditions. A control point was defined each at the specimen hole and connected to the periphery of the hole using a kinematic coupling. The rotation degree of freedom was not coupled. A concentrated load was applied to the control point at the top equivalent to the DIC creep test load.

Full integration plane stress quadratic elements (CPS8) were used for all the FE models. The reason for using full integration quadratic elements was to enable the use of singular quarter node elements at the free edges of the weld interface in the models. Mesh sensitivity analyses were performed using simple and single material elastic-plastic properties and a sufficiently refined mesh was derived for the model. Figure 6.11 shows the FE mesh. Singularity elements were used near the edges of the weld interface as shown in the figure.

The elastic modulus and Poisson's ratio for all the material zones of the specimen in the FE model were taken from table 4.4 of chapter 4. As the length of the HAZ/parent region in the gauge section of this specimen was considerably smaller than 20mm, the extent of the creep strong region as observed in the DIC creep tests of chapter 5, only two material regions, weld and HAZ/parent, were modelled in this work. The plastic portion of the stress-strain curve for the weld region was taken from table 5.4 of chapter 5. The plastic hardening data for the HAZ/parent (or the SAZ) was taken from table 5.4 of section 5.3 of chapter 5. A length parameter (l_w) as defined in section 5.3 and plotted in figure 5.29 of chapter 5, was used to linearly vary the plasticity in the HAZ/parent. The yield stresses and the corresponding plastic strains in the HAZ/parent was that of the weld material at l_w = 0 and that of the parent material yield stresses and plastic strains

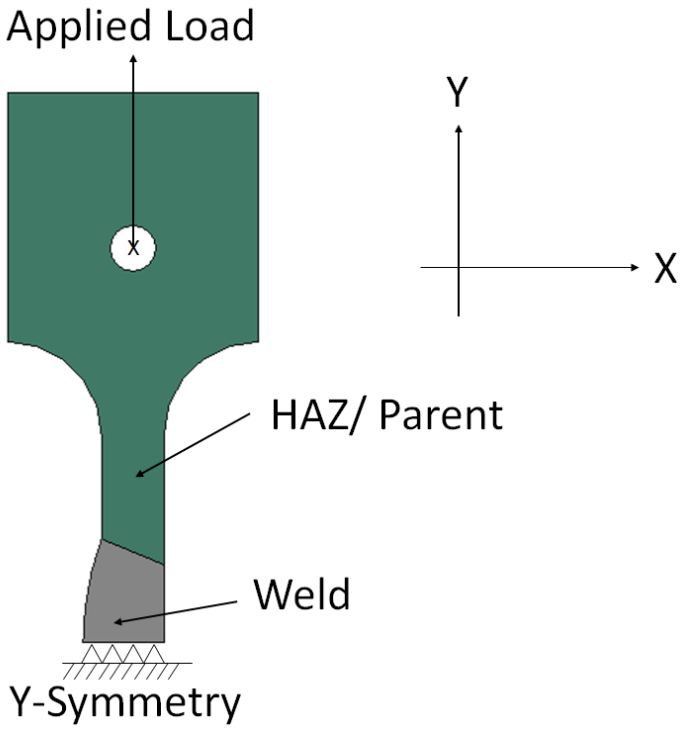

Figure 6.10: Schematic of the FE model showing the geometry and loading conditions

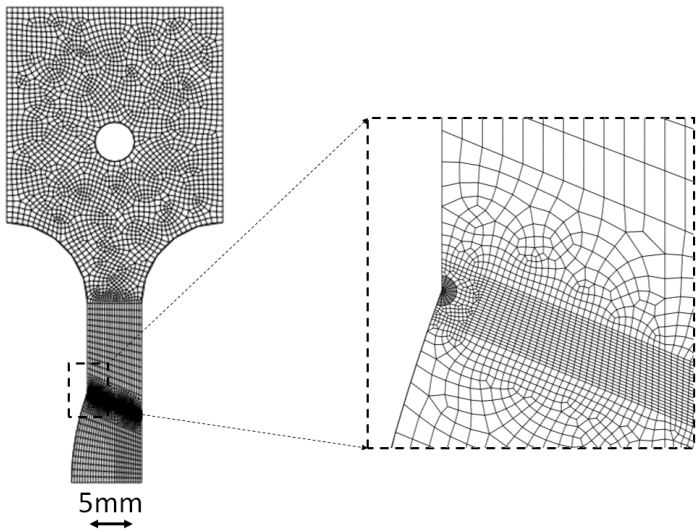

Figure 6.11: FE mesh of the DIC creep test specimen with a simulated weld cap

times 'l_w' at the end of the gauge section. The plastic properties were kept constant beyond the extent of the gauge section of the specimen as that was outside the focus of the analysis. An isotropic hardening was used in ABAQUS 6.14 (ABAQUS 6.14 documentation [132]) suite for the analysis.

As the length of the HAZ/parent section was significantly smaller than the test specimens used in chapter 5 and that the primary focus of the work was the region near the edge of the weld cap, constant creep constants were used in the HAZ/parent section, by fitting the creep models presented in section 2.2.4 (equations 2.6) to the creep response of three points in the HAZ/parent and lying on the specimen longitudinal centreline. The idea was to represent an average creep response for the HAZ/parent. Table 6.1 presents the creep constants used in the analysis.

Material	C1	C2	n1	C	n
Parent/ HAZ	2.9618D-12	0.42131	4.18	3.99025E-22	6.961
Weld	1.12131E-10	0.633182331	3.482723323	6.76083E-58	21.4

Table 6.1: Creep constants from data fits for the HAZ/parent and the weld

6.4 FE Model Results

Results obtained from the FE analysis of the capped weld specimen are discussed in this section. Variation of longitudinal creep strains across the width of the test specimen were compared for three different creep times: 100h, 200h and 400h. Figure 6.12 shows the comparison of longitudinal strains between FE model and DIC creep test. The section A-B was taken 0.5mm away from the edge of the cap as the DIC creep test results may be unreliable near the notch due to the presence of steep strain gradients and a relatively large subset size used for DIC data analysis. It can be seen from the figure that the FE results correspond well to the DIC test results except for near the edge of the weld cap where test data shows a sudden drop in the magnitude of strains while the FE results do not.

A sudden change in geometry such as the simulated weld cap in the test specimen results in a geometrical notch giving rise to stress concentration and strain localisation. This notch effect can be augmented when there is an abrupt material interface at the edge of the notch, like in the crossweld specimen tested. In order to investigate if an abrupt material interface at such a geometrical notch augments the stress concentration effects, it is important to compare crossweld creep test results to creep tests performed on homogeneous material specimens of the

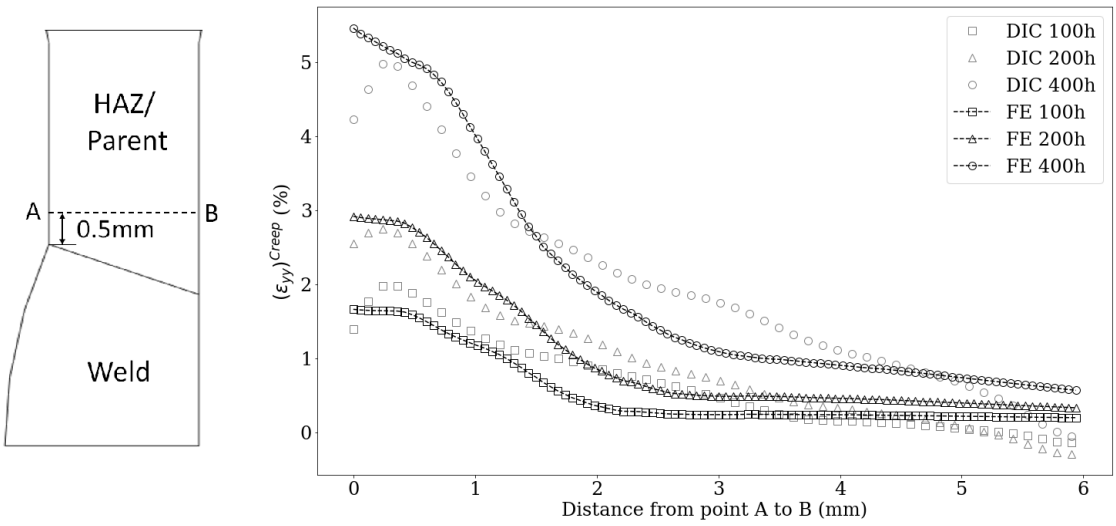

Figure 6.12: Capped crossweld specimen speckle pattern

same geometry. In this work, no creep test was performed in a homogeneous 316H specimen with a simulated weld cap. Hence, it was important to perform FE analysis on the same geometry as above but with homogeneous material properties across the specimen length. Therefore, FE analysis was performed on the same geometry but with 316H parent material properties. Figure 6.13 shows a comparison of longitudinal strain evolution across the width of the specimen between a one and a two material model. The section A-B was taken at the edge of the weld cap. It can be seen that for most of the specimen width, the magnitudes of strain obtained from the two material model remain lower than the one material model. However, at the edge of the weld cap, the strain values for the two parameter model suddenly shoot up. Also, it should be noted that the difference in the strain values between the two models is about 1%. Figure 6.14 shows a comparison of evolution of von Mises stress across the width of the specimen between a one and a two material model. There is no significant difference in von Mises stresses between the two models except that at 300h, some stress redistribution occurs for the two material model.

6.5 Conclusions

In this chapter, it was demonstrated that DIC creep tests can be used along with FE modelling to investigate the combined effects of geometry and material mismatch in a crossweld test specimen. Presence of a a weld cap can result in high peak strains at the edge of the weld cap, which is

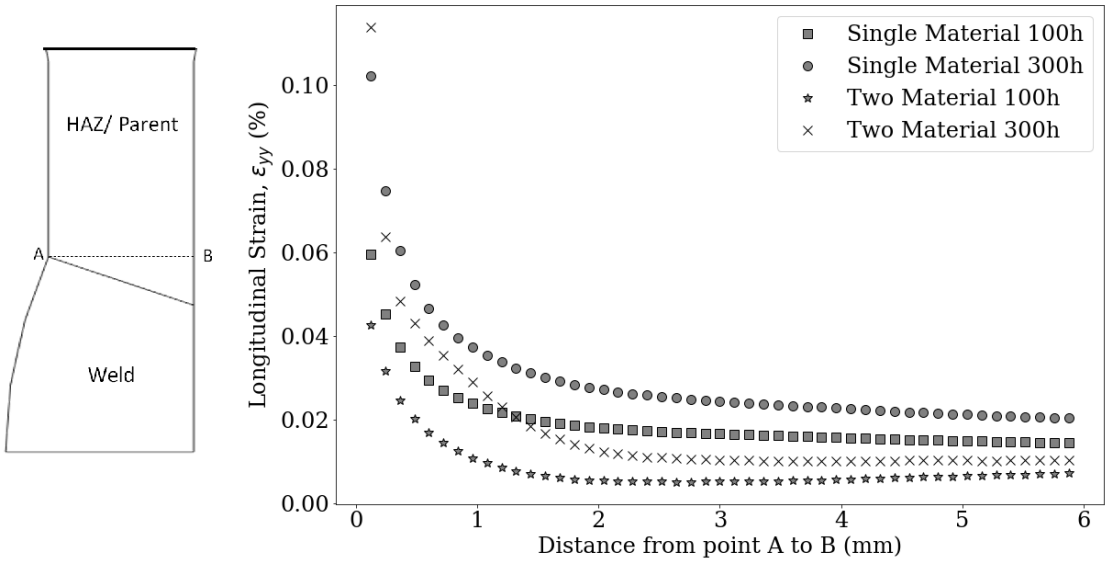

Figure 6.13: Capped crossweld specimen speckle pattern

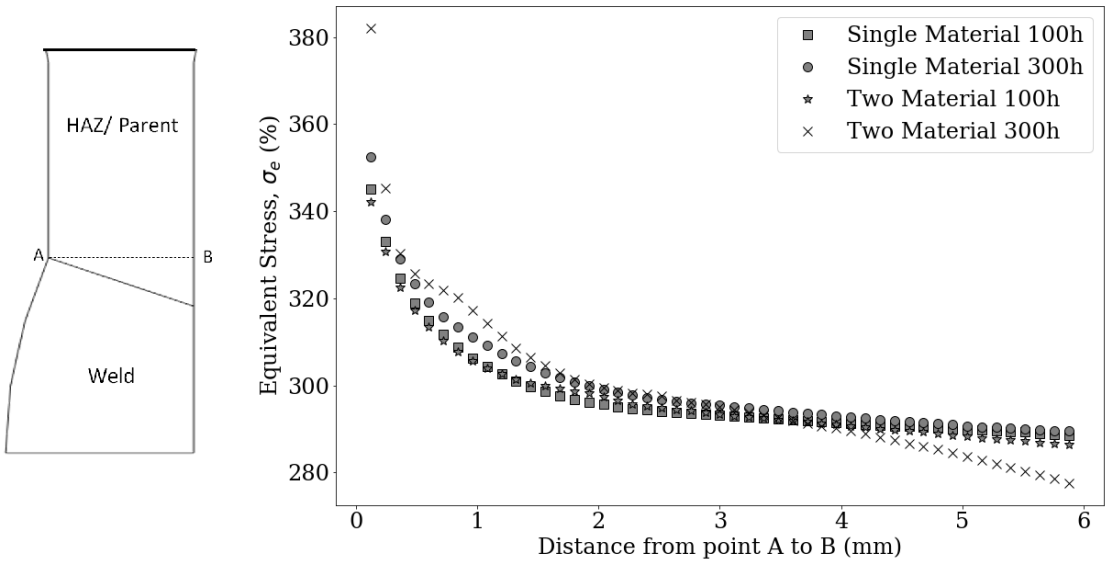

Figure 6.14: Capped crossweld specimen speckle pattern

also the weld interface. FE model results showed presence of singular variation of near the edge of the weld cap. Comparison of FE and DIC creep test results for a weld ligament 0.5mm away showed good agreement. Therefore, presence of a simulated weld cap led to strain localisation or stress concentration at the edge of the weld cap which was expected. However, further FE analysis comparison between a single homogeneous material and two material model revealed that the effect of geometry on creep is constant irrespective of the existence of any material mismatch. Therefore, it can be concluded that the effect of any material mismatch is insignificant as compared to the presence of a geometrical notch.

CHAPTER 7

CONCLUSIONS

"It does not matter how slowly you go as long as you do not stop."

Confucius

The important conclusions from the work are described in this chapter. The work investigated the existence and effects of possible creep variation in the strain hardened region of an ex-service multi-pass 316H weld.

At the outset, simple FE models were used to examine stress and strain concentration effects across a two material interface undergoing creep deformation. From an earlier work, it was known that for a numerical model, an abrupt change in creep properties across an interface gives rise to stress singularity at the free edge of the interface. Occurrence of stress singularity in a numerical model limits use of analytical modelling to investigate realistic stress and strain raising effects due to creep mismatch such as in a multi-pass weld. In this work, it was shown that by ignoring the peak stresses in a weld ligament along an interface, it was possible to observe the effects of creep mismatch on stress and strain distributions and measures of stress and strain raising effects were developed for various degrees of creep mismatch. Sensitivity of those factors to weld geometry and stress levels were also studied and an upper bound for those factors for a realistic level of creep mismatch for a 316H multi-pass weld was determined. Comparison of the upper bound stress concentration factor from this work with the documented one for dissimilar

metal welds between ferritic and austenitic steels showed that the documented SCF will be more conservative if applied to 316H multi-pass welds or other similar metal welds with a weak creep mismatch between the parent and the weld metal. Also, a new procedure for calculation of creep rupture lives for welds with a creep mismatch was proposed.

Although simplified FE modelling was used to derive useful stress and strain concentration factors for the most conservative case of an abrupt two material interface, in reality, the behaviour of a multi-pass weld is complicated by the existence of a strain hardened region across the weld interface. Earlier DIC based crossweld tests showed that the creep strains vary gradually along the the specimen axis from the weld fusion line into the parent material suggesting that there may be a gradual change in creep strength along the strain hardened region of multi-pass 316H welds. Impression creep tests on small specimens sliced from various locations in the strain hardened region of an ex-service multi-pass weld were used to build a profile of minimum creep strain rate versus distance from the weld fusion line. This work demonstrated that such impression creep tests can be successfully used to profile creep rates in a material with gradually varying creep behaviour. Results from the impression creep tests, however, showed that the maximum variation in minimum creep rates along the strain hardened region of the 316H weld was a factor of 2, much lesser than expected.

DIC creep tests performed on crossweld specimens of the same material revealed that although the creep rates do not vary much in the strain hardened region consistent with what was observed from the impression creep tests, a high level of initial plastic strains due to high test loads, together with a gradual variation of plastic hardening along the strain hardened region leads to a gradual variation of true stress in the strain hardened region. As creep of 316H has a high stress dependency (creep stress exponent > 5), a small variation in true stress value along the specimen has a pronounced effect on creep strains. However, no real strain localisation effect due to the weld interface could be observed from the tests. The tests give a good approximation for the effective length of the strain hardened region in the HAZ/parent where the creep rates vary. This is an extremely useful information for analytical modelling of multi-pass welds incorporating a strain hardened region. Finite element creep analysis results for the specimens showed good agreement with the tests. DIC creep tests give full field strain field whereas a benchmarked FE model reveals complete stress and strain field information. Therefore, DIC creep tests along with FE modelling can be an effective tool for detailed analysis of multi-pass weld behaviour.

DIC creep tests along with FE modelling were used to study the augmenting effect of weld geometry on strain localisation or stress concentration in a multi-pass weld. The DIC tests showed strain localisation near the edge of a simulated weld cap in a crossweld test specimen. FE results showed effects of stress singularity at the edge of the weld interface. However, comparison of DIC creep test and FE results for a weld ligament 0.5mm away from the material interface showed good agreement. Comparison of the FE results to one material model results showed that although the peak strains were high for the two material model with a weld cap, the magnitude of the strains fell sharply along the weld ligament compared to a single material model. The variation of stresses showed a very similar trend for both the two models.

It can be concluded that existence of a creep mismatch in an ex-service multi-pass 316H weld has insignificant effects on strain localisation or stress concentration. In a creep test, the observed variation in creep strains in a portion of the weld HAZ is more due to plastic hardening than due to an actual mismatch in creep behaviour. This is because of high levels of stresses used in creep testing. Impression creep test can be used to grade creep properties in the strain hardened region of a weld whereas DIC creep tests along with FE modelling can give a detailed picture of stress and strain variations in a crossweld specimen. The effect of weld geometry on creep is similar irrespective of a material mismatch.

This work has successfully measured the spatial distribution of creep rates in a crossweld test specimen and has showed that a combination of localised creep tests, DIC creep testing and FE modelling can be used to develop a more accurate understanding of creep behaviour of a weldment. In future, with some additional DIC creep tests, these FE models can be further refined to more accurately match the creep rate variation in the near fusion line HAZ/parent region of a 316H multi-pass weld which then can be used to develop accurate creep constitutive models for 316H weldments. This technique of combining DIC creep testing and FE modelling can be in general used to different types of similar and dissimilar metal welds to predict creep deformation. Accurate creep damage models can then be developed based on the creep constitutive equations for weldments.

BIBLIOGRAPHY

[1] UK ENERGY IN BRIEF.
Electricity generation and supply figures for scotland, wales, northern ireland and england, 2015 to 2018.
Energy & climate change, 1, 2019.

[2] EDF Energy (2009).
Assessment procedure for the high temperature response of structures.
EDF Energy, 5, 2009.

[3] Donald Peckner and Irving Melvin Bernstein.
Handbook of stainless steels.
McGraw-Hill Book Co., New York. 1977,(Chapters paged separately), 1977.

[4] Raymond Aurelius Higgins and Raymond Aurelius Higgins.
Engineering metallurgy: Applied physical metallurgy.
Edward Arnold, 1993.

[5] ASM Handbook Committee et al.
Properties and selection: Stainless steels, tool materials and special-purpose metals.
Metals Handbook Ninth Edition, 3, 1980.

[6] George E Totten.
Steel heat treatment: metallurgy and technologies.
crc Press, 2006.

[7] George Krauss.
Steels: processing, structure, and performance.
Asm International, 2015.

[8] P Marshall.
Austenitic stainless steels: microstructure and mechanical properties.
Springer Science & Business Media, 1984.

[9] JA Vaccari.
Standard wrought austenitic stainless-steels.
MATERIALS ENGINEERING, 80(7):63–71, 1974.

[10] Alenka Kosmač.
Stainless Steels: Tables of Fabrication Parameters: Welding Processes and Filler Materials-Heat Treatments-Typical End Uses.
Euro Inox, 2012.

[11] Yukio Takahashi, Takanori Nakazawa, et al.
Effect of grain size on high-temperature strength of fast reactor spec. sus316.
Zairyo, 46(11):1274–1279, 1997.

[12] John C Lippold and Damian J Kotecki.
Welding metallurgy and weldability of stainless steels.
2005.

[13] Peter Hedström.
Deformation induced martensitic transformation of metastable stainless steel AISI 301.
PhD thesis, Luleå tekniska universitet, 2005.

[14] RG Thomas.
" the effect of s-ferrite on the creep rupture properties of austenitic weld metals.
Welding journal, 57(3), 1978.

[15] Josip Brnic, Goran Turkalj, Marko Canadija, Domagoj Lanc, Sanjin Krscanski, Marino Brcic, Qiang Li, and Jitai Niu.
Mechanical properties, short time creep, and fatigue of an austenitic steel.
Materials, 9(4):298, 2016.

[16] Robert Hill.
Theory of mechanical properties of fibre-strengthened materialsóiii. self-consistent model.

Journal of the Mechanics and Physics of Solids, 13(4):189–198, 1965.

[17] RL Coble.
A model for boundary diffusion controlled creep in polycrystalline materials.
Journal of applied physics, 34(6):1679–1682, 1963.

[18] Rune Lagneborg.
Dislocation mechanisms in creep.
International Metallurgical Reviews, 17(1):130–146, 1972.

[19] KL Murty and I Charit.
Structural materials for gen-iv nuclear reactors: Challenges and opportunities.
Journal of Nuclear Materials, 383(1-2):189–195, 2008.

[20] WD Callister.
Material science and engineering: An introduction. vol. 6. 2000.

[21] F Garofalo.
Resistance to creep deformation and fracture in metals and alloys.
In *Properties of crystalline solids*. ASTM International, 1961.

[22] Forest C Monkman.
An empirical relationship between rupture life and minimum creep rate in creep rupture tests.
In *proc. ASTM*, volume 56, pages 91–103, 1956.

[23] G Sposito, C Ward, P Cawley, PB Nagy, and C Scruby.
A review of non-destructive techniques for the detection of creep damage in power plant steels.
Ndt & E International, 43(7):555–567, 2010.

[24] Harold J Frost and Michael F Ashby.
Deformation mechanism maps: the plasticity and creep of metals and ceramics.
Pergamon press, 1982.

[25] FR Nabarro and HL De Villiers.

The physics of creep: creep and creep-resistant alloy.
1995.

[26] RW Evans and B Wilshire.
Introduction to creep, 1993,(the institute of materials, london).
Google Scholar.

[27] Conyers Herring.
Diffusional viscosity of a polycrystalline solid.
Journal of applied physics, 21(5):437–445, 1950.

[28] Bijish Babu.
Physically based model for plasticity and creep of Ti-6Al-4V.
PhD thesis, Luleå tekniska universitet, 2008.

[29] Russell W Evans and Brian Wilshire.
Creep of metals and alloys.
1985.

[30] MF Ashby, C Gandhi, and DMR Taplin.
Fracture-mechanism maps and their construction for fcc metals and alloys.
In *Perspectives in Creep Fracture*, pages 1–31. Elsevier, 1983.

[31] Masaaki Tabuchi, Koichi Yagi, and Toshio Ohba.
Characterization of creep crack growth behaviour of 316 stainless steel in terms of microscopical fracture mechanism.
ISIJ International, 30(10):847–853, 1990.

[32] D McLean.
The physics of high temperature creep in metals.
Reports on Progress in Physics, 29(1):1, 1966.

[33] FK Odquist and GJ Hult.
Kriechfestigkeit metallischer werkstoffe–berlin, 1962.

[34] RCC-MR.

Appendix z, technical appendix a3.

RCC-MR, 1993.

[35] Bo Chen, David J Smith, Peter EJ Flewitt, and Michael W Spindler.

Constitutive equations that describe creep stress relaxation for 316h stainless steel at 550 c.

Materials at High Temperatures, 28(3):155–164, 2011.

[36] EDF Energy.

Agr materials data handbook r66 revision 9.

EDF Energy, Gloucester, UK, 2011.

[37] Vera Šijački Žeravčić, Gordana Bakic, Milos Djukic, and Biljana Andjelic.

Failures at elevated temperatures.

[38] MJ Manjoine.

Creep-rupture behavior of weldments.

WELDING J., 61(2):50, 1982.

[39] Jan Storesund and Shan Tung Tu.

Geometrical effect on creep in cross weld specimens.

International journal of pressure vessels and piping, 62(2):179–193, 1995.

[40] Gunther Eggeler, Ashok Ramteke, Mike Coleman, Brian Chew, Gerhard Peter, Andreas Burblies, John Hald, Clive Jefferey, Jahani Rantala, Ralf Mohrmann, et al.

Analysis of creep in a welded ëp91ípressure vessel.

International journal of pressure vessels and piping, 60(3):237–257, 1994.

[41] Shan-Tung Tu, Peter Segle, and Jian-Ming (1996) Gong.

Strength design and life assessment of welded structures subjected to high temperature creep.

International journal of pressure vessels and piping, 66(1-3):171–186, 1996.

[42] Shan-Tung Tu and Rolf Sandström.

The evaluation of weldment creep strength reduction factors by experimental and numerical simulations.

International journal of pressure vessels and piping, 57(3):335–344, 1994.

[43] RE Craine and MG Newman.
Modelling creep failure in welded plates under uniaxial loading.
The Journal of Strain Analysis for Engineering Design, 31(2):117–124, 1996.

[44] Pressure Vessel Code N47-29.
Code case n47-29.
ASME Class 1 Components in Elevated Temperature Service, 1992.

[45] Peter Mayr, Stefan Mitsche, Horst Cerjak, and Samuel M Allen.
The impact of weld metal creep strength on the overall creep strength of 9% cr steel weldments.
Journal of engineering materials and technology, 133(2):021011, 2011.

[46] Peter Segle.
Numerical simulation of weldment creep response.
PhD thesis, Materialvetenskap, 2002.

[47] Peter Segle, S-T Tu, J Storesund, and LÅ Samuelson.
Some issues in life assessment of longitudinal seam welds based on creep tests with cross-weld specimens.
International journal of pressure vessels and piping, 66(1-3):199–222, 1996.

[48] Lars A Samuelson, Peter Segle, and Peder Andersson.
Creep stress concentrations in mis-matched weldmentsóstarting points for early creep damage and creep cracking.
Materials at high temperatures, 15(3-4):415–420, 1998.

[49] FR Hall and DR Hayhurst.
Continuum damage mechanics modelling of high temperature deformation and failure in a pipe weldment.
Proceedings of the Royal Society of London. Series A: Mathematical and Physical Sciences, 433(1888):383–403, 1991.

[50] Shan-Tung Tu, Rui Wu, and Rolf Sandström.

Design against creep failure for weldments in 0· 5cr0· 5mo0· 25v pipe.
International journal of pressure vessels and piping, 58(3):345–354, 1994.

[51] MC Coleman, JD Parker, and DJ Walters.
The behaviour of ferritic weldments in thick section 12cr12mo14v pipe at elevated temperature.
International journal of pressure vessels and piping, 18(4):277–310, 1985.

[52] B Ivarsson and R Sandström.
Creep deformation and rupture of butt-welded tubes of cold-worked aisi 316 steel.
Metals Technology, 7(1):440–448, 1980.

[53] RJ Browne, BJ Cane, JD Parker, and DJ Walters.
Creep failure analysis of butt welded tubes.
In *Creep and fracture of engineering materials and structures*. 1981.

[54] TH Hyde and W (1997) Sun.
A method for estimating the stress distributions on the centre line of an axisymmetric, two-material, cross-weld, creep test specimen.
International journal of mechanical sciences, 39(8):885–898, 1997.

[55] LA Samuelson, P Segle, and ST Tu.
Design of weldments in structures subjected to creep.
In *Mechanical Effects of Welding*, pages 223–230. Springer, 1992.

[56] Y Wada, T Asayama, S Hasebe, and N Kasahara.
Creep-fatigue evaluation on butt welded joints of type 304 ss.
Technical report, 1997.

[57] P Chellapandi and SC Chetal.
Influence of mis-match of weld and base material creep properties on elevated temperature design of pressure vessels and piping.
Nuclear engineering and design, 195(2):189–196, 2000.

[58] Yongkui Li, Hiromichi Hongo, Masaaki Tabuchi, Yukio Takahashi, and Yoshio Monma.

Evaluation of creep damage in heat affected zone of thick welded joint for mod. 9cr–1mo steel.

International Journal of Pressure Vessels and Piping, 86(9):585–592, 2009.

[59] Peter Segle, Peder Andersson, and Lars Å Samuelson.

A parametric study of creep crack growth in heterogeneous ct specimens by use of finite element simulations.

Materials at High Temperatures, 15(2):63–68, 1998.

[60] Shan-Tung Tu, Peter Segle, and Jian-Ming (2004) Gong.

Creep damage and fracture of weldments at high temperature.

International journal of pressure vessels and piping, 81(2):199–209, 2004.

[61] VL Hein and F4 Erdogan.

Stress singularities in a two-material wedge.

International Journal of Fracture Mechanics, 7(3):317–330, 1971.

[62] ED Reedy Jr.

Intensity of the stress singularity at the interface corner between a bonded elastic and rigid layer.

Engineering Fracture Mechanics, 36(4):575–583, 1990.

[63] David B Bogy.

Edge-bonded dissimilar orthogonal elastic wedges under normal and shear loading.

Journal of Applied Mechanics, 35(3):460–466, 1968.

[64] DB Bogy and KC Wang.

Stress singularities at interface corners in bonded dissimilar isotropic elastic materials.

International Journal of Solids and Structures, 7(8):993–1005, 1971.

[65] J Dunders.

Edge-bonded dissimilar orthogonal elastic wedges under normal and shear loading.

Journal of Applied Mechanics, 36:650–652, 1969.

[66] M Fränkle, D Munz, and YY Yang.

Stress singularities in a bimaterial joint with inhomogeneous temperature distribution.

International journal of solids and structures, 33(14):2039–2054, 1996.

[67] Zhongrong Niu, Dali Ge, Changzheng Cheng, Jianqiao Ye, and Naman Recho.
Evaluation of the stress singularities of plane v-notches in bonded dissimilar materials.
Applied Mathematical Modelling, 33(3):1776–1792, 2009.

[68] ZQ Qian and AR Akisanya.
Wedge corner stress behaviour of bonded dissimilar materials.
Theoretical and applied fracture mechanics, 32(3):209–222, 1999.

[69] Andreas Ro, Anna-Margarete Sa, et al.
Stress singularities in bonded dissimilar materials under mechanical and thermal loading.
Computational materials science, 7(1-2):48–55, 1996.

[70] R Desmorat and FA Leckie.
Singularities in bi-materials: parametric study of an isotropic/anisotropic joint.
European Journal of Mechanics-A/Solids, 17(1):33–52, 1998.

[71] JP Dempsey and GB (1981) Sinclair.
On the singular behavior at the vertex of a bi-material wedge.
Journal of Elasticity, 11(3):317–327, 1981.

[72] JP Dempsey and GB (1979) Sinclair.
On the stress singularities in the plane elasticity of the composite wedge.
Journal of Elasticity, 9(4):373–391, 1979.

[73] Zhixue (2004) Wu.
Design free of stress singularities for bi-material components.
Composite Structures, 65(3-4):339–345, 2004.

[74] D Munz and YY Yang.
Stresses near the edge of bonded dissimilar materials described by two stress intensity factors.
International Journal of Fracture, 60(2):169–177, 1993.

[75] TC Wang.

Elastic-plastic asymptotic fields for cracks on bimaterial interfaces.
Engineering Fracture Mechanics, 37(3):527–538, 1990.

[76] Jin-Quan Xu, Lie-Dong Fu, and Yoshiharu Mutoh.
A method for determining elastic-plastic stress singularity at the interface edge of bonded power law hardening materials.
JSME International Journal Series A Solid Mechanics and Material Engineering, 45(2):177–183, 2002.

[77] Le Van Lich et al.
Plastic stress singularity near interface edge of elasto-plastic/elastic bi-material.
Computational Materials Science, 78:140–146, 2013.

[78] Anisur Rahman and ACW Lau.
Singular stress fields in interfacial notches of hybrid metal matrix composites.
Composites Part B: Engineering, 29(6):763–768, 1998.

[79] Takayuki Kitamura, Kittikorn Ngampungpis, and Hiroyuki Hirakata.
Stress field near interface edge of elastic-creep bi-material.
Engineering fracture mechanics, 74(10):1637–1648, 2007.

[80] Kittikorn Ngampungpis, Takayuki Kitamura, and Hiroyuki Hirakata.
Increase of stress intensity near interface edge of elastic-creep bi-material under a sustained load.
Engineering Fracture Mechanics, 75(6):1285–1293, 2008.

[81] Zhixue (2008) Wu.
Stress concentration analyses of bi-material bonded joints without in-plane stress singularities.
International Journal of Mechanical Sciences, 50(4):641–648, 2008.

[82] TH Hyde and W Sun.
Stress singularities at the free surface of an axisymmetric two-material creep test specimen.
The Journal of Strain Analysis for Engineering Design, 32(2):107–117, 1997.

[83] SNG Chu and JCM Li.

Impression creep; a new creep test.
Journal of Materials Science, 12(11):2200–2208, 1977.

[84] Hsiang-Yung Yu and JCM Li.
Computer simulation of impression creep by the finite element method.
Journal of Materials Science, 12(11):2214–2222, 1977.

[85] Edward C Yu and JCM Li.
Impression creep of lif single crystals.
Philosophical Magazine, 36(4):811–825, 1977.

[86] S N G Chu and J C M Li.
Localized stress relaxation by impression testing.
Materials Science and Engineering, 45(2):167–171, 1980.

[87] WS Gibbs, DK Matlock, DL Olson, and SH Wang.
High temperature impression creep testing of weldments.
Weld. J.(Miami);(United States), 64(6), 1985.

[88] Fuqian Yang, JCM Li, and CW Shih.
Computer simulation of impression creep using the hyperbolic sine stress law.
Materials Science and Engineering: A, 201(1-2):50–57, 1995.

[89] S N G Chu and J C M Li.
Impression creep of β-tin single crystals.
Materials Science and Engineering, 39(1):1–10, 1979.

[90] HY Yu, MA Imam, and BB Rath.
Study of the deformation behaviour of homogeneous materials by impression tests.
Journal of materials science, 20(2):636–642, 1985.

[91] P Tasnadi, A Juhasz, NQ Chinh, and I Kovacs.
Theoretical description of the deformation taking place in an impression test.
Res mechanica, 24(4):335–347, 1988.

[92] TH Hyde, KA Yehia, and AA Becker.

Interpretation of impression creep data using a reference stress approach.
International journal of mechanical sciences, 35(6):451–462, 1993.

[93] WS Gibbs, RM Aikin Sr, PL Martin, and RA Patterson.
Impression creep characterization of tial weldments.
Technical report, Los Alamos National Lab., NM (USA), 1990.

[94] TH Hyde, W Sun, and AA Becker.
Analysis of the impression creep test method using a rectangular indenter for determining the creep properties in welds.
International journal of mechanical sciences, 38(10):1089–1102, 1996.

[95] HY Yu, MA Imam, and BB (1985) Rath.
Study of mechanical properties of weldments by impression tests.
Welding Research Supplement, 2:55–58, 1985.

[96] MA Imam, RVV JUDY JR, and BB Rath.
Evaluation of tensile flow properties of weldments in titanium alloys.
E-Ti, 6:2V–6Zr, 1987.

[97] MA Lisin, ID Choi, DK Matlock, and DL Olson.
A composite modeling analysis of impression creep testing on heterogeneous materials.
International Welding Journal, 69:159s–165s, 1990.

[98] DH Sastry.
Impression creep techniqueóan overview.
Materials Science and Engineering: A, 409(1-2):67–75, 2005.

[99] TH Hyde, W Sun, and JA Williams.
Creep behaviour of parent, weld and haz materials of new, service-aged and repaired 1/2cr1/2mo1/4v: 2 1/4cr1mo pipe welds at 640 c.
Materials at High Temperatures, 16(3):117–129, 1999.

[100] BL Boyce, PL Reu, and CV Robino.
The constitutive behavior of laser welds in 304l stainless steel determined by digital image correlation.

Metallurgical and Materials Transactions A, 37(8):2481–2492, 2006.

[101] Murat Acar, Salih Gungor, Supriyo Ganguly, Peter Bouchard, and ME Fitzpatrick.
Variation of mechanical properties in a multi-pass weld measured using digital image correlation.
2009.

[102] AP Reynolds and F Duvall.
Digital image correlation for determination of weld and base metal constitutive behavior.
WELDING JOURNAL-NEW YORK-, 78:355–s, 1999.

[103] MO Acar, S Gungor, ME Fitzpatrick, and PJ Bouchard.
Numerical study of strength mismatch in cross-weld tensile testing.
2011.

[104] Murat O®zgu®n Acar.
Effects of plastic strain history on the properties of stainless steel boiler tube welds.
PhD thesis, The Open University, 2011.

[105] JS Lyons, J Liu, and MA Sutton.
High-temperature deformation measurements using digital-image correlation.
Experimental mechanics, 36(1):64–70, 1996.

[106] Jin Liu, Jed Lyons, Michael Sutton, and Anthony Reynolds.
Experimental characterization of crack tip deformation fields in alloy 718 at high temperatures.
Journal of engineering materials and technology, 120(1):71–78, 1998.

[107] C Maharaj, JP Dear, and A Morris.
A review of methods to estimate creep damage in low-alloy steel power station steam pipes.
Strain, 45(4):316–331, 2009.

[108] Andy Morris, Chris Maharaj, Amit Puri, Miltiadis Kourmpetis, and John Dear.
Recent developments in methods to study creep strain variations in power station steam plant.

In *ASME 2008 Pressure Vessels and Piping Conference*, pages 529–535. American Society of Mechanical Engineers Digital Collection, 2009.

[109] Andy Morris, Chris Maharaj, Iain Palmer, Amit Puri, and John Dear.
Developments in combined arcmac and strain mapping systems for creep measurement.
In *ASME 2008 Pressure Vessels and Piping Conference*, pages 521–528. American Society of Mechanical Engineers Digital Collection, 2009.

[110] LaVision GmbH.
Digital image correlation systems for full field shape, displacement and strain.

[111] DANTEC DYNAMICS A/S, Tonsbakken 16-18 Skovlunde, Denmark.
Laser Optical Measurement System and Sensors.

[112] Rui Zhang and Lingfeng He.
Measurement of mixed-mode stress intensity factors using digital image correlation method.
Optics and Lasers in Engineering, 50(7):1001–1007, 2012.

[113] Pan Bing, Xie Hui-Min, Xu Bo-Qin, and Dai Fu-Long.
Performance of sub-pixel registration algorithms in digital image correlation.
Measurement Science and Technology, 17(6):1615, 2006.

[114] Matheus Grasselli and Dmitry Pelinovsky.
Numerical mathematics.
Jones & Bartlett Learning, 2008.

[115] Tom Lyche and Knut Morken.
Spline methods.
Department of Informatics, Centre of Mathematics for Applications, University of Oslo, 2008.

[116] David Gibb, GA Carse, and G Shearer.
A course in interpolation and numerical integration for the mathematical laboratory.
1915.

[117] HA Bruck, SR McNeill, M Ae Sutton, and WH Peters.
Digital image correlation using newton-raphson method of partial differential correction.
Experimental mechanics, 29(3):261–267, 1989.

[118] Hubert W Schreier, Joachim R Braasch, and Michael A Sutton.
Systematic errors in digital image correlation caused by intensity interpolation.
Optical engineering, 39, 2000.

[119] Robert J Schalkoff.
Digital image processing and computer vision, volume 286.
Wiley New York, 1989.

[120] Robert J Marks II.
Handbook of Fourier analysis & its applications.
Oxford University Press, 2009.

[121] John N Rayner.
An introduction to spectral analysis, volume 174.
Pion London, 1971.

[122] Robin Wilson.
Euler's Pioneering Equation: The most beautiful theorem in mathematics.
Oxford University Press, 2018.

[123] YQ Wang, MA Sutton, PL Reu, and TJ Miller.
Image matching error assessment in digital image correlation.
In *Proceedings of the SEM Annual Conference*, 2009.

[124] Edmund Taylor Whittaker.
Xviii.óon the functions which are represented by the expansions of the interpolation-theory.
Proceedings of the Royal Society of Edinburgh, 35:181–194, 1915.

[125] William Thielicke and Eize Stamhuis.
Pivlab–towards user-friendly, affordable and accurate digital particle image velocimetry in matlab.
Journal of Open Research Software, 2(1), 2014.

[126] Hubert W Schreier and Michael A Sutton.
Systematic errors in digital image correlation due to undermatched subset shape functions.
Experimental Mechanics, 42(3):303–310, 2002.

[127] Peng Zhou and Kenneth E Goodson.
Subpixel displacement and deformation gradient measurement using digital image/speckle correlation.
Optical Engineering, 40(8):1613–1621, 2001.

[128] M. Ueda.
Study on accuracy evaluation of deformation and strain distribution measurement using digital image correlation.
The Japan Society of Mechanical Engineering, 76:119, 2009.

[129] D Lecompte, ASHJD Smits, Sven Bossuyt, Hugo Sol, J Vantomme, D Van Hemelrijck, and AM Habraken.
Quality assessment of speckle patterns for digital image correlation.
Optics and lasers in Engineering, 44(11):1132–1145, 2006.

[130] Sun Yaofeng and John HL Pang.
Study of optimal subset size in digital image correlation of speckle pattern images.
Optics and lasers in engineering, 45(9):967–974, 2007.

[131] Bing Pan, Huimin Xie, Zhaoyang Wang, Kemao Qian, and Zhiyong Wang.
Study on subset size selection in digital image correlation for speckle patterns.
Optics express, 16(10):7037–7048, 2008.

[132] Dassault Systèmes.
Abaqus 6.14 documentation.
Providence, RI: Dassault Systèmes, 2014.

[133] Yung-Li Lee and Mark E Barkey.
Fundamentals of cyclic plasticity theories.
Metal Fatigue Analysis Handbook: Practical Problem-solving Techniques for Computer-aided Engineering, page 253, 2011.

[134] Ali S Argon.

Constitutive equations in plasticity.

MIT press Cambridge, Massachussetts, 1975.

[135] HD Hibbitt.

Abaqus/epgenóa general purpose finite element code with emphasis on nonlinear applications.

Nuclear Engineering and Design, 77(3):271–297, 1984.

[136] James T Boyle and John Spence.

Stress analysis for creep.

Elsevier, 2013.

[137] Sunil Goyal, K Laha, CR Das, S Panneer Selvi, and MD Mathew.

Finite element analysis of uniaxial and multiaxial state of stress on creep rupture behaviour of 2.25 cr–1mo steel.

Materials Science and Engineering: A, 563:68–77, 2013.

[138] Yun-Jae Kim.

Contour integral calculations for generalised creep laws within abaqus.

International journal of pressure vessels and piping, 78(10):661–666, 2001.

[139] DP Bray, RJ Dennis, and RAW Bradford.

Modelling the complex manufacturing history of a pipework joint and assessment of its through life creep-fatigue damage using finite element based methods.

In *ASME 2010 Pressure Vessels and Piping Division/K-PVP Conference*, pages 401–419. American Society of Mechanical Engineers Digital Collection, 2010.

[140] YP Jiang, WL Guo, ZF Yue, and J Wang.

On the study of the effects of notch shape on creep damage development under constant loading.

Materials Science and Engineering: A, 437(2):340–347, 2006.

[141] Pressure Vessel Code.

Rules for constructions of nuclear facility components.

BPVC Section III, Division 1-Subsection NH-Class 1 Components in Elevated Temperature Service, 2015.

[142] Stefan Holmström, Rami Pohja, Asta Nurmela, Pekka Moilanen, and Pertti Auerkari.
Creep and creep-fatigue behaviour of 316 stainless steel.
Procedia Engineering, 55:160–164, 2013.

[143] MW Spindler, R Hales, and RP Skelton.
The multiaxial creep ductility of an ex-service type 316h stainless steel.
BOOK-INSTITUTE OF MATERIALS, 769:679–690, 2001.

[144] B Chassignole, D Villard, M Dubuget, JC Baboux, and R El Guerjouma.
Characterization of austenitic stainless steel welds for ultrasonic ndt.
In *AIP Conference Proceedings*, volume 509, pages 1325–1332. AIP, 2000.

[145] RP Skelton, IW Goodall, GA Webster, and MW Spindler.
Factors affecting reheat cracking in the haz of austenitic steel weldments.
International journal of pressure vessels and piping, 80(7-8):441–451, 2003.

[146] PJ Bouchard, PJ Withers, SA McDonald, and RK Heenan.
Quantification of creep cavitation damage around a crack in a stainless steel pressure vessel.
Acta Materialia, 52(1):23–34, 2004.

[147] EDF Energy (2017).
Cast 69431 new weld details.
Private communication.
Internal Correspondence; accessed July 2017.

[148] H Udaya Prasanna and K Rajendra Udupa.
Indentation creep studies to evaluate the mechanical properties of stainless steel welds.
Australian Journal of Mechanical Engineering, 14(1):39–43, 2016.

[149] Naveena VD Vijayanand, V Ganesan, K Laha, and MD Mathew.
Evaluation of creep deformation behaviour of different microstuctural zones of 316ln ss weld joint using impression creep testing technique.

Materials Science and Technology, 30(10):1223–1228, 2014.

[150] Edward Hares, Mahmoud Mostafavi, Richard Bradford, and Chris Truman.
The influence of creep strain rate on creep damage formation in austenitic stainless steel.
In *ASME 2018 Pressure Vessels and Piping Conference*. American Society of Mechanical Engineers Digital Collection, 2018.

[151] Chang-Sik Oh, Nak-Hyun Kim, Yun-Jae Kim, Catrin Davies, Kamran Nikbin, and David Dean.
Creep failure simulations of 316h at 550 c: Part i–a method and validation.
Engineering Fracture Mechanics, 78(17):2966–2977, 2011.

[152] EDF Energy.
Tensile data 316 cast 69431 header 2c2/3.
Private communication.
Internal Correspondence; accessed March 2018.

[153] EDF Energy (2018).
Tensile data 316 cast 69431 haz header 2c2/3.
Private communication.
Internal Correspondence; accessed September 2018.

[154] TH Hyde and Sun, W.
Evaluation of conversion relationships for impression creep test at elevated temperatures.
International Journal of Pressure Vessels and Piping, 86(11):757–763, 2009.

[155] WH Peters and WF Ranson.
Digital imaging techniques in experimental stress analysis.
Optical engineering, 21(3):213427, 1982.

[156] SR McNeill, WH Peters, WF Ranson, and MA Sutton.
A study of fracture parameters by digital image processing.
Developments in mechanics., 12:267–271, 1983.

[157] MA Sutton, WJ Wolters, WH Peters, WF Ranson, and SR McNeill.
Determination of displacements using an improved digital correlation method.

Image and vision computing, 1(3):133–139, 1983.

[158] TC Chu, WF Ranson, and Mr A Sutton.
Applications of digital-image-correlation techniques to experimental mechanics.
Experimental mechanics, 25(3):232–244, 1985.

[159] Po-Chih Hung and AS Voloshin.
In-plane strain measurement by digital image correlation.
Journal of the Brazilian Society of Mechanical Sciences and Engineering, 25(3):215–221, 2003.

[160] Y Sakanashi, S Gungor, and PJ (2011) Bouchard.
Measurement of creep deformation in stainless steel welded joints.
In *Optical Measurements, Modeling, and Metrology, Volume 5*, pages 371–378. Springer, 2011.

[161] Y Sakanashi, S Gungor, and PJ (2012) Bouchard.
Creep deformation measurement of 316h stainless steel multi-pass welded joints using digital image correlation.
2012.

[162] A Narayanan, K Dubey, CM Davies, and JP Dear.
The creep of alloy 617 at 700°c: Material properties, measurement of strain and comparison between finite element analysis and digital image correlation.
International Journal of Solids and Structures, 129:195–203, 2017.

[163] Steven Cooreman, D Lecompte, H Sol, Johnny Vantomme, and Dimitri Debruyne.
Identification of mechanical material behavior through inverse modeling and dic.
Experimental Mechanics, 48(4):421–433, 2008.

[164] Kevin M Moerman, Cathy A Holt, Sam L Evans, and Ciaran K Simms.
Digital image correlation and finite element modelling as a method to determine mechanical properties of human soft tissue in vivo.
Journal of biomechanics, 42(8):1150–1153, 2009.

[165] Daniel Gerbig, Allan Bower, Vesna Savic, and Louis G Hector Jr.

Coupling digital image correlation and finite element analysis to determine constitutive parameters in necking tensile specimens.
International Journal of Solids and Structures, 97:496–509, 2016.

[166] E8-99 ASTM et al.
Standard test methods for tension testing of metallic materials.
Annual book of ASTM standards. ASTM, 2001.

[167] American Society for Testing and Materials. Committee E-28 on Mechanical Testing.
Standard Test Methods for Conducting Creep, Creep-rupture, and Stress-rupture Tests of Metallic Materials.
ASTM International, 2006.

[168] G Crammond, SW Boyd, and JM Dulieu-Barton.
Speckle pattern quality assessment for digital image correlation.
Optics and Lasers in Engineering, 51(12):1368–1378, 2013.

[169] Takashi Matsutani.
Color interpolation method in bayer array, March 3 2009.
US Patent 7,499,089.

[170] Alexander Forsey.
Using colour cameras for digital image correlation: how bad are they?

[171] Rastislav Lukac, Karl Martin, and Konstantinos N Plataniotis.
Demosaicked image postprocessing using local color ratios.
IEEE Transactions on Circuits and Systems for Video Technology, 14(6):914–920, 2004.

[172] A Forsey and S Gungor.
Demosaicing images from colour cameras for digital image correlation.
Optics and lasers in engineering, 86:20–28, 2016.

[173] Guy Pluvinage.
Fracture and fatigue emanating from stress concentrators.
Springer Science & Business Media, 2007.

[174] Zoran D Perovic.

The weld profile effect on stress concentration factors in weldments, 15 th international research.

In *Expert Conference (Trends in The Development of Machinery and Associated Technology) Czech Republic*, 2011.

[175] LW Zachary and CP Burger.

Stress concentrations in double welded partial joint penetration butt welds.

Welding Journal, 55(3):77, 1976.

[176] Inge (2008) Lotsberg.

Stress concentration factors at welds in pipelines and tanks subjected to internal pressure and axial force.

Marine Structures, 21(2-3):138–159, 2008.

[177] P Smedley, P Fisher, et al.

Stress concentration factors for simple tubular joints.

In *The First International Offshore and Polar Engineering Conference*. International Society of Offshore and Polar Engineers, 1991.

[178] GR Stevick and I Finnie.

Stress concentrations resulting from longitudinal butt-welds in piping at elevated temperatures.

In *Creep in Structures*, pages 629–636. Springer, 1991.